Tubulin-Binding 3,5-Bis(styryl)pyrazoles as Lead Compounds for the Treatment of Castration-Resistant Prostate Cancer [S]

Vivian W.Y. Liao,[3] Anuradha Kumari,[3] ®Rajeshwar Narlawar, Soma Vignarajan,
®David E. Hibbs, Dulal Panda, and ®Paul W. Groundwater

Sydney Pharmacy School, Faculty of Medicine and Health (V.W.Y.L., R.N., D.E.H., P.W.G.) and Charles Perkins Centre (S.V.), The University of Sydney, Sydney, New South Wales, Australia; and Department of Biosciences and Bioengineering, Indian Institute of Technology Bombay, Mumbai, India (A.K., D.P.)

Received October 17, 2019; accepted March 24, 2020

ABSTRACT

The microtubule-binding taxanes, docetaxel and cabazitaxel, are administered intravenously for the treatment of castration-resistant prostate cancer (CRPC) as the oral administration of these drugs is largely hampered by their low and highly variable bioavailabilities. Using a simple, rapid, and environmentally friendly microwave-assisted protocol, we have synthesized a number of 3,5-bis(styryl)pyrazoles **2a-l**, thus allowing for their screening for antiproliferative activity in the androgen-independent PC3 prostate cancer cell line. Surprisingly, two of these structurally simple 3,5-bis(styryl)pyrazoles (**2a** and **2l**) had concentrations which gave 50% of the maximal inhibition of cell proliferation (GI_{50}) in the low micromolar range in the PC3 cell line and were thus selected for extensive further biologic evaluation (apoptosis and cell cycle analysis, and effects on tubulin and microtubules). Our findings from these studies show that 3,5-bis[(1E)-2(2,6-dichlorophenyl)ethenyl]-1H-pyrazole **2l** 1) caused significant effects on the cell cycle in PC3 cells, with the vast majority of treated cells in the G_2/M phase (89%); 2) induces cell death in PC3 cells even after the removal of the compound; 3) binds to tubulin [dissociation constant (K_d) 0.4 ± 0.1 μM] and inhibits tubulin polymerization in vitro; 4) had no effect upon the polymerization of the bacterial cell division protein FtsZ (a homolog of tubulin); 5) is competitive with paclitaxel for binding to tubulin but not with vinblastine, crocin, or colchicine; and 6) leads to microtubule depolymerization in PC3 cells. Taken together, these results suggest that 3,5-bis(styryl)pyrazoles warrant further investigation as lead compounds for the treatment of CRPC.

SIGNIFICANCE STATEMENT

The taxanes are important components of prostate cancer chemotherapy regimens, but their oral administration is hampered by very low and highly variable oral bioavailabilities resulting from their poor absorption, poor solubility, high first-pass metabolism, and efficient efflux by P-glycoprotein. New chemical entities for the treatment of prostate cancer are thus required, and we report here the synthesis and investigation of the mechanism of action of some bis(styryl)pyrazoles, demonstrating their potential as lead compounds for the treatment of prostate cancer.

Introduction

Globally, prostate cancer is the second most common male cancer in terms of incidence and fifth in terms of mortality, with over 300,000 men dying from the disease every year (Todd et al., 2018). Tumor growth in the early stages of prostate cancer is androgen-dependent, so the typical treatment of early metastatic prostate cancer is androgen deprivation therapy with a gonadotropin-releasing hormone analog such as leuprolide, often in combination with an antiandrogen such as flutamide (Crawford et al., 1989; Garnick, 1997; Taplin and Balk, 2004).

As the disease progresses, however, molecular and cellular changes occur so that cancer becomes androgen-independent/hormone refractory (termed castration-resistant prostate cancer [CRPC]) and unresponsive to current hormone therapy (Feldman and Feldman, 2001; Todd et al., 2018). This form of prostate cancer is aggressive, highly metastatic, and associated with poor prognosis (mean survival time of 18–24 months) (Abouelfadel and Crawford, 2008), and there is no effective treatment (Karantanos et al., 2013).

Paclitaxel has been used in the treatment of prostate cancer, and the semisynthetic taxanes, docetaxel and cabazitaxel, are administered intravenously for the treatment of CRPC. The oral administration of these drugs is hampered by their low and highly variable bioavailabilities (Torne et al., 2010), which are due to their poor absorption (a result of their poor solubilities); efficient efflux by P-glycoprotein, which is abundant in the gastrointestinal tract; and high first-pass metabolism by CYP450s, CYP2C8 and 3A4.

ABBREVIATIONS: AUC, area under the curve; CRPC, castration-resistant prostate cancer; GI_{50}, concentrations which gave 50% of the maximal inhibition of cell proliferation; HPLC, high-pressure liquid chromatography; K_d, dissociation constant; MTT, 3-(4,5-dimethyl-2-thiazolyl)-2,5-diphenyl-2H-tetrazolium bromide; OD, optical density; PDB, Protein Data Bank; PI, propidium iodide; PIPES, 1,4-piperazinediethanesulfonic acid.

We report here the discovery of a 3,5-bis(styryl)pyrazole analog **2l** that induces cell death in PC3 cells (Pulukuri et al., 2005; Schmitt et al., 2014) even after the removal of the compound. The compound binds to tubulin (K_d 0.4 ± 0.1 μM) and inhibits tubulin polymerization in vitro (with no effect upon the polymerization of the bacterial homolog *Streptococcus pneumoniae* FtsZ (*spn* FtsZ) or on the activity of alkaline phosphatase). Pyrazole **2l** is competitive with paclitaxel for binding to tubulin (but not with vinblastine, crocin, or colchicine), and treatment with pyrazole **2l** results in microtubule depolymerization in PC3 cells, suggesting the further investigation of these 3,5-bis(styryl)pyrazoles as lead compounds for the treatment of CRPC.

Materials and Methods

General Synthetic Chemistry Procedures. The 3,5-bis(styryl) pyrazoles **2a-l** were synthesized from the curcuminoids **1** (Supplemental Methods) using a CEM Discover SP microwave synthesis system. The spectroscopic and analytical data for pyrazoles **2a** (Amolins et al., 2009; Mayadevi et al., 2012), **2b** (Amolins et al., 2009), and **2k** (Luo et al., 2013) were identical to that reported previously. Melting points were determined on a Stuart Scientific SMP10 apparatus. Infrared spectra were obtained on a FTIR-8400S Shimadzu system using NaCl plates, and values are recorded as wave numbers (cm^{-1}). ^1H and ^{13}C NMR spectra were recorded at 400 and 100 MHz, respectively, on a Varian 400-MR magnetic resonance spectrometer, with chemical shifts (δ) reported in parts per million (ppm). Spectra were acquired in solutions of deuterated solvents, and the residual solvent peaks were used as internal references: 7.24 ppm (deuterochloroform, CDCl$_3$), 2.50 ppm (DMSO-d_6), 2.05 ppm (acetone-d_6), and 3.31 ppm (methanol-d_4). Low-resolution electrospray ionization mass spectrometry was performed on a TSQ Quantum Access Max LCMS/MS (Thomas R Watson Mass Spectrometry Laboratory, Sydney Pharmacy School, The University of Sydney), and high-resolution mass spectroscopy was performed on a Bruker 7T Fourier transform ion cyclotron resonance mass spectrometer (Mass Spectrometry Unit, School of Chemistry, The University of Sydney). Elemental analysis was performed on a Thermo Flash 2000 Elemental Analyzer (Campbell Microanalytical Laboratory, University of Otago, New Zealand). All reagents were commercially available and purchased from Sigma Aldrich (Castle Hill, Sydney, Australia) and Alfa Aesar (VWR, Australia). Solvents were purchased from Chem-Supply (Australia) and were used as received. Flash column chromatography was performed using Grace Davison (LC604 40–63 μm) Davisil chromatographic silica media. Thin-layer chromatography was performed using Grace Davidson Reveleris, aluminum-backed thin-layer chromatography plates (UV254).

General Experimental Procedure for the Synthesis of Pyrazoles 2a-l. Pyrazole derivatives **2a-l** were synthesized using a modification of the method of Mayadevi et al. (2012). Curcuminoids **1** (1.0 mmol) were dissolved in *N,N*-dimethylformamide (DMF) (1 ml). Acetic acid (1 ml) and hydrazine monohydrate (0.2 ml) were added to the solution in a microwave synthesizer tube. The mixture was placed in the microwave reactor and heated at 80°C for 5 minutes with rapid stirring. The reaction was cooled then added dropwise to stirred water (100 ml). The solid was collected by filtration, purified by flash chromatography using a gradient mobile phase of ethyl acetate and hexane (1:4 to 1:1), and then recrystallized from ethanol. Spectroscopic and analytical data for the pyrazoles are provided in the Supplemental Methods.

General Experimental Procedure for the Degradation Studies. HiPerSolv CHROMANORM liquid chromatography–mass spectrometry grade acetonitrile and methanol were purchased from VWR International. High-performance liquid chromatography (HPLC) grade glacial acetic acid was purchased from Fisher Scientific, UK. Ultrapure water was obtained with an SG Ultra Clear water

system. The chromatographic separation was performed on an Aquacil C_{18} column (2.1 × 100 mm, 5 μm particle size; Thermo Scientific).

An orbital mixter incubator (Ratek Instruments, Australia) was used for the degradation study at 37°C and 200 rpm. The HPLC analysis was carried out on a Shimadzu ultrafast liquid chromatography prominence system, consisting of a DGU-20A5R degassing unit, an LC-20AD pump, a SIL-20AHT autosampler, a SPD-M20A photo-diode array detector, and a personal computer with LabSolutions CS software for data acquisition and processing.

Chromatographic Conditions and Preparation of Standards. The chromatographic method was adapted from Jayaprakasha et al. (2002). The mobile phase consisted of varying gradients of acetonitrile (A) and 2% aq. acetic acid solution (B), with a flow rate of 0.75 ml/min. The total run time was 25 minutes, the last 10 minutes equilibrating the column for the next run. The wavelength of detection was the λ_{max} of each compound (**2a**; 325 nm; **2l** 300 nm). The injection volume was 10 μl. Table 1 summarizes the chromatographic conditions used for each of the compounds.

Methanolic standard stock solutions (1 mg/ml) were prepared for each of the analyzed compounds. The stock solutions were diluted in methanol to obtain concentrations of 0.01, 0.02, 0.03, 0.04, 0.05, and 0.06 mg/ml. For less concentrated standard samples of **2a** and **2l**, a 1 μg/ml standard stock was prepared from the 1 mg/ml stock, and the stock solutions were diluted in methanol to obtain 100, 50, 20, 10, 5, and 2 ng/ml solutions. All standards were freshly prepared from the stock solutions on the day of analysis. The stock solutions were stored at −20°C. The area under the curve (AUC) versus the concentration of each compound standards was plotted and fitted with linear regression analysis using GraphPad Prism to calculate the slope, intercept, and correlation coefficient and thus determine the linearity of the standard curve (Supplemental Tables 1 and 2). For reproducibility, the experiment was repeated three times, on three separate days, with freshly prepared standard solutions for each compound.

Degradation Study. The degradation study was carried out according to the method outlined by Tønnesen and Karlsen (1985). Compounds **2a** and **2l** were dissolved in methanol (1 mg/ml concentration). The methanolic solution (100 μl) of the compounds was then added to prewarmed PBS (900 μl, 37°C) and placed in the orbital incubator. At time points of 1, 2, 4, 8, 12, 24, 48, and 72 hours, 100 μl of the solution was removed and extracted twice with ethyl acetate (2 × 200 μl). The ethyl acetate extracts were combined and evaporated, and the residues were redissolved in methanol (200 μl) for HPLC analysis. Ten microliters of the original methanolic solutions were removed, evaporated, and redissolved in methanol (200 μl), and this was taken as $t = 0$. The AUC is the total absorbance of the compound at that given concentration and was used for quantification. The degradation profiles of each of the compounds are expressed as percentages of compounds remaining in PBS at the sampled time, with the AUC at $t = 0$ taken as 100%.

The detection and quantification limits for analogs **2a** and **2l** were calculated according to the method outlined in the guidelines of International Committee on Harmonization (2005) (https://www.ich.org/fileadmin/Public_Web_Site/ICH_Products/Guidelines/Quality/Q2_R1/Step4/Q2_R1__Guideline.pdf) using the following formulae:
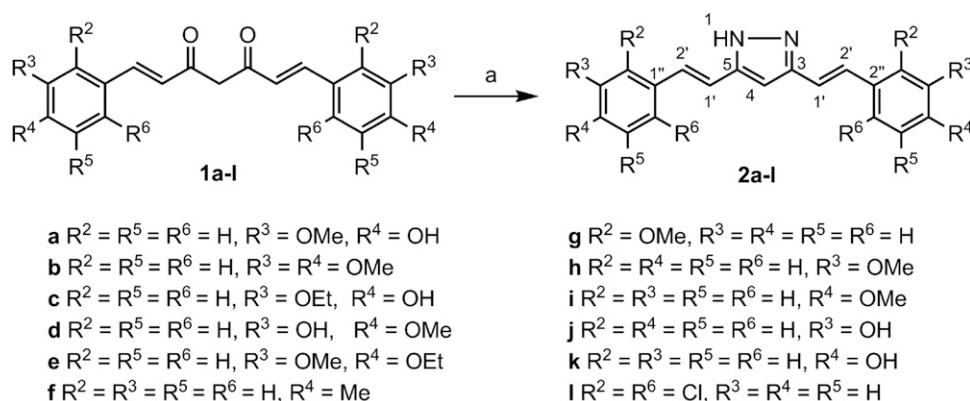
$$\text{Detection limit} = 3\ 3\sigma/\text{slope}$$

$$\text{Quantification limit} = 10\sigma/\text{slope},$$

TABLE 1
HPLC conditions for each of the compounds analyzed

Compound	0–15 min (linear gradient)	15–20 min (linear gradient)	20–25 min (isocratic re-equilibration)
		Solvent gradient % A	
2a	30–70	70–30	30
2l	60–80	80–60	60

A, acetonitrile; B, 2% aq. acetic acid solution.

Scheme 1. Synthesis of 3,5-bis(styryl) pyrazoles **2a-l**. Reagents and conditions: (a) $NH_2NH_2 \cdot H_2O$, AcOH, N,N-dimethyl-formamide (DMF), microwave, 80°C, 5 minutes. For detailed experimental protocols and spectroscopic information, see Supplemental Methods.

a $R^2 = R^5 = R^6 = H$, $R^3 = OMe$, $R^4 = OH$
b $R^2 = R^5 = R^6 = H$, $R^3 = R^4 = OMe$
c $R^2 = R^5 = R^6 = H$, $R^3 = OEt$, $R^4 = OH$
d $R^2 = R^5 = R^6 = H$, $R^3 = OH$, $R^4 = OMe$
e $R^2 = R^5 = R^6 = H$, $R^3 = OMe$, $R^4 = OEt$
f $R^2 = R^3 = R^5 = R^6 = H$, $R^4 = Me$

g $R^2 = OMe$, $R^3 = R^4 = R^5 = R^6 = H$
h $R^2 = R^4 = R^5 = R^6 = H$, $R^3 = OMe$
i $R^2 = R^3 = R^5 = R^6 = H$, $R^4 = OMe$
j $R^2 = R^4 = R^5 = R^6 = H$, $R^3 = OH$
k $R^2 = R^3 = R^5 = R^6 = H$, $R^4 = OH$
l $R^2 = R^6 = Cl$, $R^3 = R^4 = R^5 = H$

where σ is the S.D. of errors in regression of the standard curve generated upon linear regression fitting of the average values of three standard curves ($n = 3$).

The detection and quantification limits for **2a** and **2l** were verified by injecting multiple samples ($n = 6$) at the concentrations of the detection and quantification limits. The accuracy is expressed as the percentage of the S.D. divided by mean values of the six AUC values determined from the injected samples.

General Experimental Procedure for the In Vitro Testing. RPMI 1640 medium, PBS, trypsin/EDTA 10× solution, and 3-(4,5-dimethyl-2-thiazolyl)-2,5-diphenyl-2H-tetrazolium bromide (MTT) were purchased from Sigma Aldrich. Fetal bovine serum (FBS) of Australian origin was purchased from Bovogen. PC3 cells were purchased from American Type Culture Collection (Manasses, VA; CRL-1435). Muse Count & Viability Assay Kit, Muse Annexin V & Dead Cell Assay kit, and Muse Cell Cycle Assay Kit were purchased from Millipore, Australia. A CLARIOstar microplate reader was used to measure the absorbance of MTT formazan at 540 nm. A Muse Cell Analyzer (Merck, Millipore) was used to conduct the annexin V apoptosis and cell cycle analysis assays.

Antiproliferative Assay. PC3 cells were grown in RPMI 1640 supplemented with 10% FBS to ~70–80% confluency before seeding. Antiproliferative activity was determined by the MTT colorimetric assay (Mosmann, 1983). The MTT stock solution (12 mM) was prepared by dissolving 3-(4,5-dimethylthiazol-2-yl)-2,5-diphenyltetrazolium bromide in PBS (5 mg/ml) filtered through a 0.2 μm syringe filter.

The pyrazoles and methotrexate were dissolved in DMSO to make a 200 mM stock. PC3 cells were seeded in 96-well plates at 3000 cells per well and incubated for 24 hours. The DMSO stock solutions were diluted in 10% FBS supplemented RPMI 1640 media; six concentrations of each of the test compounds were added to wells (in triplicate) with the final DMSO concentration of less than 0.1% in each well. DMSO (0.1%) in RPMI 1640 medium was also prepared and used as a vehicle control for each plate and represents 100% growth in this assay. The plates were then incubated for 72 hours (T_{72}).

After 72 hours, the medium was removed from each well and was replaced with 10% MTT stock solution in serum and phenol red–free RPMI 1640 medium (100 μl/well). The plates were then incubated for 3 hours at 37°C before removing the medium and replacing it with DMSO (50 μl/well). After mixing, the plates were placed in the microplate reader, and the absorbance was determined. A control plate was prepared in the same way as above and read 24 hours (T_0) after seeding. The experiment was repeated at least three times on three separate days to give $n = 3$.

The percentage of inhibition of cell growth was then calculated using the following formula:

$$\%\text{Growth inhibition} = 100 - \left(\left(\frac{Abs(T_{72}) - Abs(T_0)}{Abs(DMSO) - Abs(T_0)}\right) \times 100\right).$$

GraphPad Prism was used to determine the GI_{50} values using a nonlinear regression fit after first transforming concentrations to

log scale values. All results were representative of three independent experiments conducted on three separate days.

Annexin V/Propidium Iodide Apoptosis Assay. PC3 cells were seeded in six-well plates at cell densities of 100,000 cells per well and incubated for 24 hours. The pyrazoles **2a** and **2l** were added to the wells at their GI_{50} concentration. DMSO (0.1%) in RPMI medium was used as a vehicle control. The cells were incubated for 72 hours; then they were trypsinized, centrifuged, stained with the Muse Annexin V/Dead Cell kit according to manufacturer's instructions, and then analyzed using, Muse Cell Analyzer. The experiment was conducted in duplicate, with data acquisition of 4000 events, and the experiment was repeated three times on three separate days to give $n = 3$.

A set of experiments was performed following the same procedure as above, but after 72 hours of drug treatment, the medium containing the pyrazoles was removed and replaced with fresh medium, and the cells were incubated for a further 72 hours. Cells were then trypsinized, stained with the Muse Annexin V/Dead Cell kit, and analyzed using the Muse Cell Analyzer. The experiment was conducted in duplicate, with data acquisition of 4000 events, and the experiment was repeated three times on three separate days to give $n = 3$.

Cell Cycle Analysis. PC3 cells were treated in the same way as in the apoptosis assay except, after trypsinization, cells were counted, centrifuged, and fixed with cold ethanol solution 70% (v/v) at 1×10^6 cells/ml. The cells were left to fix overnight at -20°C, then centrifuged, stained with the Muse Cell Cycle kit according to the manufacturer's instructions, and then analyzed using the Muse Cell Analyzer. The experiment was conducted in duplicate with data acquisition of 5000 events, and the experiment was repeated at least four times on four separate days to give $n = 4$.

TABLE 2
GI_{50} values of 3,5-bis(styryl)pyrazoles **2a-l** in PC3 cells[a]

Compound	GI_{50}
	μM
Methotrexate	0.012 ± 0.008
2a	0.85 ± 0.34
2b	39.8 ± 7.8
2c	3.4 ± 0.1
2d	77.8 ± 6.7
2e	69.3 ± 9.4
2f	>500[b]
2g	4.1 ± 0.14
2h	26.9 ± 1.7
2i	39.8 ± 7.8
2j	24.2 ± 0.5
2k	28.9 ± 2.5
2l	2.21 ± 0.33

[a]Data represent the mean ± S.D. of three independent replicates ($n = 3$).
[b]Compound showed no growth inhibitory activity in PC3 cells at the highest tested concentration (500 μM).
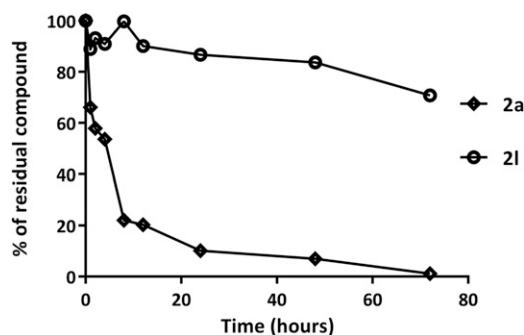
Fig. 1. Representative degradation profiles of pyrazoles **2a** and **2l** in PBS (pH 7.4) at 37°C in darkness over a period of 72 hours. Residual concentrations of each compound are expressed as percentages with respect to the concentration at time zero ($t = 0$, 100%).

Experimental Procedure for the Tubulin and Microtubule Studies. The determination of the effects of the pyrazoles on the assembly kinetics of tubulin in vitro, the K_d for the binding of the analogs to tubulin, and effect on microtubules in cells were performed as described previously (Panda et al., 2005).

Tubulin Purification. Tubulin was isolated from goat brain by two cycles of polymerization, and depolymerization as described previously (Panda et al., 2005).

Light Scattering. Tubulin (12 μM) was incubated with different concentrations of **2a** and **2l** in PEM [50 mM 1,4-piperazinediethane-sulfonic acid (PIPES), 1 mM EGTA, and 3 mM MgCl$_2$] buffer, pH 6.8, on ice for 10 minutes. After 10 minutes of incubation, 10% DMSO and 1 mM GTP was added to the reaction mixture, and polymerization was monitored at 37°C in a spectrophotometer, Spectramax M2^e, at 350 nm for 30 minutes. The experiment was repeated three times, and the percentage inhibition of tubulin polymerization was calculated. The IC_{50} of polymerization was determined by fitting the data in dose-response inhibition curve in the GraphPad Prism Software.

Sedimentation Assay. Tubulin (12 μM) was polymerized at 37°C for 30 minutes in the presence and absence of **2a** and **2l** as in light scattering. After 30 minutes, the polymerized microtubules were pelleted by centrifuging it at 33,000g, 30°C for 30 minutes. The supernatant was separated, and the amount of polymerized microtubules was calculated by loading the supernatant and pellet on the SDS-PAGE gel followed by intensity quantification of bands by ImageJ or by quantifying the supernatant protein concentration by Bradford's assay.

Determination of Dissociation Constant. Tubulin (2 μM) was incubated with and without different concentrations of **2a** or **2l** in 25 mM PIPES buffer pH 6.8 for 10 minutes at room temperature. After incubation, the spectra of tryptophan emission were recorded in a spectrofluorometer (FP-6500; JASCO, Tokyo, Japan) by exciting the sample at 295 nm and recording the spectra. The fluorescence intensity at λ_{max} was noted, and it was fitted in the following equation in GraphPad Prism software to determine the K_d:

$$\Delta F = \Delta Fmax \times \frac{([P_0] + [L_0] + K_d) - \sqrt{([P_0] + [L_0] + K_d)^2 - 4[P_0][L_0]}}{2[P_0]},$$

where ΔF_{max} is the highest fluorescence intensity, P_0 is the concentration of protein, and L_0 is the concentration of **2a** or **2l**.

Determination of Tubulin Binding Site of Pyrazole 2l. Competitive inhibition with colchicine: tubulin (5 μM) was incubated without or with 10 and 20 μM of **2l** on ice for 10 minutes in 25 mM PIPES buffer pH 6.8 and then incubated with 10 μM colchicine for 45 minutes at 37°C. The fluorescence spectra (370–500 nm) were monitored using a fluorescence spectrophotometer (FP-6500; JASCO) with excitation of the samples at 340 nm.

Competitive Inhibition with Vinblastine and Crocin. First, we examined whether **2l** could inhibit the binding of vinblastine to tubulin using BODIPY-FL-Vinblastine, a fluorescent analog of vinblastine (Lin and Chen, 2013). Tubulin (3 μM) was incubated with 200 nM of BODIPY-FL-vinblastine (V12390; Thermo Scientific) on ice for 10 minutes in 25 mM PIPES buffer pH 6.8. The reaction mixture was then incubated without or with 1 and 5 μM of **2l** for 10 minutes on ice. The change in fluorescence of BODIPY-FL-Vinblastine was observed in a spectrofluorometer (FP-6500; JASCO) by exciting at 488 nm and taking emission spectra from 498 to 540 nm.

Recently, it has been reported that vinblastine and crocin share their binding sites on tubulin (Hire et al.; 2017; Sawant et al., 2019). Therefore, we examined whether **2l** could inhibit the binding of crocin to tubulin. Crocin (5 μM) was incubated with 10 μM tubulin for 10 minutes on ice in PEM buffer pH 6.8. The reaction mixture was then incubated with 10 μM **2l** for 10 minutes on ice and then change in optical density (OD) from 410 to 500 nm was observed in a spectrophotometer (V-730; JASCO).

Docking of 2l with Tubulin. The structure of **2l** was drawn in PubChem Sketcher (V2.4) and the Protein Data Bank (PDB) coordinates of **2l** were generated in PRODRG server (Schüttelkopf and van Aalten, 2004). The Autodock Vina tool was used for docking of **2l** on tubulin (Trott and Olson, 2010) as described previously (Rane et al., 2017; Hura et al., 2018). The crystal structure of tubulin (PDB identifier 5LYJ) was used for docking **2l** with tubulin. The coordinates of all other proteins and molecules (tubulin-tyrosine ligase, CA-4, glycerol, stathmin, etc.) in 5LYJ, except one α and one β subunit of
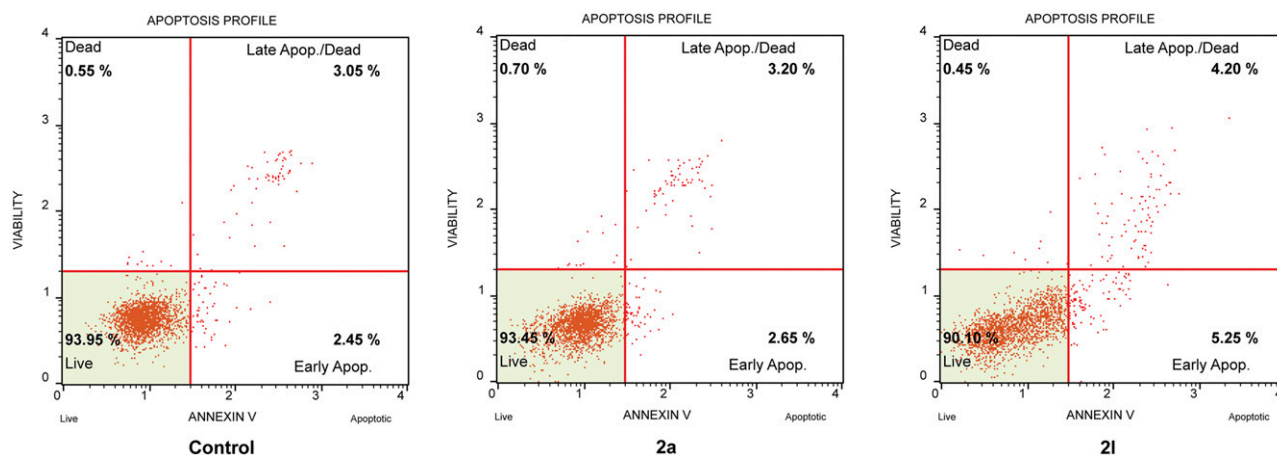
Fig. 2. Representative dot plots from the annexin V/PI apoptosis assay of PC3 cells treated with the GI_{50} concentrations of **2a** and **2l** for 72 hours. DMSO (0.01%) was used as the vehicle control.
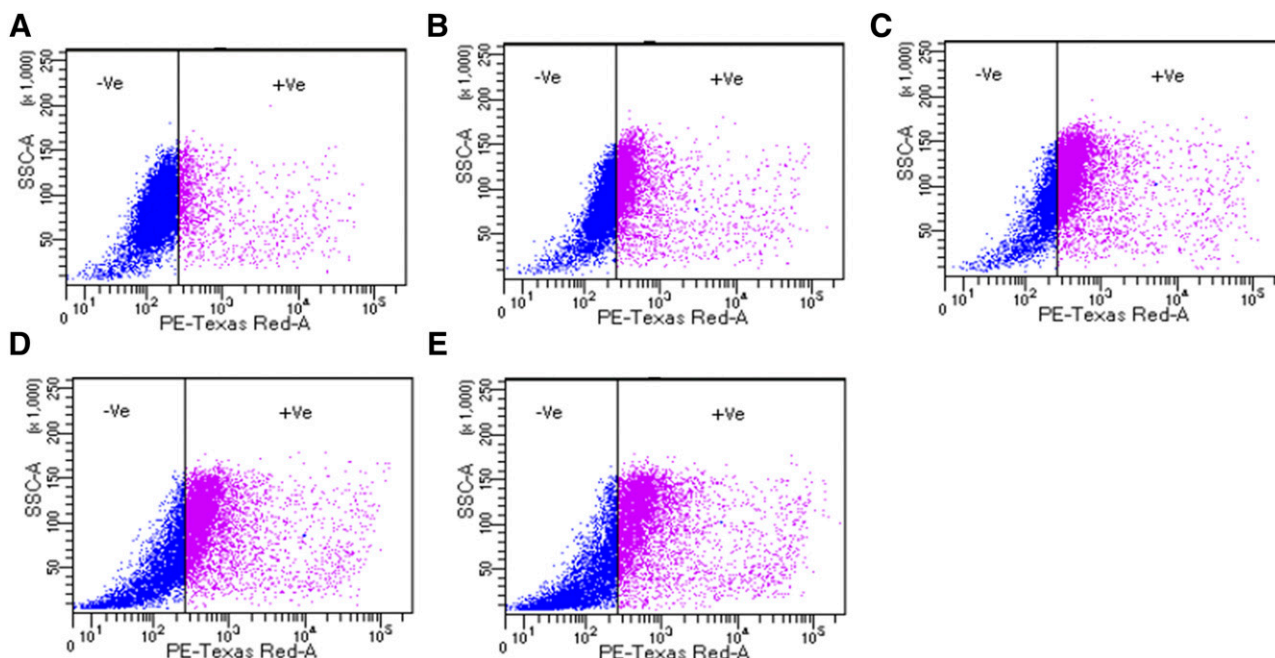
Fig. 3. Live dead assay to determine the percentage of cell death after treatment with (A) 0.1% DMSO, (B) **2a** (4 μM), (C) **2a** (8 μM), (D) **2l** (4 μM), and (E) **2l** (8 μM). The blue dots represent the PI-negative (live) cells, and magenta dots represent PI-positive (dead) cells. The experiment was repeated three times, and the quantitation is represented as mean ± S.D. of three independent sets in Table 3.PE, phycoerythrin; SSC, side scatter; -Ve, negative; +Ve, positive

tubulin were deleted using PyMOL (DeLano, 2002). The final coordinates used for docking had one α subunit, one β subunit, one GDP, one GTP, one calcium ion, and two magnesium ions. Initially global docking was performed by covering the whole molecule in a grid box of 72 × 102 × 100 Å, with grid spacing of 1 Å. The global docking was performed five times with exhaustiveness of 100 (the number of times the calculation is repeated), and each set of docking produced nine conformations. The greatest number of conformations were found to interact with two sites on the protein (16 conformations at the interface of the α- and β-dimers and 19 conformations at the taxol site) (Jaghoori et al., 2016). These two sites were thus chosen to perform local docking, which was performed in a grid box of 72 × 56 × 58 Å for colchicine and 126 × 86 × 82 Å for epothilone, with a grid spacing of 0.375 Å. The conformation with minimum binding energy was chosen to analyze the interaction with tubulin. Control docking with epothilone was performed in a similar way to validate the docking protocol. The coordinates of epothilone and colchicine were obtained from their PDB structures 4O4I and 1SA0, respectively. The interaction of the docked conformers with tubulin was further analyzed in University of California, San Francisco's (UCSF) Chimera version 1.11 (Pettersen et al., 2004) to determine the amino acid residues in the binding pocket and the residues within 4 Å of **2l** to determine the possible hydrogen bonding interactions.

Competitive Inhibition with Paclitaxel. Tubulin (12 μM) was incubated with different concentrations (0, 2, 5, 10, 20, and 30 μM) of **2l** for 10 minutes on ice in PEM buffer pH 6.8. Different concentrations (2, 5, and 7 μM) of paclitaxel were added to the reaction mixtures for each concentration of **2l** and incubated for 10 minutes on ice. The polymerization reaction was monitored immediately after adding 1 mM GTP in Spectramax M2e by taking OD at 350 nm. The percentage inhibition of tubulin polymerization versus concentration of **2l** was plotted in a Lineweaver-Burk plot at different concentrations of paclitaxel to determine the nature of inhibition.

Effects of 2l on the Polymerization of *spn*FtsZ. Purified *spn*FtsZ (10 μM) was polymerized in the presence of 1 mM GTP at 37°C as described previously (Dhaked et al., 2019). The polymerization reaction was monitored in a spectrofluorometer

(FP-6500; JASCO) with the wavelength for both excitation and the emission at 400 nm. Polymerization of *spn*FtsZ was also observed with prior incubation of the protein with 20 μM **2a** and **2l** in ice for 10 minutes.

Alkaline Phosphatase Assay. Two units of alkaline phosphatase was taken in glycine-NaOH buffer pH 10.4 with 1 mM $MgCl_2$ and 0.1 mM $ZnCl_2$. Two hundred fifty micromolars of *para*-nitrophenylphosphate was mixed with the reaction mixture in a cuvette. The reaction mixture was immediately put in a spectrophotometer, and the conversion of the yellow colored product was monitored by taking the OD at 410 nm. A similar experiment was performed with both **2a** and **2l** by incubating 20 μM each of **2a** and **2l** for 10 minutes with alkaline phosphatase on ice.

Sulphorhodamine B Assay. The GI_{50} in HeLa cells was determined by sulphorhodamine B assay as described previously (Vichai and Kirtikara, 2006). Briefly, HeLa cells were seeded in tissue culture treated 96-well plate (10,000 cells/well). After attachment, the cells were treated with different concentrations of **2a** and **2l** and incubated for 24 hours followed by fixation with 50% trichloroacetic acid for 1 hour at 4°C. The plates were then washed, dried, and stained with 0.4% sulphorhodamine B for 1 hour at room temperature. After drying of the plates, the dye was dissolved in 10 mM Tris pH 10.5, and the absorbance was measured at 520 nm in Spectramax M2^e. The percentage

TABLE 3

Quantification of percentage of live and dead cells after treatment with bis(styryl)pyrazoles **2a** and **2l**

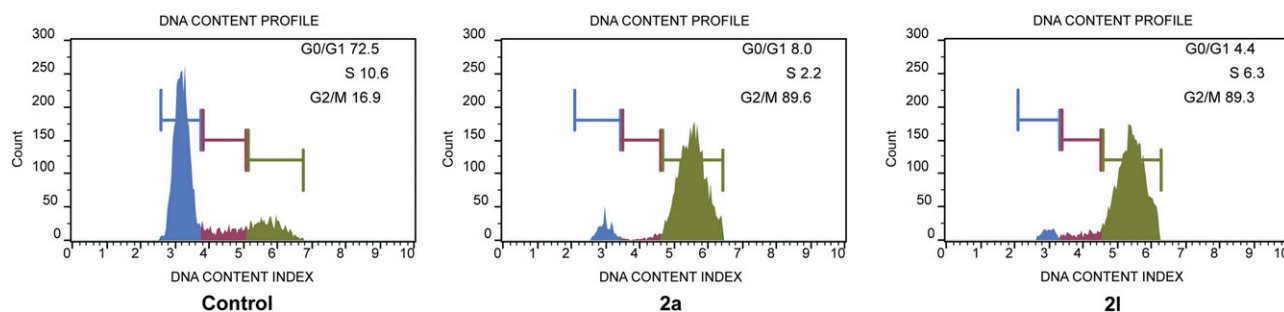| Compound	Dead cells
	%
Control	15.4 ± 1.2
2a (4 μM)	35.9 ± 8.9
2a (8 μM)	54.5 ± 12.2
2l (4 μM)	49.4 ± 10.8
2l (8 μM)	47.4 ± 6.0

Fig. 4. Representative cell cycle histograms for PC3 cells 72 hours after treatment with vehicle control (0.01% of DMSO) and GI_{50} concentrations of analogs **2a** and **2l**, where blue, magenta, and green represent the numbers of cells in the G_0/G_1, S, and G_2/M phases, respectively.

inhibition of cell proliferation at each concentration was determined by the formula

$$\%Inhibition\ of\ cell\ proliferation = 100 - \left\{\left(\frac{N_t - N_0}{N_c - N_0}\right) \times 100\right\},$$

where N_t is OD of the wells where **2a** or **2l** was added, N_0 is the OD of the wells at the time of **2a** or **2l** addition, and N_c is the OD of the wells of 0.1% DMSO treatment. This percentage inhibition was then fitted in dose-response inhibition curve in GraphPad Prism software.

Immunofluorescence Microscopy. The coverslips were first coated with poly-L-lysine, and then cells were added onto coverslips (25,000 cells/well) for attachment. After attachment, cells were treated with different concentrations of **2a** and **2l** and incubated for 24 hours. Cells were then fixed with 4% formaldehyde and permeabilized with 100% chilled methanol. Two percent bovine serum albumin was used for blocking the nonspecific binding of the antibody, and then the anti–α-tubulin antibody (Sigma) was added to cells and incubated for 3 hours at 37°C. After washing of primary antibody, secondary antibody tagged with fluorescein isothiocyanate (Sigma) was added to the cells and incubated for 1.5 hours. The coverslips were mounted on clean glass slides using the mounting media having 4′,6-diamidino-2-phenylindole, purchased from Vector Laboratories, and observed under a fluorescence microscope (CSU-XI; Yokogawa).

Live-Dead Assay. The percentage of the live and dead cell was determined by propidium iodide (PI) staining. The cells were seeded up to 50% confluency in T25 flasks and then incubated with 4 and 8 μM of **2a** and **2l** for 24 hours. The cells were trypsinized, pelleted, and resuspended in PBS with a final concentration of cells approximately 1 million per ml. The cells were stained with PI and then analyzed by flow cytometry for PI-positive and PI-negative cells. Ten thousand cells were counted in each case. The experiment was repeated three times.

Statistical Analysis. "$\pm$" represents S.D., and P values were calculated using Student's t test.

Results

Synthetic Chemistry. The synthesis of the bis(styryl) pyrazoles **2a-l** takes advantage of our recently described

microwave-assisted synthesis of curcuminoids (Groundwater et al., 2017), in which the total reaction time was shortened to 10 minutes and the analytically pure compounds were mostly obtained by the simple recrystallization from ethanol of the crude solid obtained from the acid hydrolysis of the boron-containing intermediate. The ready availability of these synthetic intermediates **1a-l** lead to the preparation of
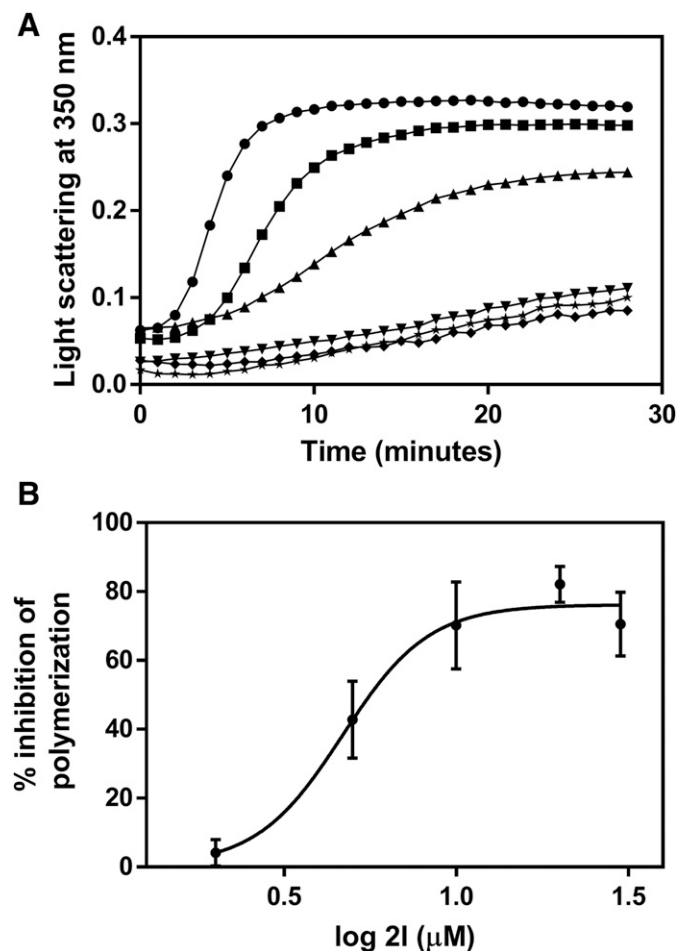

Fig. 5. Inhibition of tubulin polymerization by 3,5-bis(styryl)pyrazole **2l** monitored by light scattering. Tubulin (12 μM) was polymerized in the presence of 10% DMSO and 1 mM GTP without (●) or with 2 (■), 5 (▲), 10 (▼), 20 (♦), and 30 (★) μM **2l**. The polymerization kinetics were followed by light scattering at 350 nm. The experiment was repeated three times. (A) Representative graph of the light scattering of tubulin in the presence and absence of **2l**. (B) The inhibition of tubulin polymerization at different concentrations of **2l**. Error bars represent S.D.
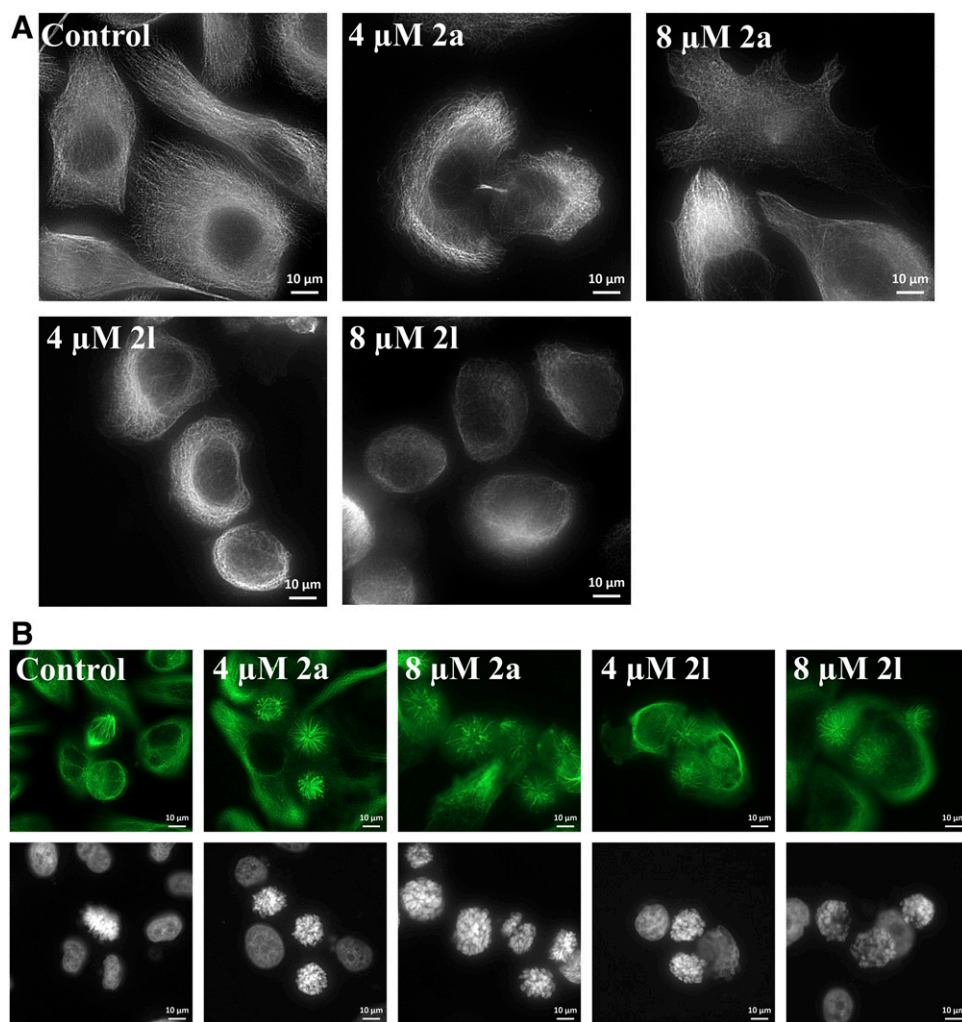
TABLE 4

Percentage of live and dead PC3 cells 72 h after the removal of the 3,5-bis(styryl)pyrazoles **2a** and **2l**[a]

Compound	Live cells	Dead cells
	%	
Control	95.7 ± 2.2	3.9 ± 1.9
2a	86.7 ± 3.5	12.3 ± 3.7
2l	67.5 ± 9.1	29.4 ± 9.8

[a]Data represent the mean ± S.D. of three independent replicates ($n = 3$).

Fig. 6. Effect of **2l** and **2a** on microtubules of PC3 cells. (A) Interphase microtubules of PC3 cells before and after the treatment with 4 and 8 μM of **2a** and **2l** (grayscale image). (B) Mitotic microtubules (green) and corresponding DNA (grayscale image). Scale bars, 10 μm.

noncurcuminoid analogs such as 3,5-bis(stryryl)pyrazole analogs **2a-l** for biologic evaluation, via the cyclization with hydrazine in an acid-catalyzed microwave-assisted condensation, to generate the respective **2a-l** (Scheme 1).

Antiproliferative Activity of 3,5-Bis(styryl)pyrazoles 2a-l in PC3 Cells. The growth inhibitory effect of all the 3,5-bis(styryl)pyrazoles **2a-l** on the PC3 cell line was determined by the MTT assay (Table 2), which was validated by the trypan blue exclusion cell count. Methotrexate was used as a positive control, with a GI_{50} value (obtained in this study) of 0.012 ± 0.008 μM, which is within the ranges of the reported GI_{50} values in PC3 cells for methotrexate (0.001–0.1 μM) (Derenne et al., 2010; Marques et al., 2010; Serova et al., 2011). Two compounds (**2a** and **2l**) had GI_{50} values in the low micromolar range (<2.5 μM) (Supplemental Fig. 1) and were thus selected for further biologic evaluation, as well as degradation and solubility studies.

Degradation Studies. We evaluated the stability and solubility of the two analogs selected for extensive biologic testing, **2a** and **2l**, under simulated physiologic conditions (pH 7.4, 37°C), and the degradation kinetics are summarized in Fig. 1. After 24 hours under the simulated physiologic conditions, 10% of analog **2a** remained, whereas 71% of analog **2l** remained after 72 hours (Supplemental Figs. 2 and 3).

The Effect of 3,5-Bis(styryl)pyrazoles 2a and 2l on the Induction of Apoptosis in PC3 Cells. The two selected analogs (**2a** and **2l**) did not induce apoptosis at their GI_{50} concentrations, as determined by the annexin V/PI apoptosis assay. PC3 cells were treated at the GI_{50} of analogs **2a** and **2l**, with cells treated with DMSO (0.01%) as the vehicle control. The cells were then incubated for 72 hours, stained with annexin V/PI, and analyzed. The representative dot plots depicting the results from this apoptosis assay are shown in Fig. 2; cells treated with and without these compounds maintained more than 90% viability, indicating that they did not undergo apoptosis when treated at the GI_{50} concentrations. However, the cells died after treatment with higher concentrations of **2a** and **2l** (4 and 8 μM), as shown by the increasing number of PI-positive cells after PI staining and counting 10,000 cells by flow cytometry (Fig. 3; Table 3). In addition, we quantified the extent of apoptosis in three other cell lines, namely, lung carcinoma (A549), skin melanoma (B16F10), and liver carcinoma (Huh-7), at similar concentrations of **2a** and **2l**. The compounds induced apoptosis in all three cell lines in a concentration-dependent manner (Supplemental Fig. 4; Supplemental Table 3).

The Effect of 3,5-Bis(styryl)pyrazoles 2a and 2l on the Cell Cycle of PC3 Cells. A cell cycle analysis was conducted
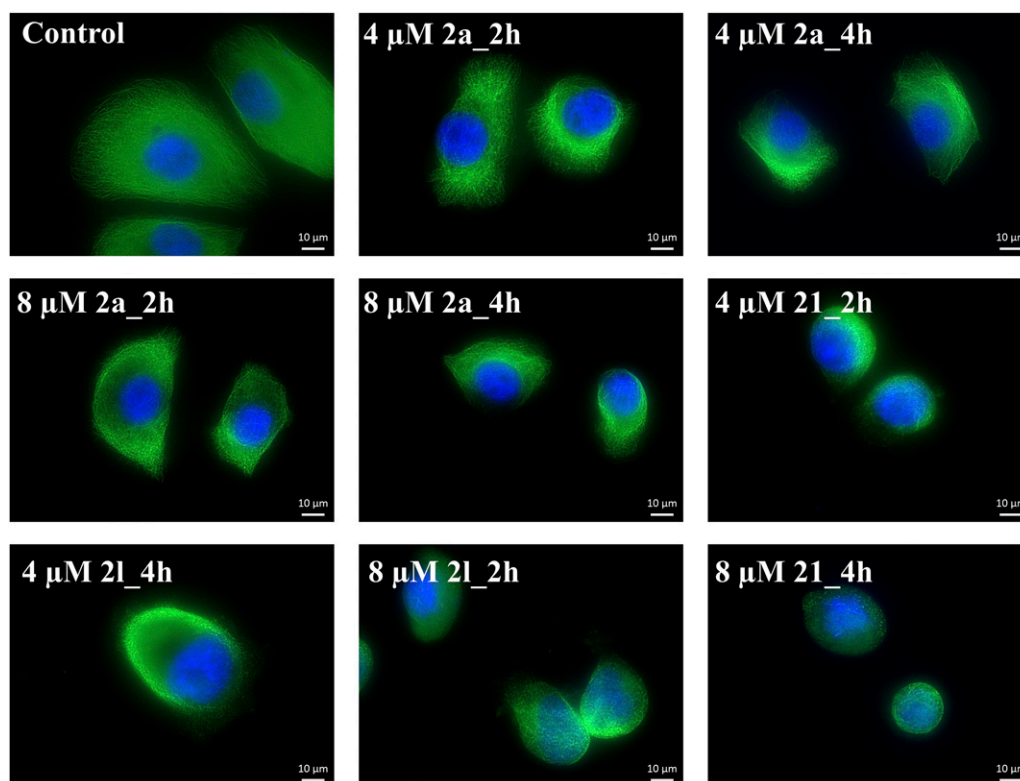
Fig. 7. Effects of **2l** and **2a** on microtubules of PC3 cells after 2 and 4 hours of **2a** and **2l** treatment. Interphase microtubules (green) of PC3 cells before and after the short exposure of 4 and 8 µM of **2a** and **2l**. DNA (blue) was stained with Hoechst 33258. Scale bars, 10 µm.

to determine the effects of 3,5-bis(styryl)pyrazoles **2a** and **2l** on cell division. PC3 cells were treated for 72 hours at the GI_{50}s of these compounds, with cells treated with 0.01% of DMSO used as the vehicle control. The cell cycle analysis showed a significant increase in the percentage of cells in the G_2/M phase when treated with the 3,5-bis(styryl)pyrazoles at their GI_{50} concentrations, in comparison with the control (Fig. 4; Supplemental Table 4).

Assessment of the Outcome of Mitotic Arrest Induced by 3,5-Bis(styryl)pyrazoles 2a and 2l. To evaluate the potential of 3,5-bis(styryl)pyrazoles **2a** and **2l** as effective agents for the treatment of CRPC, we examined whether cell death results from mitotic arrest in PC3 cells. PC3 cells were treated for 72 hours with 3,5-bis(styryl)pyrazoles **2a** and **2l** (at their GI_{50}s), and the medium containing the compounds was then removed and replaced with fresh medium. The cells were incubated for a further 72 hours before being stained with annexin V/PI and analyzed. The percentage of cell death 72 hours after the removal of **2a** and **2l** (Supplemental Fig. 5; Table 4) was lower than the mitotic block after 72 hours treatment with **2a** and **2l** (Supplemental Table 4), suggesting that the effects of the compounds on PC3 cells are reversible.

Determination of the Effect of 3,5-Bis(styryl)pyrazoles 2a and 2l on Tubulin Polymerization. Since both the compounds, **2a** and **2l**, caused a mitotic block, a characteristic of most antitubulin agents (Mukhtar et al., 2014), the effect of **2a** and **2l** on tubulin was investigated. 3,5-Bis(styryl)pyrazole **2l** inhibited the polymerization of purified tubulin (Fig. 5), inhibiting both the rate and extent of tubulin assembly, as monitored by light scattering. The extent of inhibition of tubulin polymerization by the compound was also

determined by the sedimentation assay (Supplemental Fig. 6). The IC_{50} of 3,5-bis(styryl)pyrazole **2l** for tubulin polymerization was found to be 4.7 ± 1.2 µM by light scattering and 4 ± 1.5 µM by the sedimentation assay.

The effect of analog **2a** on the polymerization of purified tubulin was also determined by light scattering and sedimentation assay (Supplemental Fig. 7). Unlike the pyrazole **2l**, analog **2a** was not able to inhibit the tubulin polymerization in vitro (Supplemental Fig. 7).

Effect of 3,5-Bis(styryl)pyrazoles 2a and 2l on Microtubules of PC3 Cells. Next, the effects of 3,5-bis(styryl) pyrazoles **2a** and **2l** on the microtubules of PC3 cells were examined by fluorescence microscopy. Cells were seeded on poly-L-lysine coated coverslips and treated with 4 and 8 µM of **2a** or **2l**. Both the compounds caused the depolymerization of the interphase microtubules in PC3 cells (Fig. 6A). As in the control cells, thread-like microtubule structures can be seen, which were well spread in the cytoplasm of the cells. These thread-like structures were not properly visible in cells treated with **2a** and **2l**, indicating that the interphase microtubules were depolymerized by the treatment with these drugs (Fig. 6A). Although both **2a** and **2l** also strongly depolymerized spindle microtubules and caused the formation of abnormal spindles in PC3 cells (Fig. 6B), the effects of **2l** on interphase microtubules were more pronounced (Supplemental Fig. 8A). A normal mitotic cell with spindle microtubules is shown in the Fig. 6B control panel (arrow). In treated cells, abnormal multipolar spindles can be seen, and the number of mitotic cells per field increased significantly after the treatment with **2a** and **2l**, which also confirms that these compounds cause mitotic block (Fig. 6B; Supplemental Fig. 8B). In the control cells,
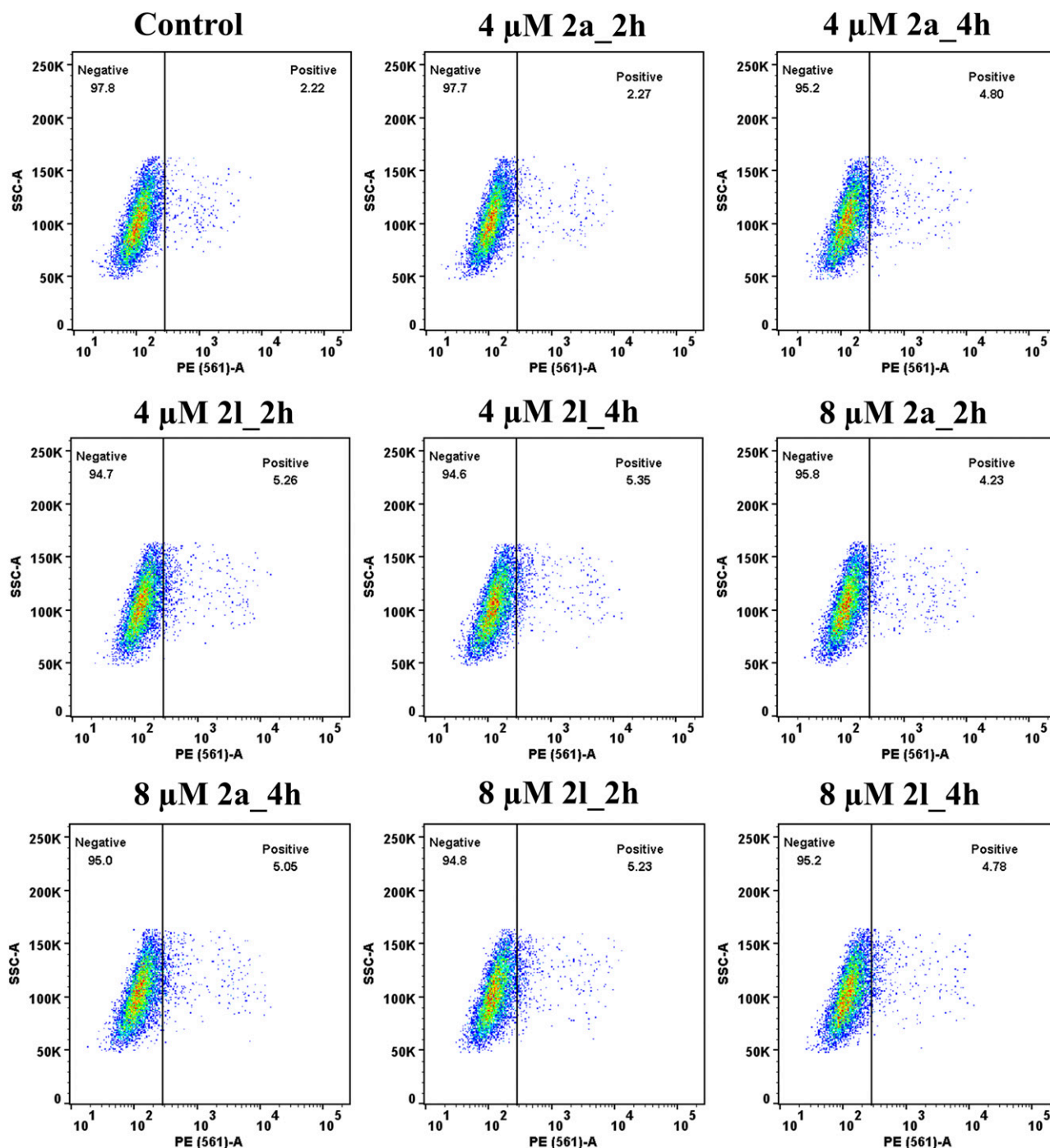
Fig. 8. Live dead assay to determine the percentage of cell death after treatment with 4 and 8 μM of **2a** and **2l** for 2 and 4 hours. The experiment was repeated three times, and the quantitation is represented as mean $\pm$ S.D. of three independent sets in Supplemental Table 5.PE, phycoerythrin; SSC, side scatter

DNA is aligned on the metaphase plate (arranged more compactly in a straight line), whereas after treatment the DNA is scattered and unable to align. We also determined the effect of **2a** and **2l** on the microtubules of HeLa cells. The GI_{50} of **2a** and **2l** was determined to be 2.6 $\pm$ 1.2 and 2.4 $\pm$ 0.5 μM, respectively (Supplemental Fig. 9, A and B). Both **2a** and **2l** depolymerized interphase and spindle microtubules in HeLa cells (Supplemental Fig. 9, C and D), with the depolymerization of microtubules by **2l** being more pronounced than that produced by **2a** (Supplemental Fig. 10A). The population of mitotic cells also increased upon

treatment with **2a** and **2l,** suggesting that the compounds cause mitotic block (Supplemental Fig. 10B).

Kinetics of Microtubule Depolymerization and Cell Death after Treatment of PC3 Cells with 3,5-Bis(styryl) pyrazole 2a. To examine whether microtubules are the primary targets of **2a** and **2l**, we compared the kinetics of microtubule disassembly and cell death upon treatment with both compounds. PC3 cells were incubated without or with either 4 and 8 μM of **2a** and **2l** for 2 and 4 hours. The fluorescence intensity of microtubules was found to be

strongly reduced after both 2- and 4-hour treatment with **2a** and **2l** (Fig. 7; Supplemental Fig. 11). The fluorescence intensity of microtubules in vehicle treated cells was determined to be 1525 ± 229 (a.u.), dropping to 1054 ± 112 and 913 ± 105 (a.u.) after treatment with 4 μM **2a** for 2 and 4 hours, respectively, and 825 ± 61 and 771 ± 54 (a.u.) after treatment with 4 μM **2l** for 2 and 4 hours, respectively (Fig. 7; Supplemental Fig. 11). The fluorescence intensity of the microtubules was reduced by 54 and 57% in the presence of 8 μM **2a** for 2 and 4 hours, and 41 and 72% in the presence of 8 μM **2l** for 2 and 4 hours, respectively (Fig. 7; Supplemental Fig. 11). These results indicate that treatment with both **2a** and **2l** led to the formation of depolymerized microtubules within a short time period. In contrast, treatment with 4 and 8 μM **2a** and **2l**, for 2 or 4 hours, did not induce cell death in PC3 cells (Fig. 8; Supplemental Table 5), indicating that the depolymerization of microtubules preceded cell death upon treatment with **2a** or **2l** and that microtubules are the primary targets of both **2a** and **2l** in PC3 cells.

Binding of 3,5-Bis(styryl)pyrazole 2l to Tubulin. Since **2a** and **2l** caused microtubule depolymerization, we characterized the binding of **2a** and **2l** with tubulin; the binding of **2l** with tubulin was examined by monitoring the tryptophan fluorescence of tubulin (Bhattacharyya et al., 2010). The fluorescence of tubulin was found to be reduced in the presence of **2l**, indicating that the compound binds to tubulin (Fig. 9). The change in the fluorescence intensity of tubulin in the presence of **2l** was plotted in a binding isotherm, which yielded a K_d of 0.4 ± 0.1 μM for the binding interaction.

The binding affinity of **2a** to tubulin was also determined (Supplemental Fig. 12), and it was found that it binds to tubulin with a much weaker affinity (K_d, 4.6 ± 1.1 μM) than **2l** (K_d, 0.4 ± 0.1 μM), a possible explanation for the weak effect of **2a** on the polymerization of purified tubulin and interphase cellular microtubules.

Determination of Binding Site of 3,5-Bis(styryl)pyrazole 2l on Tubulin. Pyrazole **2l** binds to tubulin with higher affinity than **2a**, and we have determined the binding site of **2l** on tubulin. Tubulin has three well defined binding sites for small molecules: the taxane, vinca alkaloid, and colchicine sites (Supplemental Fig. 13). Compounds that bind to the vinca alkaloid and colchicine sites generally destabilize microtubules, so we first checked the binding of **2l** to these binding sites.

The fluorescence intensity of colchicine and BODIPY-FL-vinblastine increases upon binding to tubulin, whereas the absorbance of crocin, a vinca domain binder, increases upon binding to tubulin. If **2l** inhibits the binding of colchicine to tubulin, the fluorescence of colchicine-tubulin complex should be reduced in the presence of **2l**. However, the prior incubation of **2l** with tubulin did not reduce the fluorescence of colchicine-tubulin complex, indicating that **2l** does not bind to the colchicine site on tubulin (Supplemental Fig. 14A). To check the binding of **2l** at the vinblastine site, we used BODIPY-FL-vinblastine and crocin. There was no change in the fluorescence of the BODIPY-FL-vinblastine-tubulin complex or the absorbance of the crocin-tubulin complex, respectively, upon prior incubation with **2l**, indicating that **2l** does not bind to the vinblastine site on tubulin (Supplemental Fig. 14, B and C).

Consequently, to determine the putative binding site, we performed molecular docking with the tubulin crystal structure
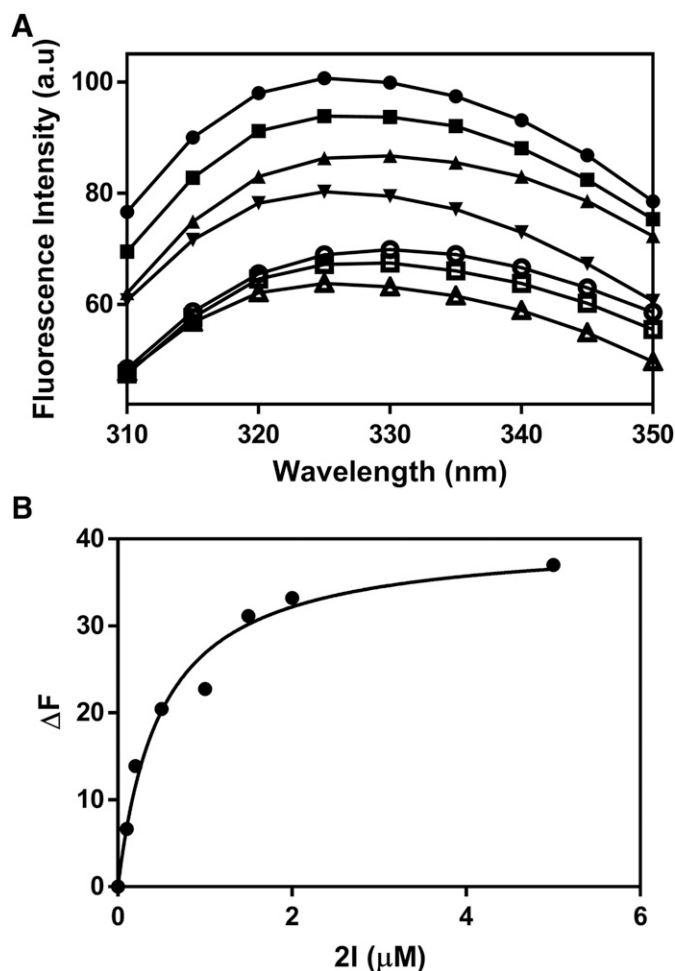

Fig. 9. Determination of the K_d of the tubulin-**2l** complex. (A) The fluorescence of tubulin reduced with increasing concentration of **2l**: 0 (●), 0.1 (■), 0.2 (▲), 0.5 (▼), 1.5 (○), 2 (□) and 5 (△) μM. (B) The difference in the fluorescence intensity (ΔF) (at 340 nm) of tubulin in the presence of various concentrations of the compound was fitted in a binding equation. The experiment was repeated three times.

(PDB identifier 5LYJ) as described previously (Rane et al., 2017; Hura et al., 2018). We found that most conformations of **2l** were interacting with two distinct sites on tubulin; the paclitaxel binding site on β-tubulin (Fig. 10) and the interface of the α- and β-tubulin heterodimer (Supplemental Fig. 15), near the colchicine site. To further validate the docking, we docked epothilone, a paclitaxel site binder, with tubulin. The root mean square deviation of the docked conformation of epothilone to the epothilone conformation present in complex with tubulin (PDB identifier 4O4I) was found to be 1 Å, confirming that the docking protocols were appropriate (Fig. 11) (Hura et al., 2018). Since competitive binding data with colchicine showed that **2l** does not bind to the colchicine site (Supplemental Fig. 14A), we further analyzed the docking data only for paclitaxel site.

We found that **2l** possibly forms 2 hydrogen bonds in the paclitaxel binding site, with the peptide backbone of T273 (2.2 Å) and P271 (2.6 Å) (Fig. 12). Further analysis of the docking gave the binding energy of **2l** with tubulin, which was found to be −8.4 kcal/mol, whereas that of epothilone was found to be −9.1 kcal/mol. Taxol also forms a similar hydrogen bond with the peptide backbone of T273 (3.0 Å).
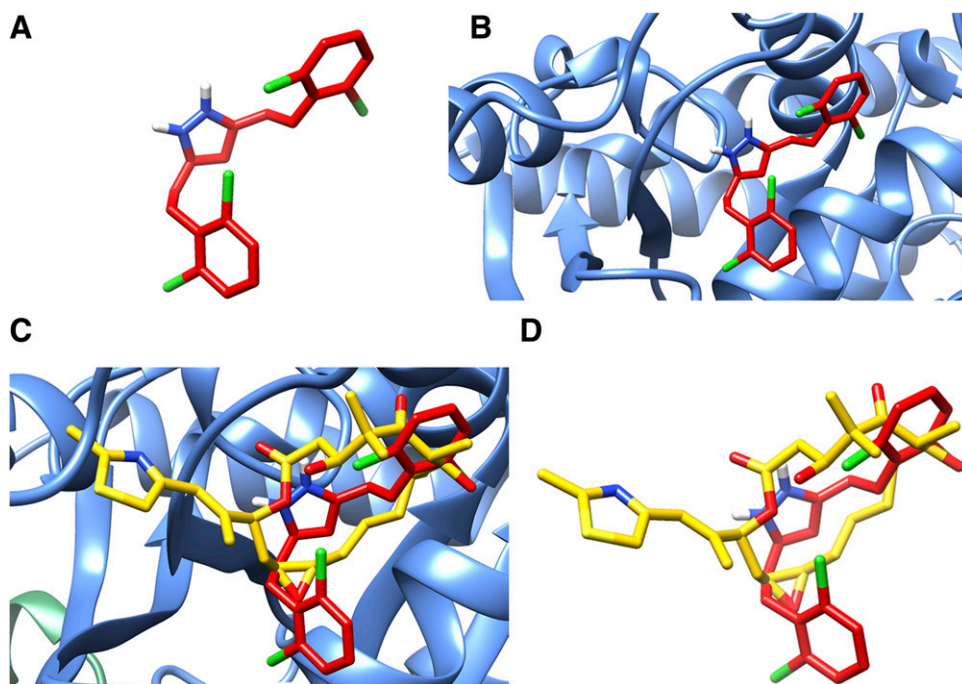
Fig. 10. Docking of **2l** on tubulin. (A) Structure of **2l** shown in red sticks. (B) Conformation of **2l** (red sticks) docked with beta-tubulin (blue ribbon) with least binding energy. (C) Docked conformation of epothilone (yellow sticks) and **2l** (red sticks) with beta-tubulin (blue ribbons) showing epothilone; **2l** goes to the same binding pocket on beta-tubulin. (D) Magnified view of overlap between **2l** and epothilone after docking.

In addition, paclitaxel also forms other hydrogen bonds, with R358 (3.3 Å), Q278 (3.4 Å), H226 (2.6 Å), and the peptide backbone of R358 (3.1 Å) (Snyder et al., 2001; Yadava et al., 2015).

We also analyzed the binding pocket of both epothilone and **2l** on beta-tubulin and found that there were 12 residues that are common to both **2l** and epothilone (Table 5), showing that **2l** and epothilone share the same binding pocket. Since the taxol binding pocket has hydrophobic residues in the H7 helix, M loop, and β strand of S7, S9-10, (Ranade et al., 2016), it is possible that **2l** also makes some hydrophobic interactions within the binding pocket.

To elucidate the binding site of **2l** on tubulin, we performed a competitive inhibition experiment of **2l** with paclitaxel. The effects of **2l** on the polymerization of tubulin in the presence of different concentrations of paclitaxel were determined. **2l** exerted a stronger inhibitory effect on tubulin polymerization in the presence of low concentrations of paclitaxel. The percentage inhibition at each concentration of taxol was plotted in the Michaelis-Menten equation (Fig. 13A). The resulting curves showed a typical competitive inhibition pattern, where V_{max} (maximum percentage of inhibition) remains unchanged ($P > 0.05$). Furthermore, the Lineweaver-Burk plot indicated that the nature of inhibition is competitive (Fig. 13B), as the plot shows that the affinity of the substrate **2l** changes with changes in the paclitaxel concentration, as suggested by a decrease in the x-intercept with increasing concentration of paclitaxel.

Determination of the Effect of 3,5-Bis(styryl)pyrazoles 2a and 2l on *spn*FtsZ. 3,5-Bis(styryl)pyrazoles, **2a** and **2l**, inhibited neither the polymerization of *spn*FtsZ (a bacterial homolog of tubulin) nor the enzymatic activity of alkaline phosphatase (Fig. 14) suggesting that the compounds are not Pan-assay interference compounds.
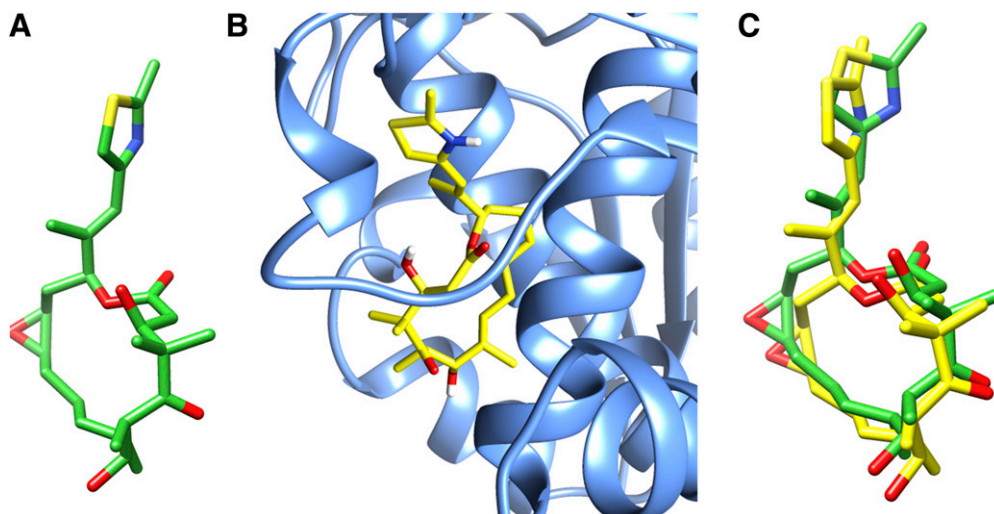

Fig. 11. Docking of epothilone with tubulin. (A) Crystal structure of epothilone (green sticks). (B) Docked conformation of epothilone (yellow sticks) with beta-tubulin (blue ribbon). (C) Root mean square deviation of the crystal structure (green) and docked conformation (yellow) of epothilone.
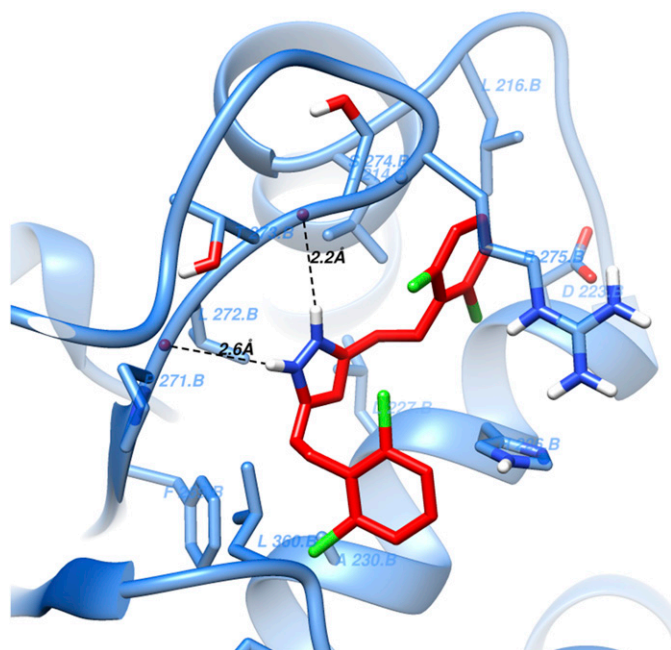
Fig. 12. Residues within 4 Å of **2l** (red sticks) on beta-tubulin (blue ribbon) showing two possible hydrogen bonds.

Discussion

A range of 3,5-bis(styryl)pyrazole analogs **2a-l** have been prepared using a very simple environmentally friendly microwave-assisted protocol, allowing the rapid and clean generation of analogs in minutes without the need for multiple chromatographic steps for purification. All analogs were screened for antiproliferative activity in the PC3 (androgen-independent) prostate cancer cell line, and two analogs (**2a** and **2l**) with GI_{50} values in the low micromolar range were selected for further biologic evaluation. 3,5-Bis(styryl)pyra-zole **2a** was the most potent compound in the study of the antiproliferative activity in PC3 cells (GI_{50} 0.85 ± 0.34 μM), whereas the novel analog **2l** was also selected for further biologic evaluation (Supplemental Fig. 1); it has been shown in other studies that analog **2a** has GI_{50} values of 5.6 μM (in PC3 cells) (Fuchs et al., 2009) and 4.19 and 0.25 μM in breast cancer cell lines, MCF-7 and SKBR3, respectively (Amolins et al., 2009). The GI_{50} of **2a** and **2l** against human cervical cancer (HeLa) cells was determined to be 2.6 ± 1.2 and 2.4 ± 0.5 μM, respectively (Supplemental Fig. 9).

In a stability study, we found that after 72 hours only 10% of derivative **2a** remained, in comparison with the 71% of analog **2l** that remained. The instability of **2a** at pH 7.4 may be due to the presence of the *para*-hydroxy group; a detailed study of the mechanism of degradation of **1a** under physiologic conditions suggested that the major degradation pathway is auto-oxidation
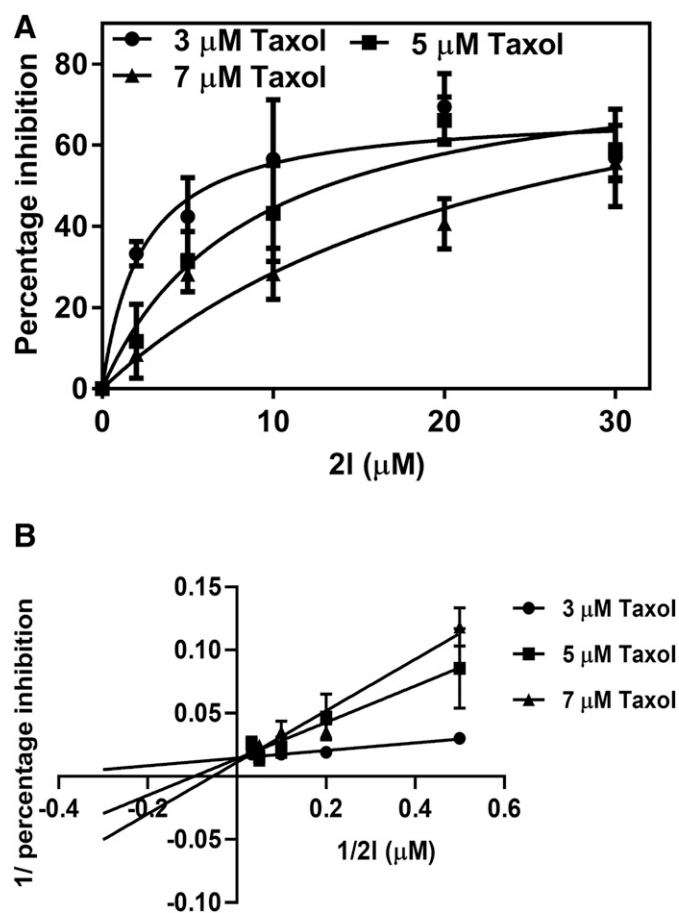
Fig. 13. Determination of the nature of inhibition of **2l** by paclitaxel. (A) Percentage inhibition data fitted in Michaelis-Menten equation. (B) Lineweaver-Burk plot for 3 (●), 5 (■), and 7 (▲) μM paclitaxel concentration showing that the nature of inhibition is competitive. The experiment was repeated three times, and error bars represent S.D.

due to the presence of this group (Gordon et al., 2015). As **2a** is a derivative of **1a**, it too could undergo similar auto-oxidation, leading to rapid degradation. Although the GI_{50} of **2a** is less than that of **2l**, **2l** might thus be a better lead than **2a**. Neither of these analogs induced apoptosis at their GI_{50} concentration, but, as can be seen from the cell cycle histograms in Fig. 4, both caused significant effects on the cell cycle, with the vast majority of treated cells in the G_2/M phase (89.6% and 89.3%, respectively), suggesting that these analogs inhibit PC3 cell growth as a result of G_2/M arrest. With no cell division, as a result of G_2/M arrest, the percentage of cells in the G_0/G_1 phase decreases, and this, in turn, reduces the number of cells in the S phase.

We next examined whether cell death results from mitotic arrest in PC3 cells. The results showed that the tested compounds caused greater cell death in PC3 cells than the

TABLE 5

Residues within 4 Å of the binding pocket of **2l**, epothilone, and paclitaxel

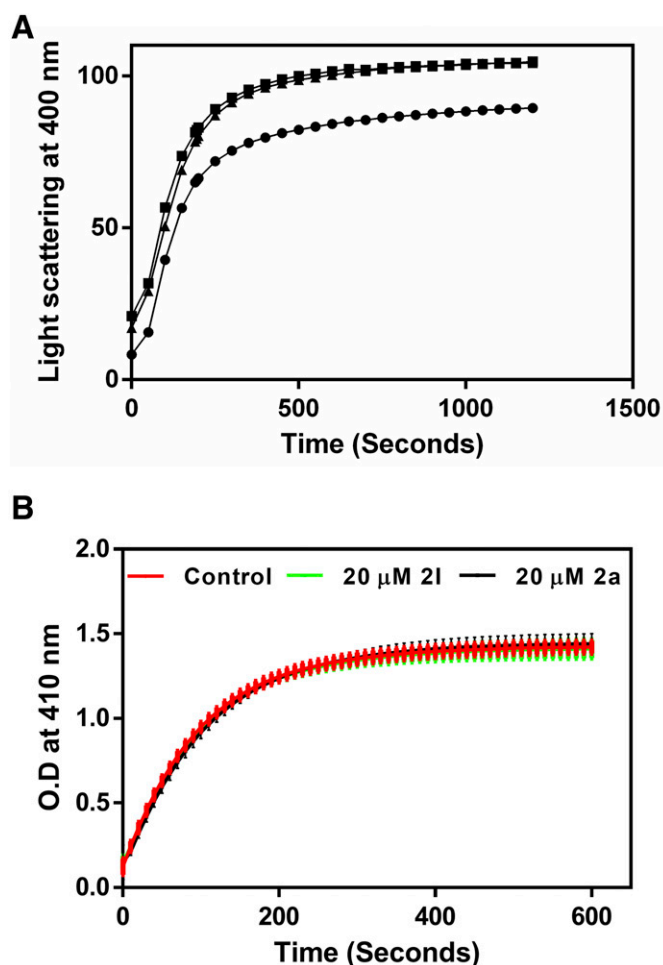| Molecule	Common residues	Uncommon residues
Epothilone	β-tubulin residues D223, H226, L227, A230, F269, P271, T273, L360,	β-tubulin residues L214, L272, S274, R275, R281, L283, Y280, Q278, Q279, G276
2l		β-tubulin residues L214, L216, L272, S274, R275, P357, **R358**
Paclitaxel		V22, D25, S233, **R358**, Q278

Fig. 14. The specificity of **2a** and **2l**. (A) Polymerization of *spn*FtsZ in the absence (●) and presence of 20 μM **2a** (▲) and **2l** (■). (B) Activity of alkaline phosphatase in the presence and absence of 20 μM of **2a** and **2l**.

FtsZ, a bacterial homolog of tubulin that shows the specific binding of **2l** to tubulin only. Treatment with both pyrazoles **2a** and **2l** caused depolymerization of the microtubules in PC3 and HeLa cells. We also found that, although **2l** depolymerizes microtubules, it shares its binding site on tubulin with paclitaxel. Paclitaxel is a known microtubule polymerizing agent, and paclitaxel site binders generally stabilize microtubules; however, few tubulin-binding small molecules, such as estramustine (Laing et al., 1997) and griseofulvin (Rathinasamy et al., 2010), are reported to share their binding sites with paclitaxel but to destabilize microtubules. In summary, we have identified a potential lead that could be the basis for future optimization in the search for novel agents for the treatment of CRPC. Both pyrazoles exert similar effects on HeLa cells (Supplemental Fig. 9), GI$_{50}$s of 2.6 ± 1.2 μM (**2a**) and 2.4 ± 0.5 μM (**2l**), through their interactions with tubulin and the depolymerization of microtubules in cells.

Authorship Contributions

Participated in research design: Liao, Kumari, Narlawar, Vignarajan, Hibbs, Panda, Groundwater.

Conducted experiments: Liao, Kumari, Narlawar.

Contributed new reagents or tools: Liao, Kumari, Narlawar.

Performed data analysis: Liao, Kumari, Vignarajan, Hibbs, Panda, Groundwater.

Wrote or contributed to the writing of the manuscript: Liao, Kumari, Hibbs, Panda, Groundwater.

References

Abouelfadel Z and Crawford ED (2008) Leuprorelin depot injection: patient considerations in the management of prostate cancer. *Ther Clin Risk Manag* 4:513–526.
Amolins MW, Peterson LB, and Blagg BSJ (2009) Synthesis and evaluation of electron-rich curcumin analogues. *Bioorg Med Chem* 17:360–367.
Bhattacharyya B, Kapoor S, and Panda D (2010) Fluorescence spectroscopic methods to analyze drug-tubulin interactions, in *Microtubules, in Vitro: Microtubules, in Vitro* (Wilson L and Correia JJ eds) pp 301–329, Elsevier Academic Press Inc, San Diego, CA.
Crawford ED, Eisenberger MA, McLeod DG, Spaulding JT, Benson R, Dorr FA, Blumenstein BA, Davis MA, and Goodman PJ (1989) A controlled trial of leuprolide with and without flutamide in prostatic carcinoma. *N Engl J Med* 321:419–424.
DeLano WL (2002) *The PyMOL Molecular Graphics System, Version 1.1*, Schrödinger LLC, New York, NY
Derenne A, Gasper R, and Goormaghtigh E (2010) Monitoring of metabolism perturbation in prostate PC-3 cancer cells by sub-lethal concentrations of methotrexate. *J Spectrosc* 24:55–60.
Dhaked HPS, Ray S, Battaje RR, Banerjee A, and Panda D (2019) Regulation of Streptococcus pneumoniae FtsZ assembly by divalent cations: paradoxical effects of Ca2+ on the nucleation and bundling of FtsZ polymers. *FEBS J* 286:3629–3646.
Feldman BJ and Feldman D (2001) The development of androgen-independent prostate cancer. *Nat Rev Cancer* 1:34–45.
Fuchs JR, Pandit B, Bhasin D, Etter JP, Regan N, Abdelhamid D, Li C, Lin J, and Li P-K (2009) Structure-activity relationship studies of curcumin analogues. *Bioorg Med Chem Lett* 19:2065–2069.
Garnick MB (1997) Hormonal therapy in the management of prostate cancer: from Huggins to the present. *Urology* 49(3A Suppl):5–15.
Gordon ON, Luis PB, Sintim HO, and Schneider C (2015) Unraveling curcumin degradation: autoxidation proceeds through spiroepoxide and vinylether intermediates en route to the main bicyclopentadione. *J Biol Chem* 290:4817–4828.
Groundwater PW, Narlawar R, Liao VWY, Bhattacharya A, Srivastava S, Kunal K, Doddareddy M, Oza PM, Mamidi R, Marrs ECL, et al. (2017) A carbocyclic curcumin inhibits proliferation of gram-positive bacteria by targeting FtsZ. *Biochemistry* 56:514–524.
Hire RR, Srivastava S, Davis MB, Kumar Konreddy A, and Panda D (2017) Antiproliferative activity of crocin involves targeting of microtubules in breast cancer cells. *Sci Rep* 7:44984.

control (Table 3, Table 4; Supplemental Fig. 5). Analog **2a** had the least effect on PC3 cells 72 hours after removal, despite showing G$_2$/M arrest in the cell cycle analysis, indicating that cells treated with this analog may either have divided or remained in a senescing state. Treatment with analog **2l** led to the greatest total percentage of dead PC3 cells. Analysis of the cell cycle in cells treated with analog **2l** showed that this compound resulted in the greatest percentage of cells in the G$_2$/M phase, indicating that the arrested cells undergo significant mitotic death.

There are three possible main outcomes from drug-mediated mitotic arrest upon drug removal (Yamada and Gorbsky, 2006): the cells divide (they may recover, leading to normal cell division or divide with abnormalities in the genome); the cells may remain in a senescent state, in which they are metabolically active but do not undergo further cell division; or cell death may be triggered, either by necrosis or apoptosis.

3,5-Bis(styryl)pyrazole **2l** inhibited the polymerization of purified tubulin (Fig. 5), inhibiting both the rate and extent of tubulin assembly, as monitored by light scattering and sedimentation assay. Extensive testing of the effects of these pyrazoles on tubulin and microtubules showed that **2l** binds to tubulin tightly with a K$_d$ of 0.4 ± 0.1 μM and inhibits the assembly of purified tubulin with no effect on the assembly of

Hura N, Naaz A, Prassanawar SS, Guchhait SK, and Panda D (2018) Drug-clinical agent molecular hybrid: synthesis of diaryl(trifluoromethyl)pyrazoles as tubulin targeting anticancer agents. *ACS Omega* **3**:1955–1969.

Jaghoori MM, Bleijlevens B, and Olabarriaga SD (2016) 1001 ways to run AutoDock Vina for virtual screening. *J Comput Aided Mol Design* **30**:237–249.

Jayaprakasha GK, Jagan Mohan Rao L, and Sakariah KK (2002) Improved HPLC method for the determination of curcumin, demethoxycurcumin, and bisdemethoxycurcumin. *J Agric Food Chem* **50**:3668–3672.

Karantanos T, Corn PG, and Thompson TC (2013) Prostate cancer progression after androgen deprivation therapy: mechanisms of castrate resistance and novel therapeutic approaches. *Oncogene* **32**:5501–5511.

Laing N, Dahllöf B, Hartley-Asp B, Ranganathan S, and Tew KD (1997) Interaction of Estramustine with Tubulin Isotypes. *Biochemistry* **36**:871–878.

Lin W and Chen T (2013) A vinblastine fluorescent probe for pregnane X receptor in a time-resolved fluorescence resonance energy transfer assay. *Anal Biochem* **443**:252–260.

Luo JX, Ding W, Zhang YQ, Yang ZG, Li Y, and Ding LJ (2013) Semisynthesis and acaricidal activities of isoxazole and pyrazole derivatives of a natural product bisdemethoxycurcumin. *J Pestic Sci* **38**:214–219.

Marques SM, Enyedy ÉA, Supuran CT, Krupenko NI, Krupenko SA, and Santos MA (2010) Pteridine-sulfonamide conjugates as dual inhibitors of carbonic anhydrases and dihydrofolate reductase with potential antitumor activity. *Bioorg Med Chem* **18**:5081–5089.

Mayadevi M, Sherin DR, Keerthi VS, Rajasekharan KN, and Omkumar RV (2012) Curcumin is an inhibitor of calcium/calmodulin dependent protein kinase II. *Bioorg Med Chem* **20**:6040–6047.

Mosmann T (1983) Rapid colorimetric assay for cellular growth and survival: application to proliferation and cytotoxicity assays. *J Immunol Methods* **65**:55–63.

Mukhtar E, Adhami VM, and Mukhtar H (2014) Targeting microtubules by natural agents for cancer therapy. *Mol Cancer Ther* **13**:275–284.

Panda D, Rathinasamy K, Santra MK, and Wilson L (2005) Kinetic suppression of microtubule dynamic instability by griseofulvin: implications for its possible use in the treatment of cancer. *Proc Natl Acad Sci USA* **102**:9878–9883.

Pettersen EF, Goddard TD, Huang CC, Couch GS, Greenblatt DM, Meng EC, and Ferrin TE (2004) UCSF Chimera--a visualization system for exploratory research and analysis. *J Comput Chem* **25**:1605–1612.

Pulukuri SM, Gondi CS, Lakka SS, Jutla A, Estes N, Gujrati M, and Rao JS (2005) RNA interference-directed knockdown of urokinase plasminogen activator and urokinase plasminogen activator receptor inhibits prostate cancer cell invasion, survival, and tumorigenicity in vivo. *J Biol Chem* **280**:36529–36540.

Ranade AR, Higgins L, Markowski TW, Glaser N, Kashin D, Bai R, Hong KH, Hamel E, Höfle G, and Georg GI (2016) Characterizing the epothilone binding site on β-tubulin by photoaffinity labeling: identification of β-tubulin peptides TARGSQQY and TSRGSQQY as targets of an epothilone photoprobe for polymerized tubulin. *J Med Chem* **59**:3499–3514.

Rane JS, Bhaumik P, and Panda D (2017) Curcumin inhibits tau aggregation and disintegrates preformed tau filaments *in vitro*. *J Alzheimers Dis* **60**:999–1014.

Rathinasamy K, Jindal B, Asthana J, Singh P, Balaji PV, and Panda D (2010) Griseofulvin stabilizes microtubule dynamics, activates p53 and inhibits the proliferation of MCF-7 cells synergistically with vinblastine. *BMC Cancer* **10**:213, doi: 10.1186/1471-2407-10-213.

Sawant AV, Srivastava S, Prassanawar SS, Bhattacharyya B, and Panda D (2019) Crocin, a carotenoid, suppresses spindle microtubule dynamics and activates the mitotic checkpoint by binding to tubulin. *Biochem Pharmacol* **163**:32–45.

Schmitt J, Noble A, Otsuka M, Berry P, Maitland NJ, and Rumsby MG (2014) Phorbol ester stimulates ethanolamine release from the metastatic basal prostate cancer cell line PC3 but not from prostate epithelial cell lines LNCaP and P4E6. *Br J Cancer* **111**:1646–1656.

Schüttelkopf AW and van Aalten DM (2004) PRODRG: a tool for high-throughput crystallography of protein-ligand complexes. *Acta Crystallogr D Biol Crystallogr* **60**:1355–1363.

Serova M, Bieche I, Sablin MP, Pronk GJ, Vidaud M, Cvitkovic E, Faivre S, and Raymond E (2011) Single agent and combination studies of pralatrexate and molecular correlates of sensitivity. *Br J Cancer* **104**:272–280.

Snyder JP, Nettles JH, Cornett B, Downing KH, and Nogales E (2001) The binding conformation of Taxol in β-tubulin: a model based on electron crystallographic density. *Proc Natl Acad Sci USA* **98**:5312–5316.

Taplin ME and Balk SP (2004) Androgen receptor: a key molecule in the progression of prostate cancer to hormone independence. *J Cell Biochem* **91**:483–490.

Todd A, Groundwater PW, and Gill JH (2018) *Anticancer Therapeutics: From Drug Discovery to Clinical Applications*, John Wiley & Sons Ltd., Chichester, UK.

Tønnesen HH and Karlsen J (1985) Studies on curcumin and curcuminoids. VI. Kinetics of curcumin degradation in aqueous solution. *Z Lebensm Unters Forsch* **180**:402–404.

Torne SJ, Ansari KA, Vavia PR, Trotta F, and Cavalli R (2010) Enhanced oral paclitaxel bioavailability afteradministration of paclitaxel-loaded nanosponges. *Drug Delivery* **17**:419–425, doi: 10.3109/10717541003777233.

Trott O and Olson AJ (2010) AutoDock Vina: improving the speed and accuracy of docking with a new scoring function, efficient optimization, and multithreading. *J Comput Chem* **31**:455–461.

Vichai V and Kirtikara K (2006) Sulforhodamine B colorimetric assay for cytotoxicity screening. *Nat Protoc* **1**:1112–1116.

Yadava U, Gupta H, and Roychoudhury M (2015) Stabilization of microtubules by taxane diterpenoids: insight from docking and MD simulations. *J Biol Phys* **41**:117–133.

Yamada HY and Gorbsky GJ (2006) Spindle checkpoint function and cellular sensitivity to antimitotic drugs. *Mol Cancer Ther* **5**:2963–2969.

Address correspondence to: Paul W. Groundwater, Sydney Pharmacy School, Faculty of Medicine and Health, The University of Sydney, Sydney, NSW 2006, Australia. E-mail: paul.groundwater@sydney.edu.au; or Dulal Panda, Department of Biosciences and Bioengineering, Indian Institute of Technology Bombay, Mumbai 400076, India. E-mail: panda@iitb.ac.in

Tubulin-Binding 3,5-Bis(styryl)pyrazoles as Lead Compounds for the Treatment of Castration-Resistant Prostate Cancer

Vivian W.Y. Liao,[#] Anuradha Kumari,[#] Rajeshwar Narlawar, Soma Vignarajan, David E. Hibbs, Dulal Panda, and Paul W. Groundwater

Sydney Pharmacy School, Faculty of Medicine and Health, The University of Sydney, Sydney, NSW 2006, Australia (VWYL, RN, DEH, PWG); Department of Biosciences and Bioengineering, Indian Institute of Technology Bombay, Mumbai 400076, India (AK, DP); Charles Perkins Centre, The University of Sydney, Sydney, NSW 2006, Australia (SV)

[#] These authors contributed equally to this work.

SUPPLEMENTARY INFORMATION

General Synthetic Methods

The 3,5-bis(styryl)pyrazoles **2a-l** were synthesized from the curcuminoids **1** using a CEM Discover SP microwave synthesis system. The spectroscopic and analytical data for pyrazoles **2a** [28,34], **2b** [28] and **2k** [35] were identical to that reported previously. Melting points were determined on a Stuart Scientific SMP10 apparatus. IR spectra were obtained on a FTIR-8400S Shimadzu system, using NaCl plates and values are recorded as wave-numbers (cm^{-1}). ^{1}H and ^{13}C NMR spectra were recorded at 400 and 100 MHz, respectively, on a Varian 400-MR magnetic resonance spectrometer, with chemical shifts (δ) reported in parts per million (ppm). Spectra were acquired in solutions of deuterated solvents and the residual solvent peaks were used as internal references; 7.24 ppm (CDCl$_3$), 2.50 ppm (DMSO-d_6), 2.05 ppm (acetone-d_6) and 3.31 ppm (methanol-d_4). Low resolution electrospray ionization (ESI) mass spectrometry was performed on a TSQ Quantum Access Max LCMS/MS (Thomas R Watson Mass Spectrometry Laboratory, Faculty of Pharmacy, The University of Sydney) and high resolution mass spectroscopy was performed on a Bruker 7T Fourier transform ion cyclotron resonance mass spectrometer (Mass Spectrometry Unit, School of Chemistry, The University of Sydney). Elemental analysis was performed on a Thermo Flash 2000 Elemental Analyser (Campbell Microanalytical Laboratory, University of Otago, New Zealand). All reagents were commercially available and purchased from Sigma Aldrich (Castle Hill, Sydney, Australia), Alfa Aesar (VWR, Australia). Solvents were purchased from Chem-Supply (Australia) and were used as received. Flash column chromatography was performed using Grace Davison (LC604 40-63 µm) Davisil chromatographic silica media. Thin layer chromatography (TLC) was performed using Grace Davidson Reveleris, aluminium-backed TLC plates (UV254).

3,5-Bis[(1E)-2-(3-ethoxy-4-hydroxyphenyl)ethenyl]-1H-pyrazole (2c). Yield 57 %, pale yellow crystalline solid, mp 149-153 ˚C. ^{1}H NMR (400 MHz, acetone-d_6) δ 7.19 (2H, d, J = 2.0 Hz, 2 × H-2″), 7.11 (2H, d, J = 16.8 Hz, 2 × H-2′), 7.00-6.96 (4H, m, 2 × H-1′, 2 × H-6″), 6.83 (2H, d, J = 8.0 Hz, 2 × H-5″), 6.65 (1H, s, H-4), 4.17 (4H, q, J = 6.8 Hz, 2 × OCH$_2$CH$_3$), 1.40 (6H, t, J = 6.8 Hz, 2 × OCH$_2$CH$_3$). ^{13}C NMR (100 MHz, acetone-d_6) δ 148.9 (2 × quat, 2 × C-4″), 148.8 (2 × quat, 2 × C-3″), 131.6 (2 × quat, 2 × C-1″), 131.1 (2 × CH, 2 × C-2′), 122.1 (2 × CH, 2 × C-6″), 116.9 (2 × CH, 2 × C-5″), 111.8 (2 × CH, 2 × C-2″), 100.9 (CH, C-4), 66.0 (2 × OCH$_2$CH$_3$), 16.1 (2 × OCH$_2$CH$_3$). IR (cm^{-1}) v_{max} 3535 (OH), 3316 (NH), 1593 (C=N), 1558 (C=C), 1511 (C=C). ESI-MS: *m/z* 393 (100 %) [M+H]$^+$. Anal. Calcd for C$_{23}$H$_{24}$N$_2$O$_4$: C, 70.39; H, 6.16; N, 7.14. Found: C, 70.19; H, 6.43; N, 6.92.

3,5-Bis[(1E)-2-(3-hydroxy-4-methoxyphenyl)ethenyl]-1H-pyrazole (2d). Yield 35 %, pale yellow crystalline solid, mp 246-253 ˚C. ^{1}H NMR (400 MHz, acetone-d_6) δ 7.09 (2H, d, J = 2.0 Hz, 2 × H-2″), 7.10 (2H, d, J = 16.4 Hz, 2 × H-2′), 7.00-6.93 (6H, m, 2 × H-1′, 2 × H-5″, 2 × H-6″), 6.69 (1H, s, H-4), 3.86 (6H, s, 2 × OCH$_3$). ^{13}C NMR (100 MHz, acetone-d_6) δ 149.5 (2 × quat, 2 × C-3″), 148.7 (2 × quat, 2 × C-4″), 132.4 (2 × quat, 2 × C-1″), 131.3 (2 × CH, 2 × C-2′), 120.5 (2 × CH, 2 × C-6″), 114.1 (2 × CH, 2 × C-2″), 113.4 (2 × CH, 2 × C-5″), 101.2 (CH, C-4), 57.3 (2 × OCH$_3$). IR (cm^{-1}) v_{max} 3290 (OH), 3229 (NH), 1582 (C=N), 1564 (C=C), 1511 (C=C). ESI-MS: *m/z* 365 (100 %) [M+H]$^+$. Anal. Calcd for C$_{21}$H$_{20}$N$_2$O$_4$ · 0.5 CH$_3$OH: C, 67.82; H, 5.83; N, 7.36. Found: C, 67.62; H, 5.74; N, 7.52.

3,5-Bis[(1E)-2-(4-ethoxy-3-methoxyphenyl)ethenyl]-1H-pyrazole (2e). Yield 51 %, white crystalline solid, mp 191-193 ˚C. ^{1}H NMR (400 MHz, CDCl$_3$) δ 7.06-7.02 (4H, m, 2 × H-2′, 2 × H-2″), 6.98 (2H, dd, J = 8.0, 1.6 Hz, 2 × H-6″), 6.93 (2H, d, J = 16.4 Hz, 2 × H-1′), 6.80 (2H, d, J = 8.4 Hz, 2 × H-5″), 6.60 (1H, s, H-4), 4.10 (4H, q, J = 6.8 Hz, 2 × OCH$_2$CH$_3$), 3.87 (6H, s, 2 ×

OCH₃), 1.47 (6H, t, $J = 6.8$ Hz, 2 × OCH$_2$CH$_3$). ^{13}C NMR (100 MHz, CDCl$_3$) δ 149.3 (2 × quat, 2 × C-4″), 148.5 (2 × quat, 2 × C-3″), 130.6 (2 × CH, 2 × C-2′), 129.5 (2 × quat, 2 × C-1″), 120.0 (2 × CH, 2 × C-6″), 112.4 (2 × CH, 2 × C-5″), 108.8 (2 × CH, 2 × C-2″), 99.5 (CH, C-4), 64.3 (2 × OCH$_2$CH$_3$), 55.8 (2 × OCH$_3$), 14.8 (2 × OCH$_2$CH$_3$). IR (cm^{-1}) υ_{max} 3396 (NH), 1595 (C=N), 1577 (C=C), 1507 (C=C). ESI-MS: m/z 421 (100 %) [M+H]$^+$. Anal. Calcd for C$_{25}$H$_{28}$N$_2$O$_4$: C, 71.41; H, 6.71; N, 6.66. Found: C, 71.33; H, 6.77; N, 6.66.

3,5-Bis[(1E)-2-(4-methylphenyl)ethenyl]-1H-pyrazole (2f). Yield 28 %, yellow crystalline solid, mp 191-193 ˚C. ^{1}H NMR (400 MHz, acetone-d_6) δ 12.18 (1H, bs, H-1), 7.45 (4H, d, $J = 8.0$ Hz, 2 × H-2″, 2 × H-6″), 7.20-7.17 (6H, m, 2 × H-2′, 2 × H-3″, 2 × H-5″), 7.10 (2H, d, $J = 16.8$ Hz, 2 × H-1′), 6.75 (1H, s, H-4), 2.33 (6H, s, 2 × CH$_3$). ^{13}C NMR (100 MHz, acetone-d_6) δ 139.3 (2 × quat, 2 × C-4″), 136.3 (2 × quat, 2 × C-1″), 131.2 (6 × CH, 2 × C-2′, 2 × C-3″, 2 × C-5″), 128.1 (4 × CH, 2 × C-2″, 2 × C-6″), 101.7 (CH, C-4), 22.2 (2 × CH$_3$). IR (cm^{-1}) υ_{max} 3209 (NH), 1583 (C=N), 1558 (C=C), 1506 (C=C). m/z 301 (100 %) [M+H]$^+$. Anal. Calcd for C$_{21}$H$_{20}$N$_2$: C, 83.96; H, 6.71; N, 9.33. Found: C, 84.08; H, 6.78; N, 9.50.

3,5-Bis[(1E)-2-(2-methoxyphenyl)ethenyl]-1H-pyrazole (2g). Yield 50 %, waxy white solid, mp 92-95 ˚C. ^{1}H NMR (400 MHz, acetone-d_6) δ 7.61 (2H, dd, $J = 8.0, 1.6$ Hz, 2 × H-6″), 7.49 (2H, d, $J = 16.8$ Hz, 2 × H-2′), 7.29-7.24 (2H, m, 2 × H-4″), 7.19 (2H, d, $J = 16.8$ Hz, 2 × H-1′), 7.03 (2H, d, $J = 8.0$ Hz, 2 × H-3″), 6.97 (2H, m, 2 × H-5″), 6.73(1H, s, H-4), 3.91 (6H, s, 2 × OCH$_3$). ^{13}C NMR (100 MHz, acetone-d_6) δ 159.0 (2 × quat, 2 × C-2″), 130.7 (2 × CH, 2 × C-4″), 128.3 (2 × CH, 2 × C-6″), 127.7 (2 × quat, 2 × C-1″), 126.4 (2 × CH, 2 × C-2′), 122.5 (2 × CH, 2 × C-5″), 113.0 (2 × CH, 2 × C-3″), 101.5 (CH, C-4), 56.9 (2 × OCH$_3$). IR (cm^{-1}) υ_{max} 3176 (NH), 1595 (C=N), 1576 (C=C), 1489 (C=C). ESI-MS: m/z 333 (100 %) [M+H]$^+$. HRMS (ESI): calcd for C$_{21}$H$_{21}$N$_2$O$_2$ [M + H]$^+$ 333.1603, found 333.1600.

3,5-Bis[(1E)-2-(3-methoxyphenyl)ethenyl]-1H-pyrazole (2h). Yield 41 %, white solid, mp 111-113 ˚C. ^{1}H NMR (400 MHz, CDCl$_3$) δ 7.24 (2H, t, J = 8.0 Hz, 2 × H-5″), 7.09 (2H, d, J = 16.4 Hz, 2 × H-1′), 7.07-7.02 (4H, m, 2 × H-2′, 2 × H-6″), 7.00 (2H, s, 2 × H-2″), 6.82 (2H, dd, J = 8.0, 2.0 Hz, 2 × H-4″), 6.66 (1H, s, H-4), 3.81 (6H, s, 2 × OCH$_3$). ^{13}C NMR (100 MHz, CDCl$_3$) δ 159.8 (2 × quat, 2 × C-3″), 147.1 (2 × quat, C-3, C-5), 137.9 (2 × quat, 2 × C-1″), 130.9 (2 × CH, 2 × C-2′), 129.7 (2 × CH, 2 × C-5″), 119.2 (2 × CH, 2 × H-6″), 117.9 (2 × CH, 2 × C-1′), 113.8 (2 × CH, 2 × C-4″), 111.6 (2 × CH, 2 × C-2″), 100.4 (CH, C-4), 55.2 (2 × OCH$_3$). IR (cm^{-1}) v_{max} 3183 (NH), 1597 (C=N), 1588 (C=C), 1481 (C=C). ESI-MS: *m/z* 333 (100 %) [M+H]$^+$. Anal. Calcd for C$_{21}$H$_{20}$N$_2$O$_2$: C, 75.88; H, 6.06; N, 8.43. Found: C, 75.83; H, 6.09; N, 8.56.

3,5-Bis[(1E)-2-(4-methoxyphenyl)ethenyl]-1H-pyrazole (2i). Yield 46 %, pale yellow crystalline solid, mp 184-189 ˚C. ^{1}H NMR (400 MHz, CDCl$_3$) δ 7.40(4H, d, J = 8.8 Hz, 2 × H-2″, 2 × H-6″), 7.06 (2H, d, J = 16.4 Hz, 2 × H-2′), 6.92 (2H, d, J = 16.4 Hz, 2 × H-1′), 6.85 (4H, d, J = 8.8 Hz, 2 × H-3″, 2 × H-5″), 6.60 (1H, bs, H-4), 3.82 (6H, s, 2 × OCH$_3$). ^{13}C NMR (100 MHz, CDCl$_3$) δ 159.5 (2 × quat, 2 × C-4″), 147.4 (2 × quat, C-3, C-5), 130.4 (2 × CH, 2 × C-2′), 129.3 (2 × quat, 2 × C-1″), 127.8 (4 × CH, 2 × C-2″, 2 × C-6″), 115.6 (2 × CH, 2 × C-1′), 114.1 (2 × CH, 2 × C-3″, 2 × C-5″), 99.5 (CH, C-4), 55.3 (2 × OCH$_3$). IR (cm^{-1}) v_{max} 3384 (NH), 1601 (C=N), 1569 (C=C), 1507 (C=C). ESI-MS: *m/z* 333 (100 %) [M+H]$^+$. Anal. Calcd for C$_{21}$H$_{20}$N$_2$O$_2$: C, 75.88; H, 6.06; N, 8.43. Found: C, 75.91; H, 6.11; N, 8.52.

3,5-Bis[(1E)-2-(3-hydroxyphenyl)ethenyl]-1H-pyrazole (2j). Yield 29 %, beige crystalline solid, mp 207-211 ˚C. ^{1}H NMR (400 MHz, methanol-d_4) δ 7.20-7.16 (2H, m, 2 × H-5″), 7.11 (2H, d, J = 16.4 Hz, 2 × H-2′), 7.03-6.97 (6H, m, 2 × H-1′, 2 × H-2″, 2 × H-6″), 6.73 (1H, s, H-4), 6.73-6.70 (2H, m, 2 × H-4″). ^{13}C NMR (100 MHz, methanol-d_4) δ 158.9 (2 × quat, 2 × C-3″), 139.6 (2 × quat, 2 × C-1″), 132.1 (2 × CH, 2 × C-2″), 130.8 (2 × CH, 2 × C-5″), 119.3 (2 × CH, 2 × C-6″),

116.2 (2 × CH, 2 × C-4″), 113.8 (2 × CH, 2 × C-2″), 101.0 (CH, C-4). IR (cm^{-1}) v_{max} (OH), 1595 (C=N), 1582 (C=C), 1489 (C=C). ESI-MS: *m/z* 305 (100 %) [M+H]$^{+}$. Anal. Calcd for C$_{19}$H$_{16}$N$_2$O$_2$: C, 74.98; H, 5.30; N, 9.20. Found: C, 74.72; H, 5.49; N, 9.13.

*3,5-Bis[(1*E*)-2(2,6-dichlorophenyl)ethenyl]-1H-pyrazole (2l).* Yield 18 %, white fluffy solid, mp 205-210 ˚C. ^{1}H NMR (400 MHz, CDCl$_3$) δ 7.33 (4H, d, *J* = 8.0 Hz, 2 × H-3″, 2 × H-5″), 7.22-7.17 (4H, m, 2 × C-1′, 2 × C-2′), 7.13-7.09 (2H, m, 2 × H-4″), 6.81 (1H, bs, H-4). ^{1}H NMR (400 MHz, methanol-*d$_4$*) δ 7.44 (4H, d, *J* = 8.4 Hz, 2 × H-3″, 2 × H-5″), 7.27-7.22 (4H, m, 2 × H-2′, 2 × H-4″), 7.12 (2H, d, *J* = 16.8 Hz, 2 × H-1′), 6.87 (1H, s, H-4). ^{13}C NMR (100 MHz, CDCl$_3$) δ 134.5 (2 × quat, 2 × C-2″, 2 × 6″), 133.6 (2 × quat, 2 × C-1″), 128.6 (4 × CH, 2 × C-3″, 2 × C-5″), 128.4 (2 × CH, 2 × C-4″), 126.0 (2 × CH, 2 × C-1′), 124.6 (2 × CH, 2 × C-2′), 101.2 (CH, C-4). IR (cm^{-1}) v_{max} 3169 (NH), 1653 (C=N), 1558 (C=C), 1506 (C=C). ESI-MS: *m/z* C$_{19}$H$_{13}$^{35}Cl$_4$N$_2$, 409 (71 %) [M+H]$^{+}$, C$_{19}$H$_{13}$^{35}Cl$_3$^{37}ClN$_2$, 411 (100 %) [M+H]$^{+}$, C$_{19}$H$_{13}$^{35}Cl$_2$^{37}Cl$_2$N$_2$, 413 (41 %) [M+H]$^{+}$, C$_{19}$H$_{13}$^{35}Cl^{37}Cl$_3$N$_2$, 415 (10 %) [M+H]$^{+}$. Anal. Calcd for C$_{19}$H$_{12}$Cl$_4$N$_2$: C, 55.64; H, 2.95; N, 6.83. Found: C, 55.67; H, 2.91; N, 6.78.

¹H AND ¹³C SPECTRA OF NOVEL COMPOUNDS

3,5-Bis[(1*E*)-2-(3-ethoxy-4-hydroxyphenyl)ethenyl]-1*H*-pyrazole (**2c**)

3,5-Bis[(1*E*)-2-(3-hydroxy-4-methoxyphenyl)ethenyl]-1*H*-pyrazole (**2d**)

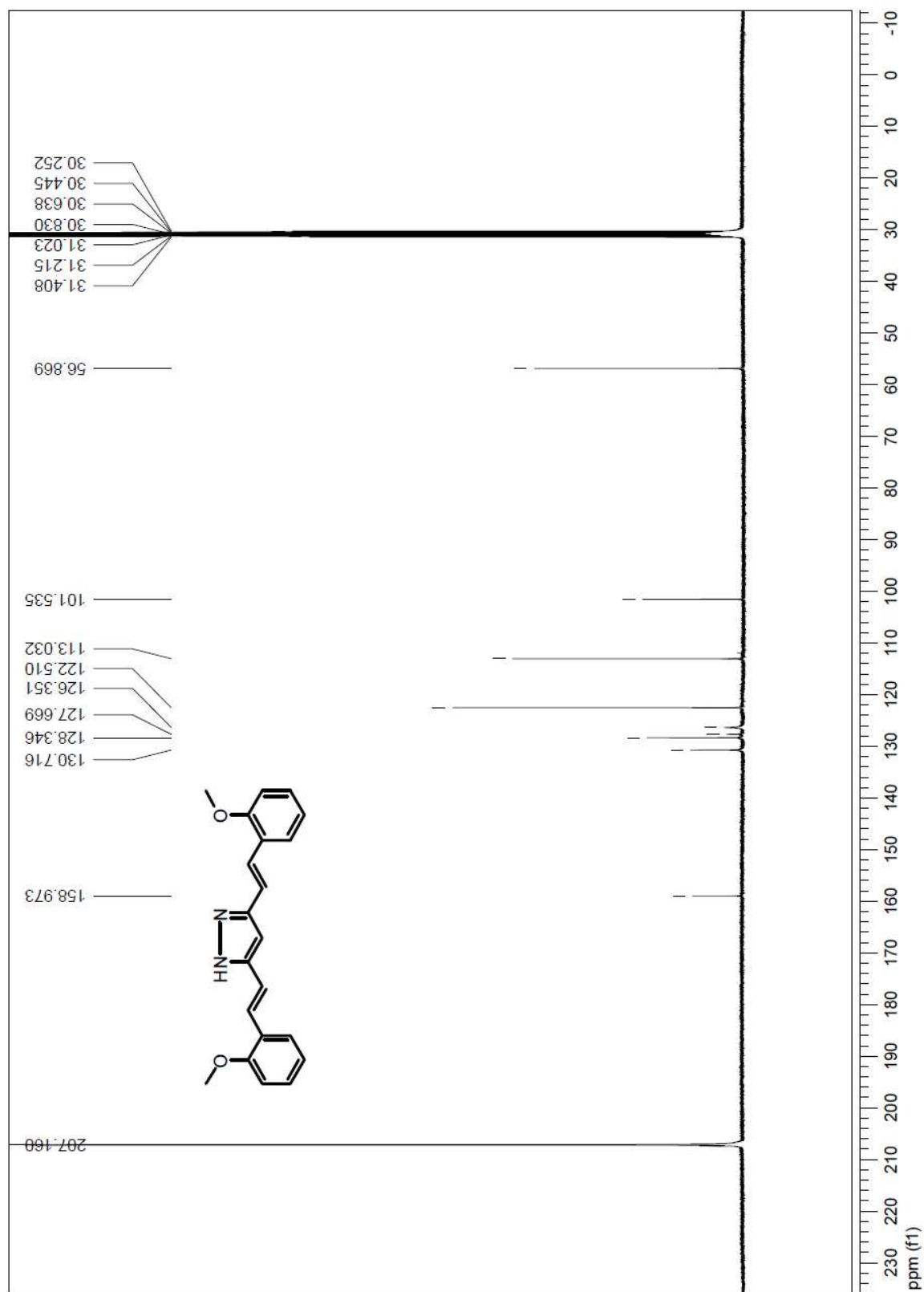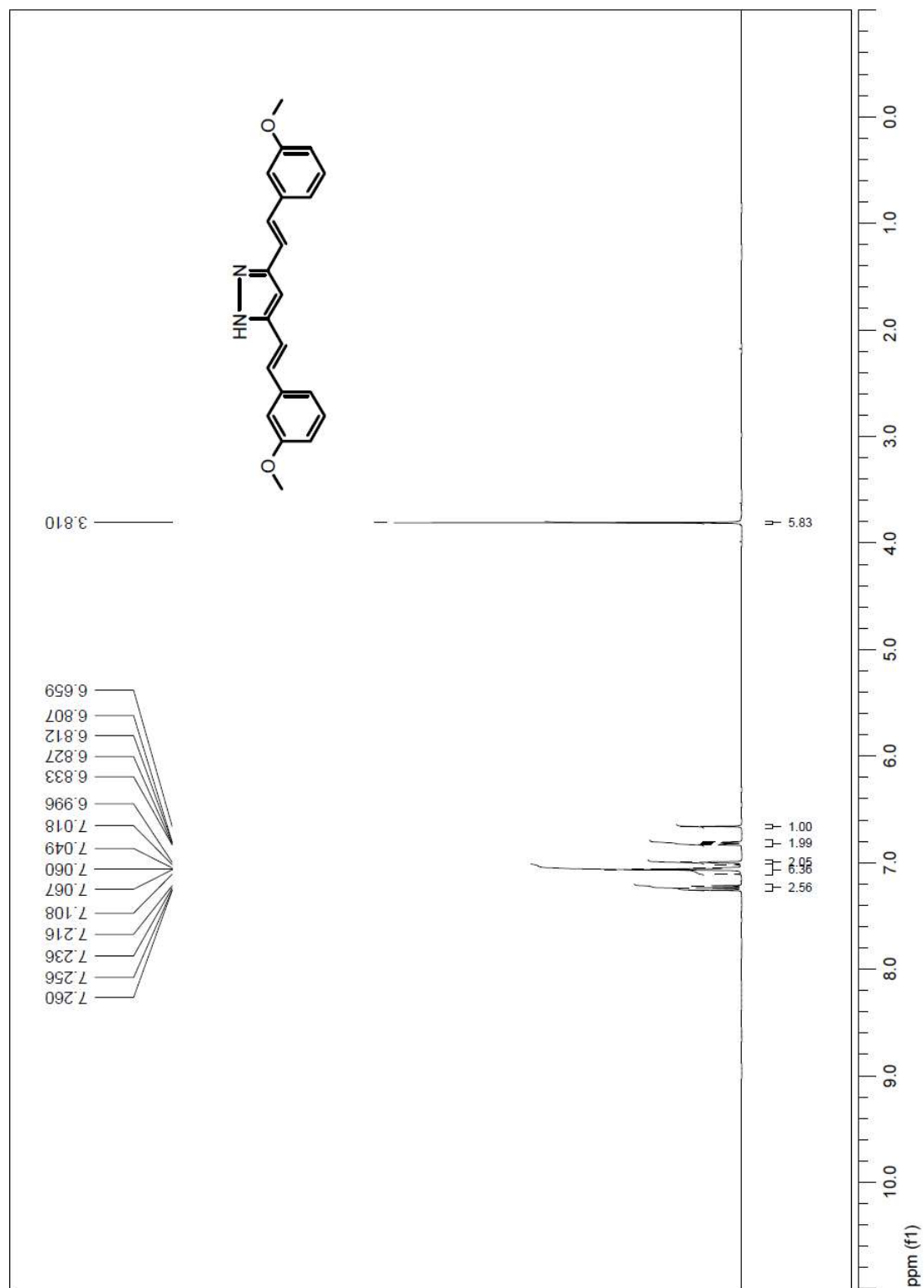3,5-Bis[(1*E*)-2-(4-ethoxy-3-methoxyphenyl)ethenyl]-1*H*-pyrazole (**2e**)

3,5-Bis[(1*E*)-2-(4-methylphenyl)ethenyl]-1*H*-pyrazole (**2f**)

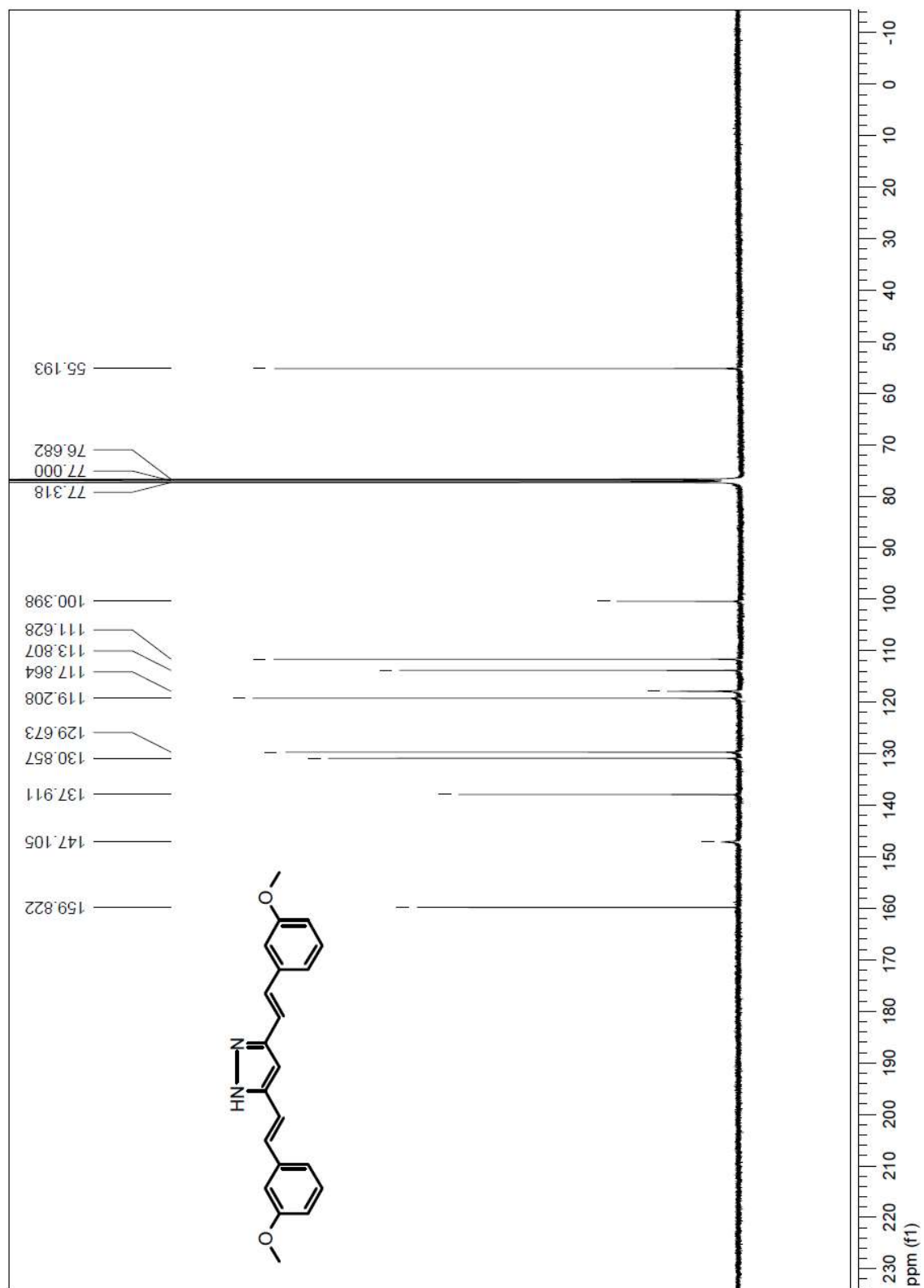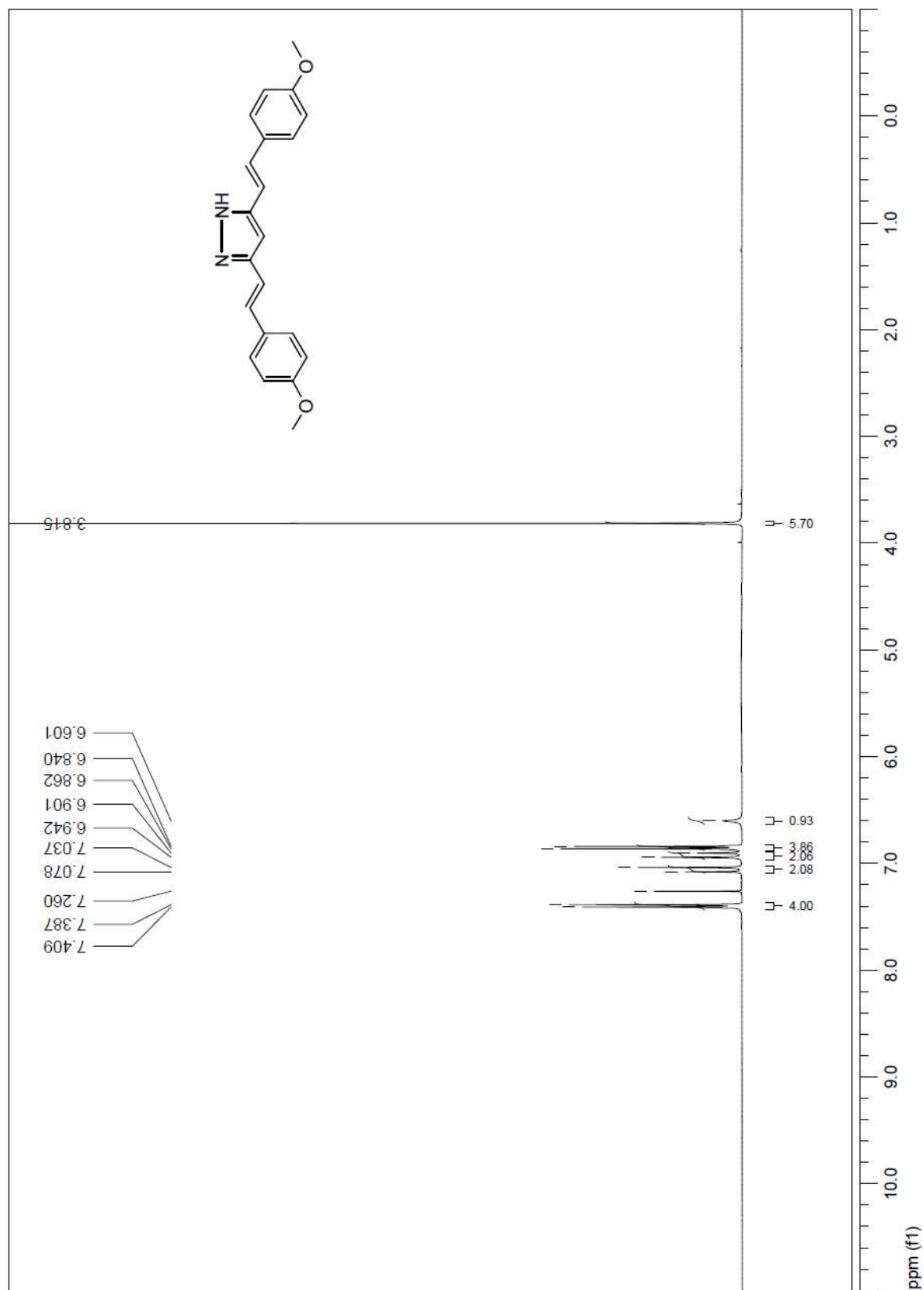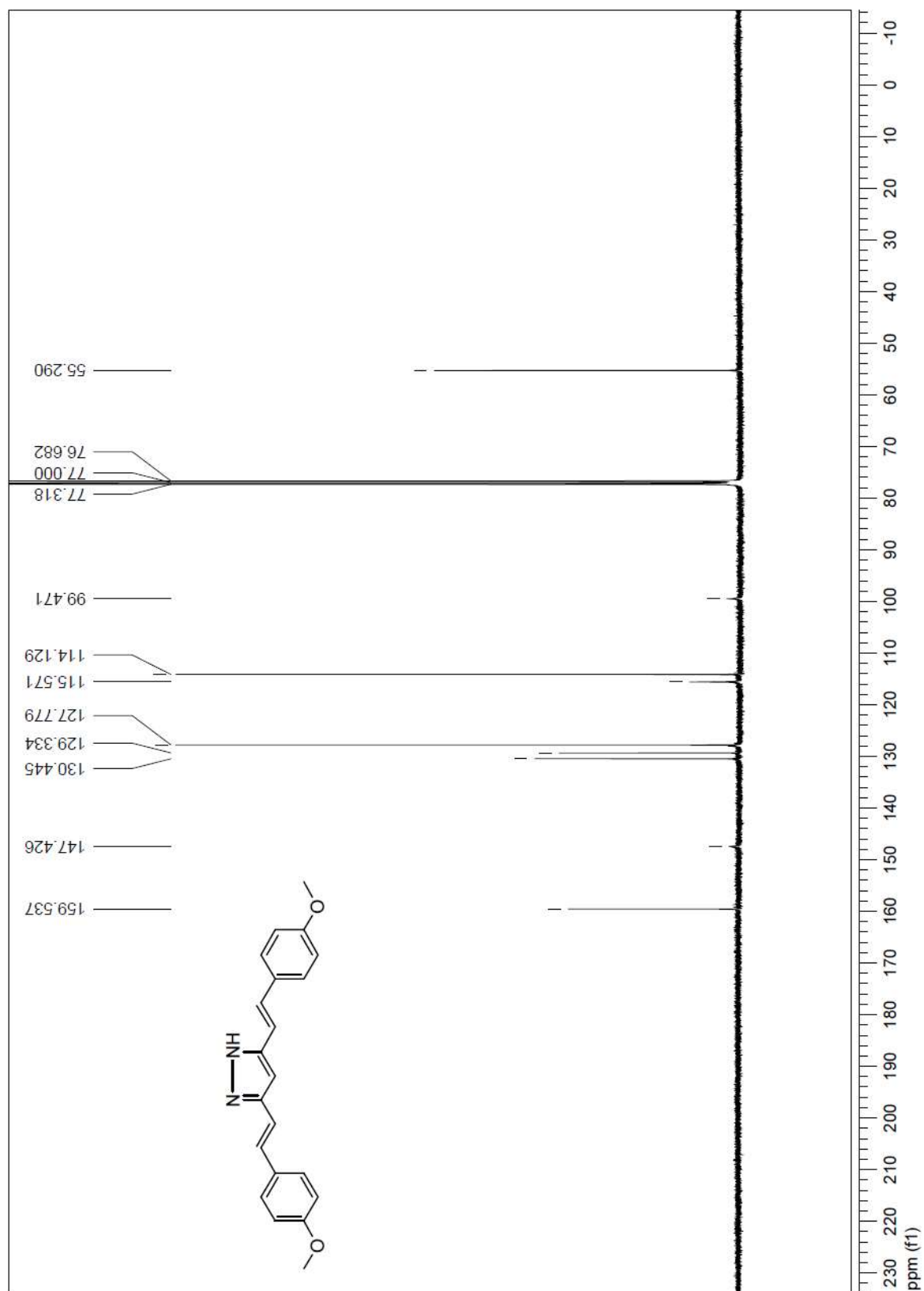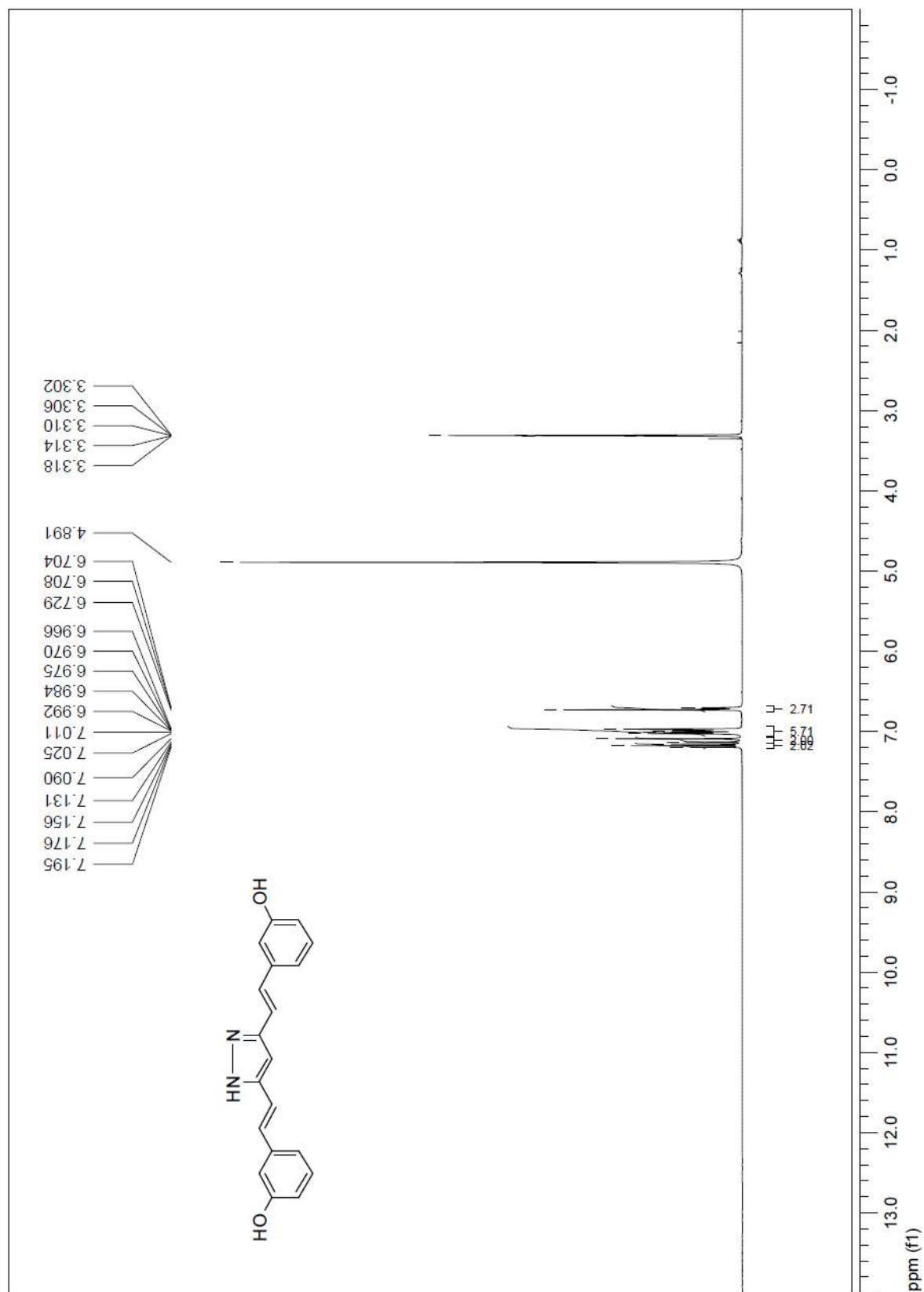3,5-Bis[(1*E*)-2-(2-methoxyphenyl)ethenyl]-1*H*-pyrazole (**2g**)

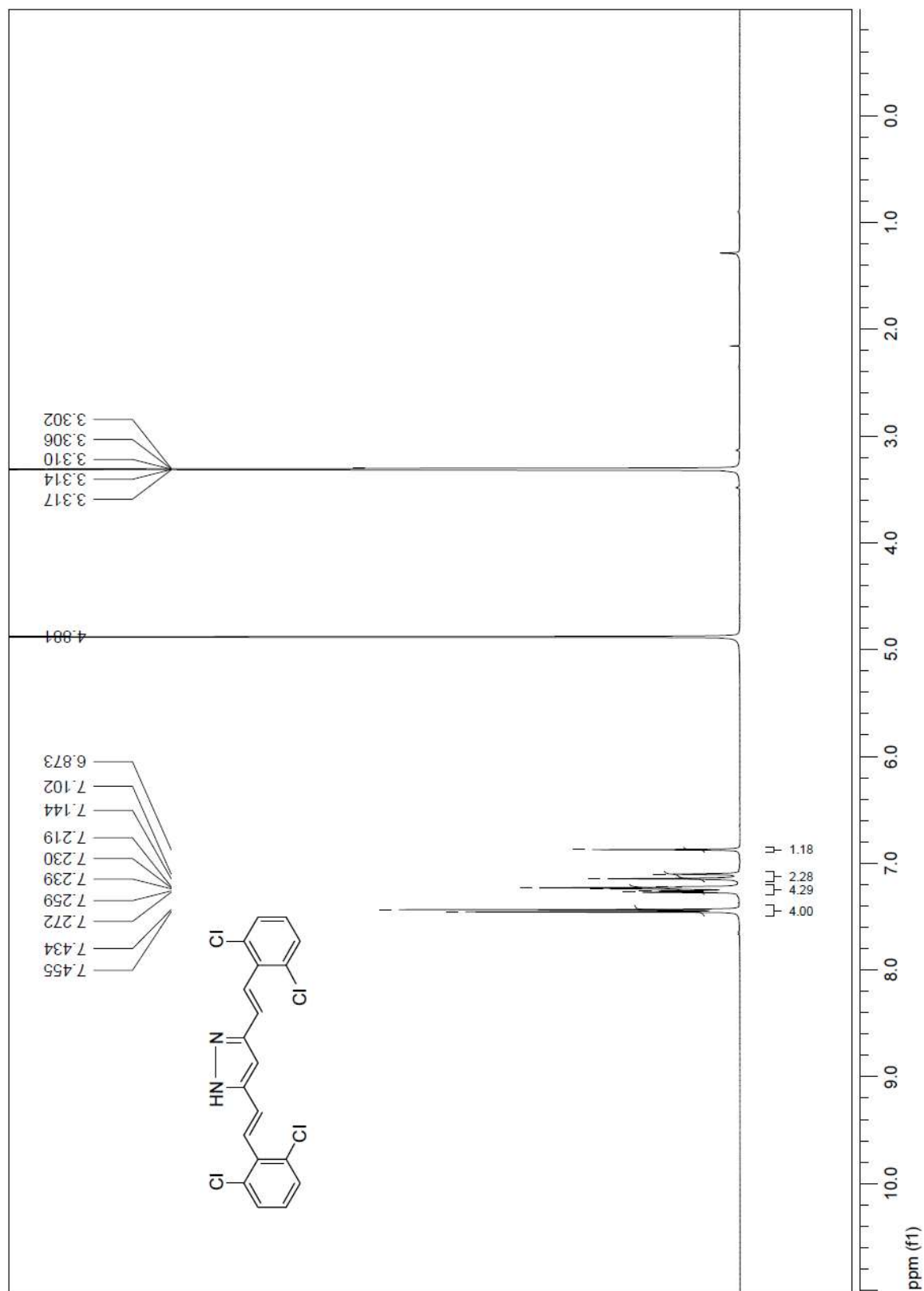3,5-Bis[(1*E*)-2-(3-methoxyphenyl)ethenyl]-1*H*-pyrazole (**2h**)

3,5-Bis[(1*E*)-2-(4-methoxyphenyl)ethenyl]-1*H*-pyrazole (**2i**)
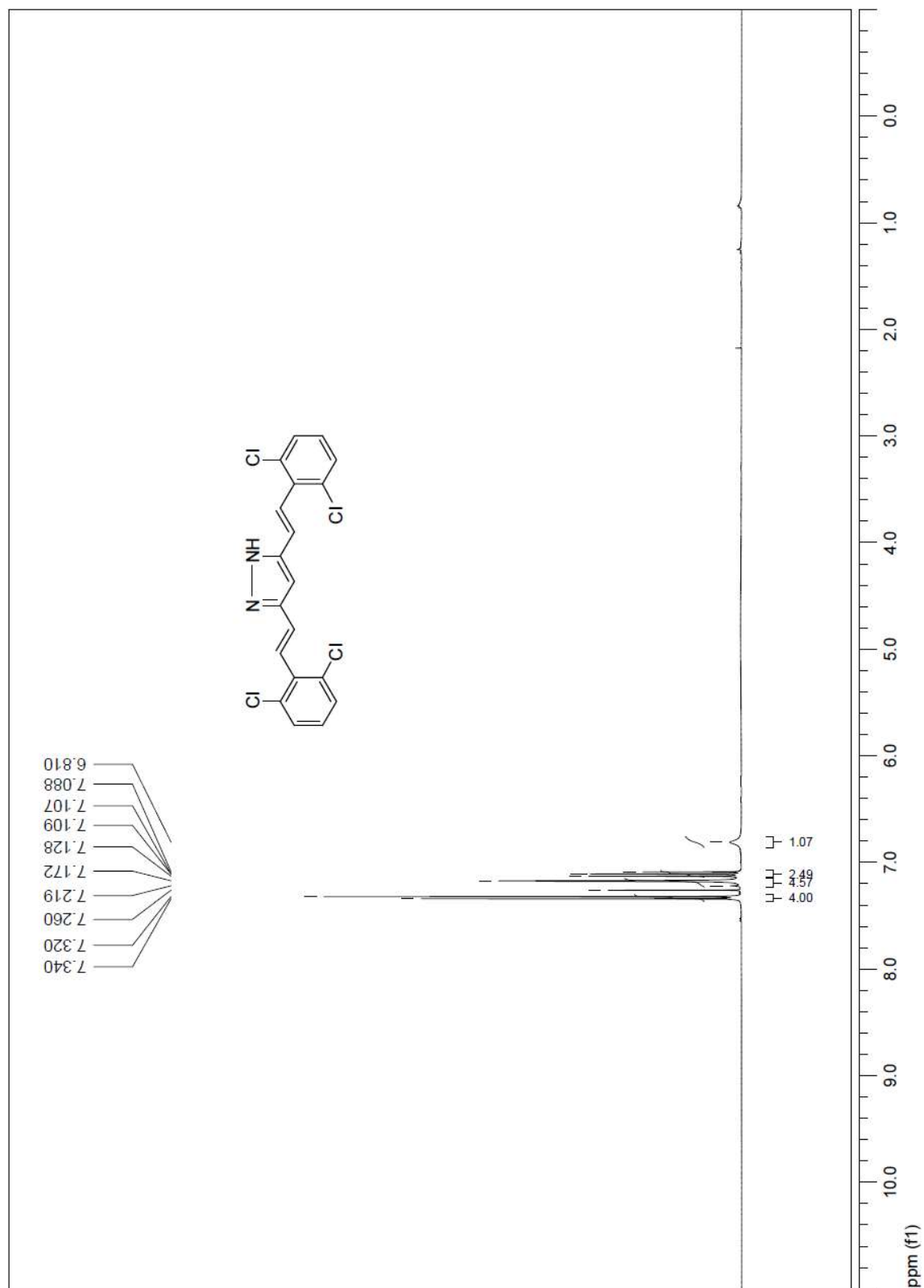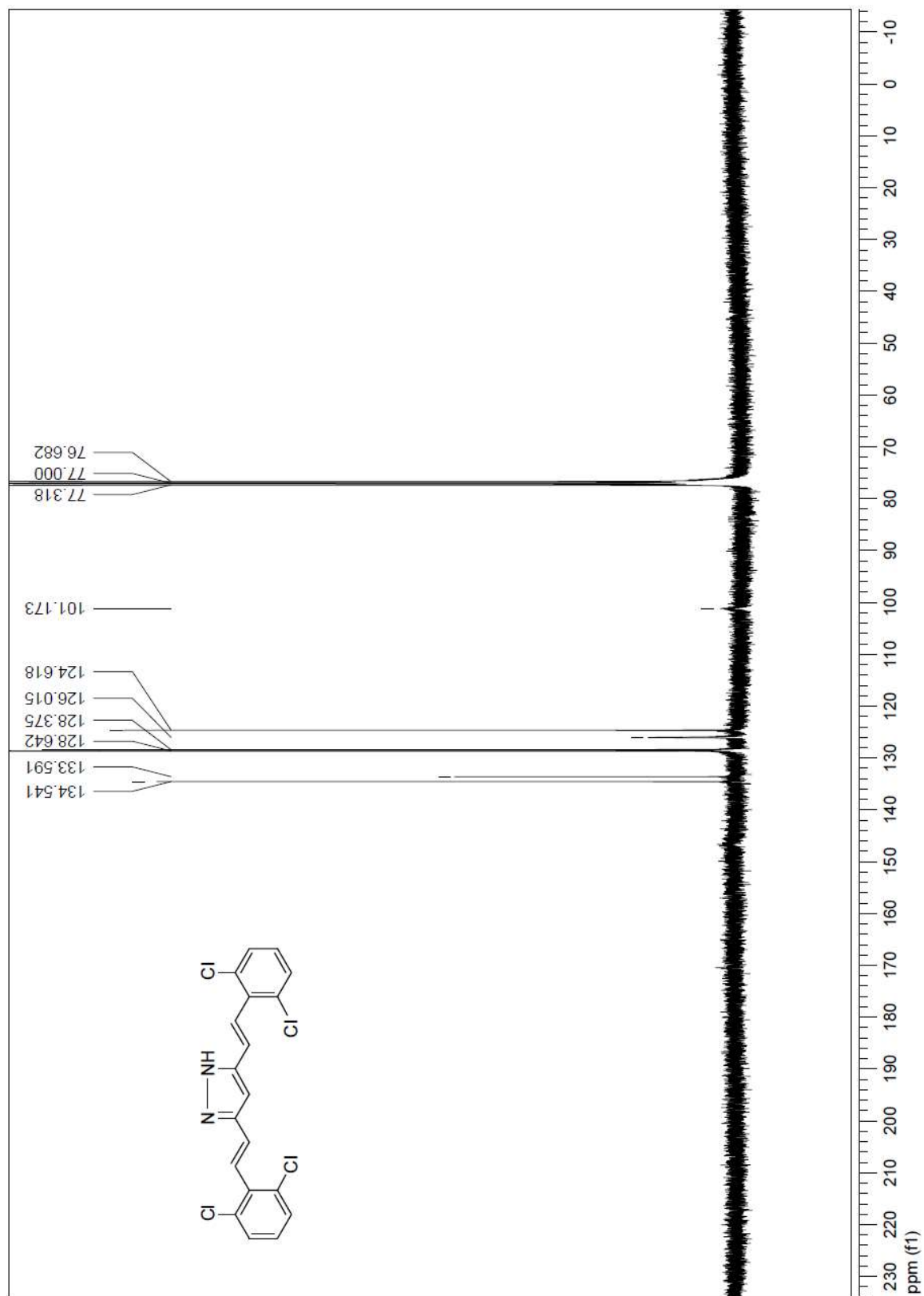
3,5-Bis[(1*E*)-2-(3-hydroxyphenyl)ethenyl]-1*H*-pyrazole (**2j**)

3,5-Bis[(1E)-2(2,6-dichlorophenyl)ethenyl]-1H-pyrazole (**2l**)

3,5-Bis[(1E)-2-(3-ethoxy-4-hydroxyphenyl)ethenyl]-1H-pyrazole (2c). **¹H NMR**
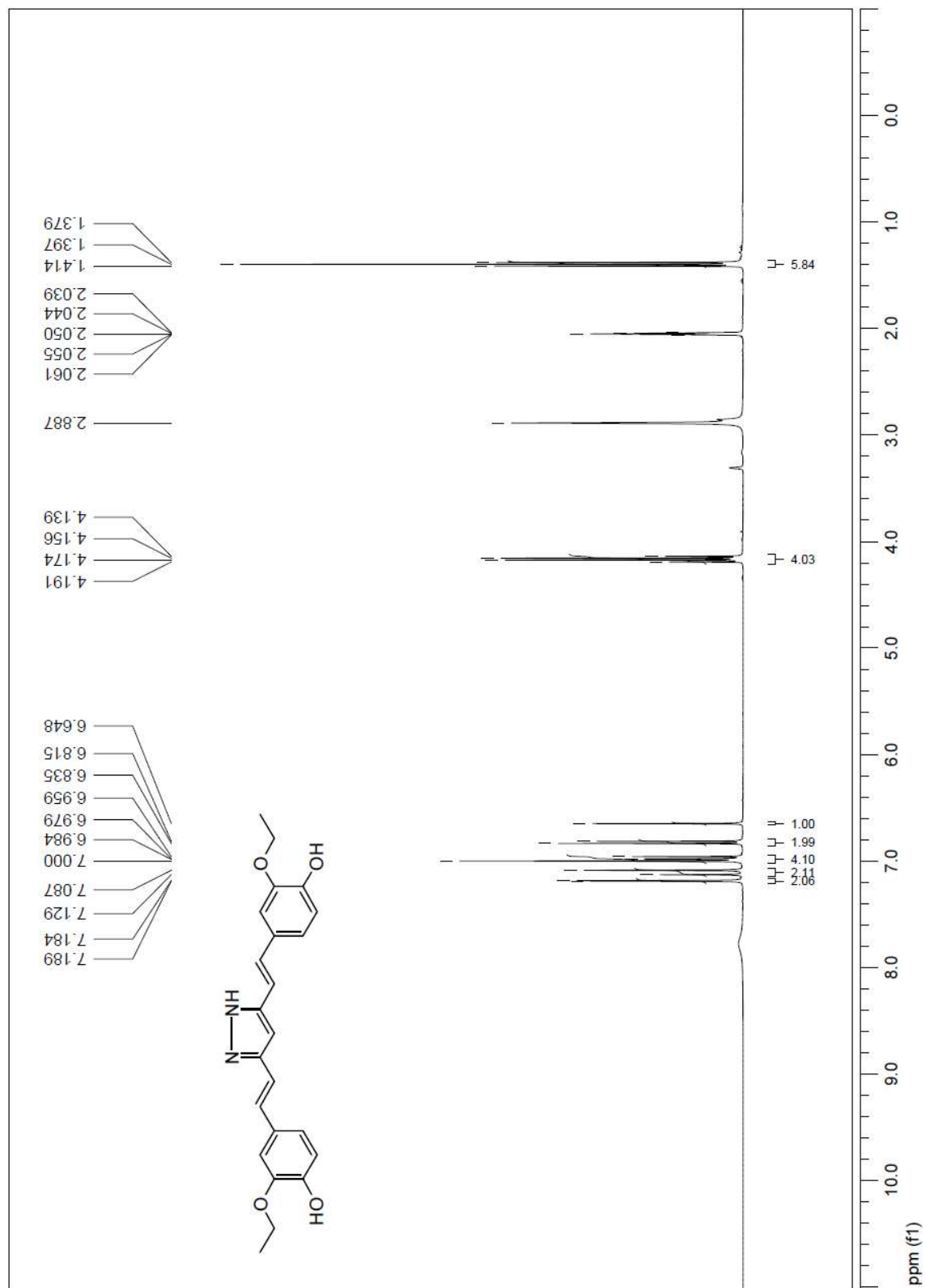
*3,5-Bis[(1E)-2-(3-ethoxy-4-hydroxyphenyl)ethenyl]-1H-pyrazole (**2c**).* **¹³C NMR**
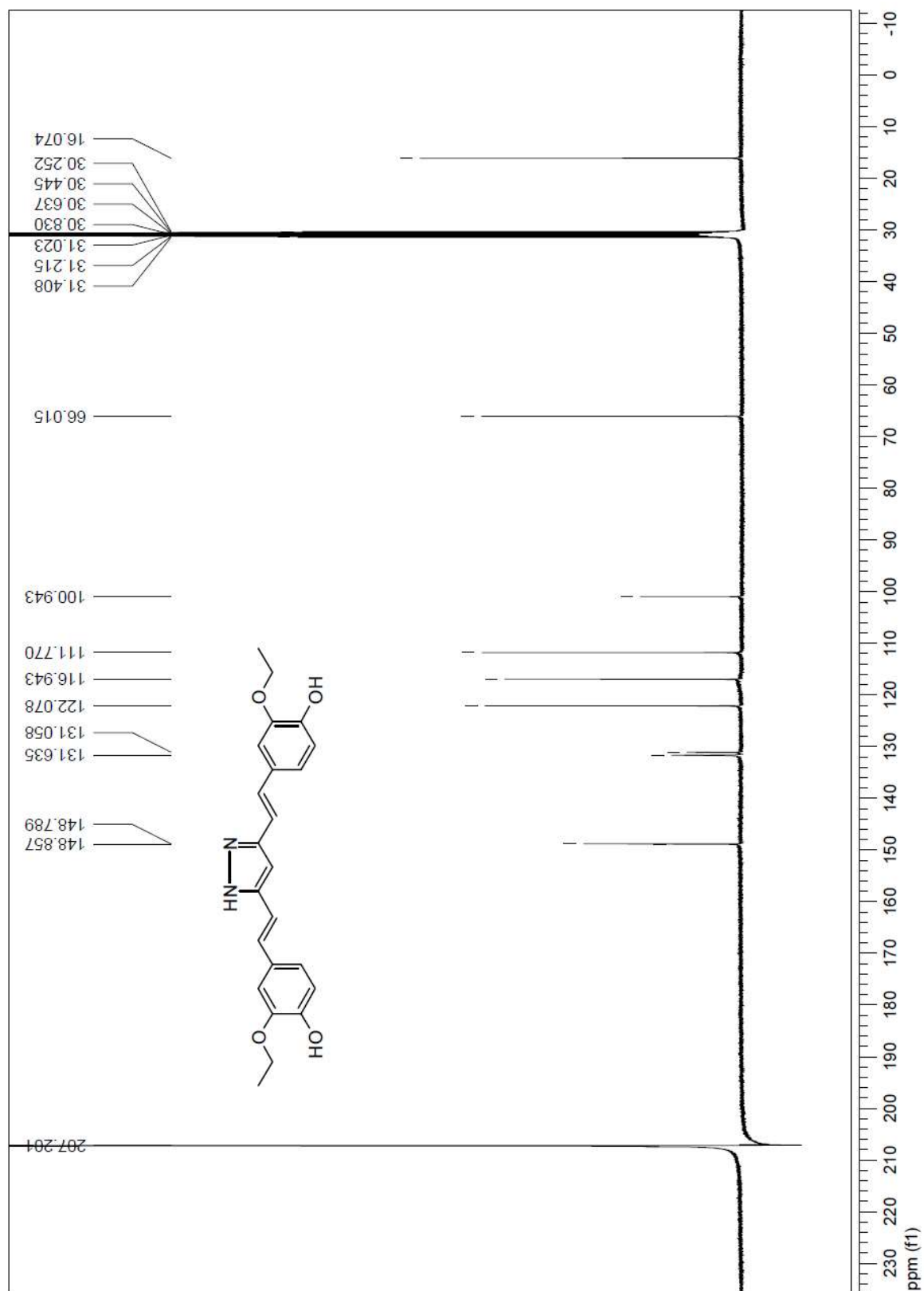
3,5-Bis[(1E)-2-(3-hydroxy-4-methoxyphenyl)ethenyl]-1H-pyrazole (2d). **^{1}H NMR**
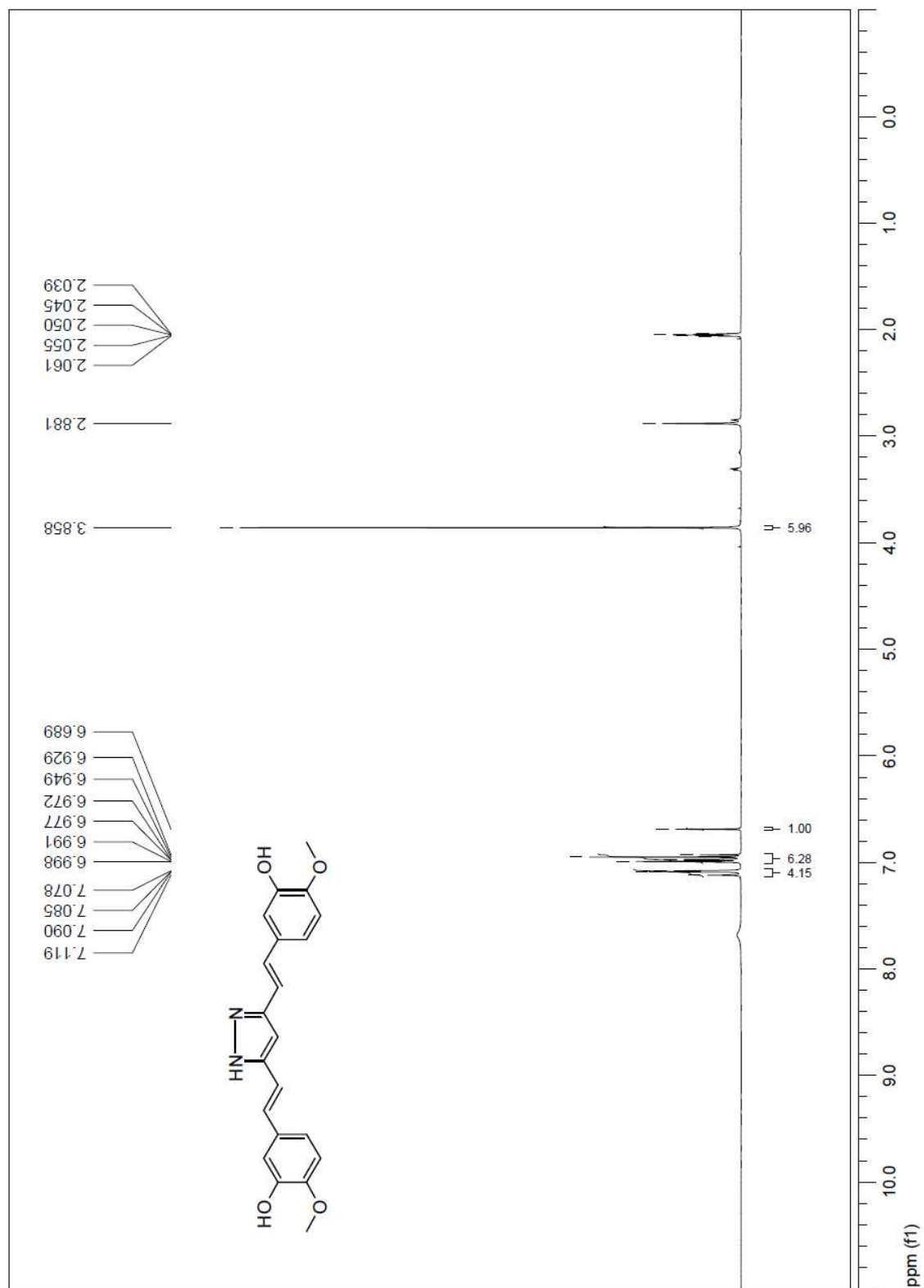
3,5-Bis[(1E)-2-(3-hydroxy-4-methoxyphenyl)ethenyl]-1H-pyrazole (2d). **¹³C NMR**
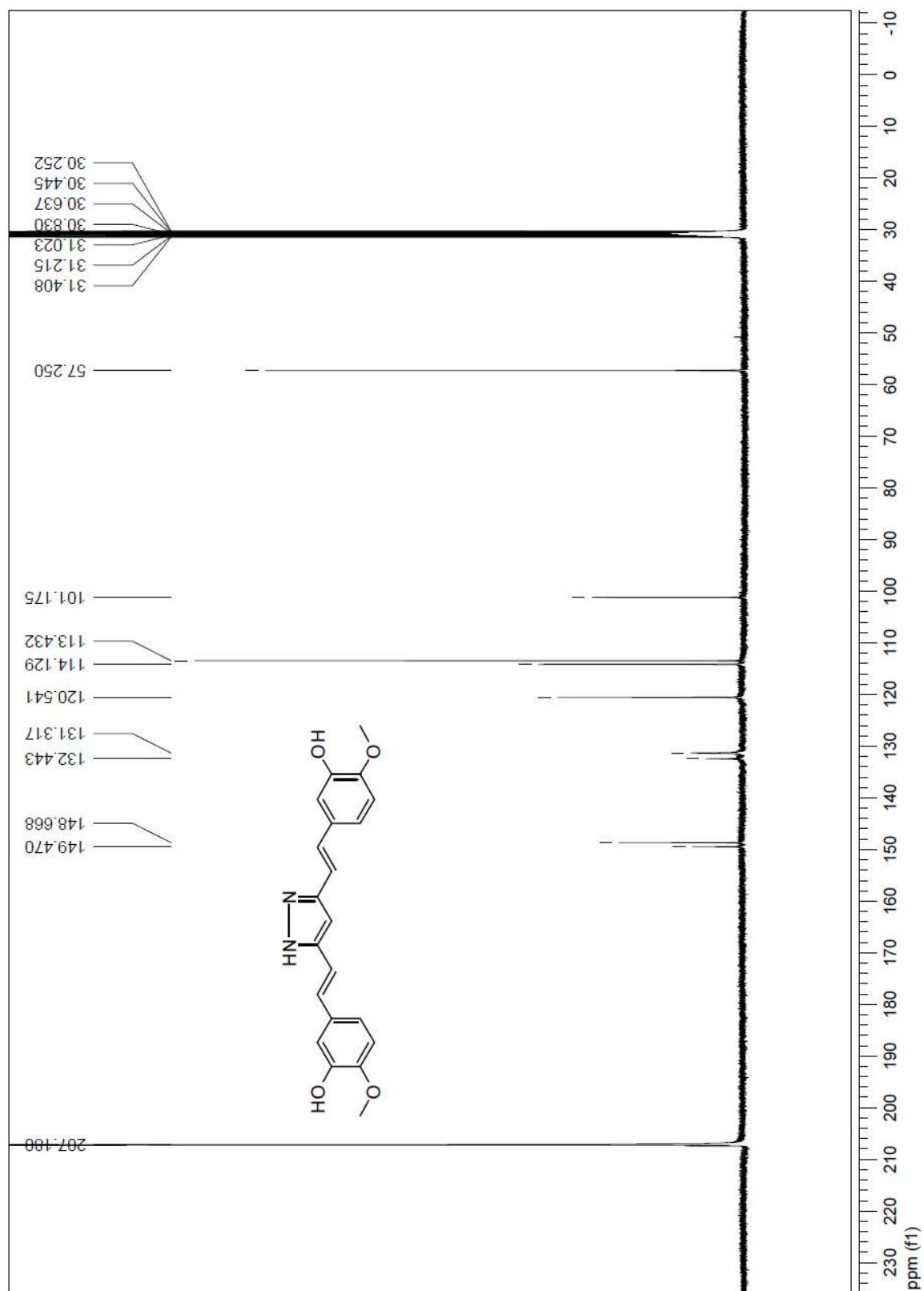
3,5-Bis[(1E)-2-(4-ethoxy-3-methoxyphenyl)ethenyl]-1H-pyrazole (2e). **¹H NMR**
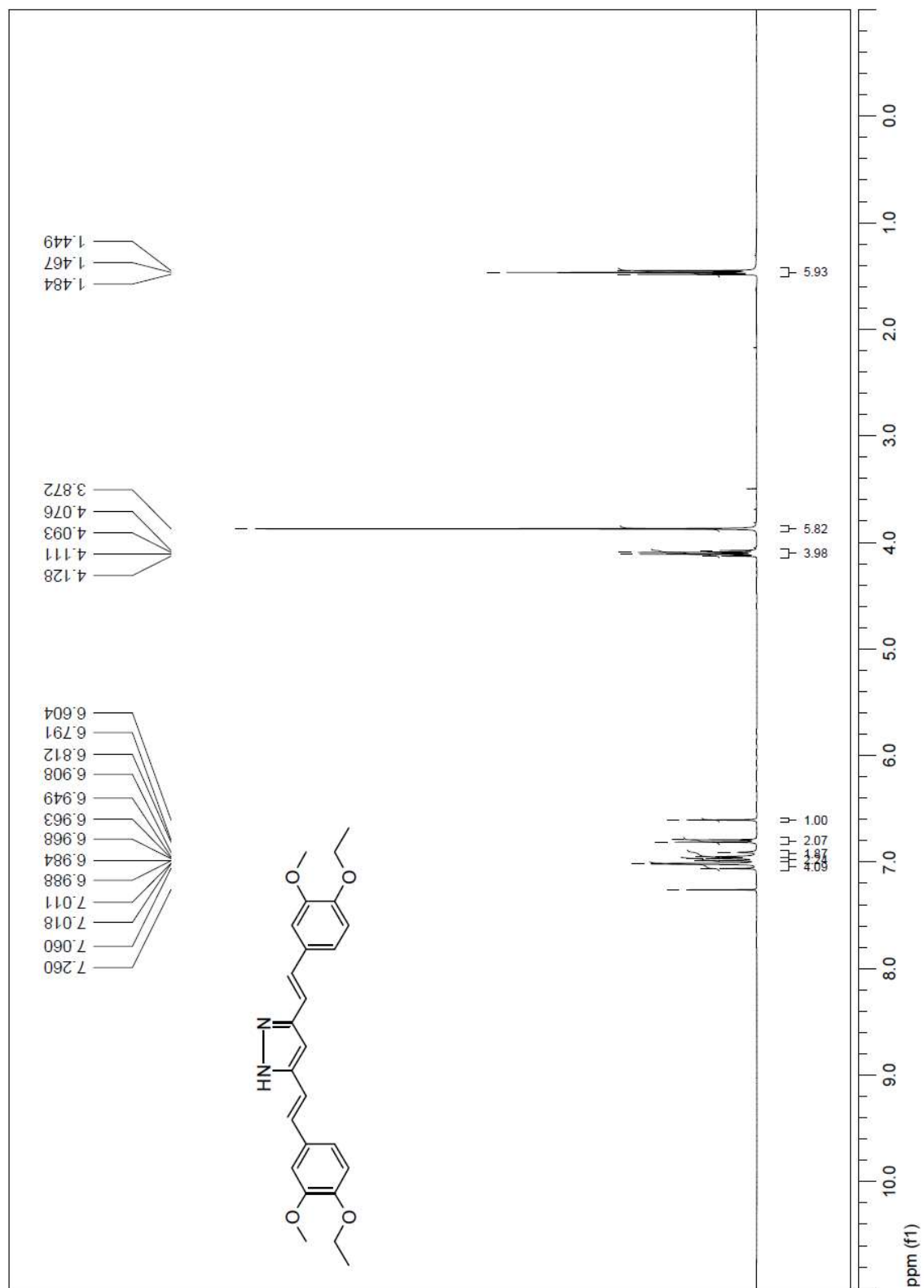
3,5-Bis[(1E)-2-(4-ethoxy-3-methoxyphenyl)ethenyl]-1H-pyrazole (2e). **¹³C NMR**
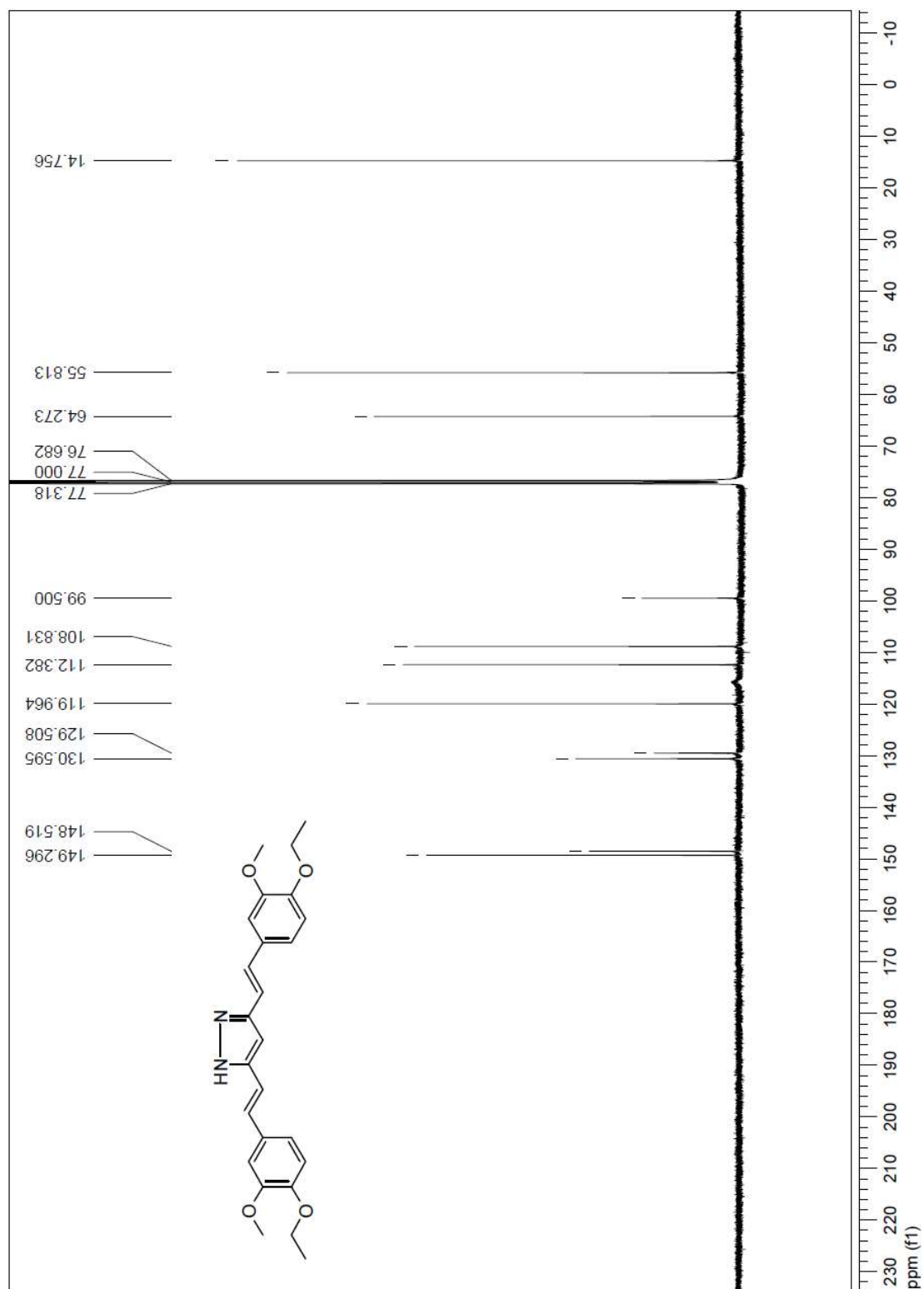
*3,5-Bis[(1E)-2-(4-methylphenyl)ethenyl]-1H-pyrazole (**2f**)*. **¹H NMR**
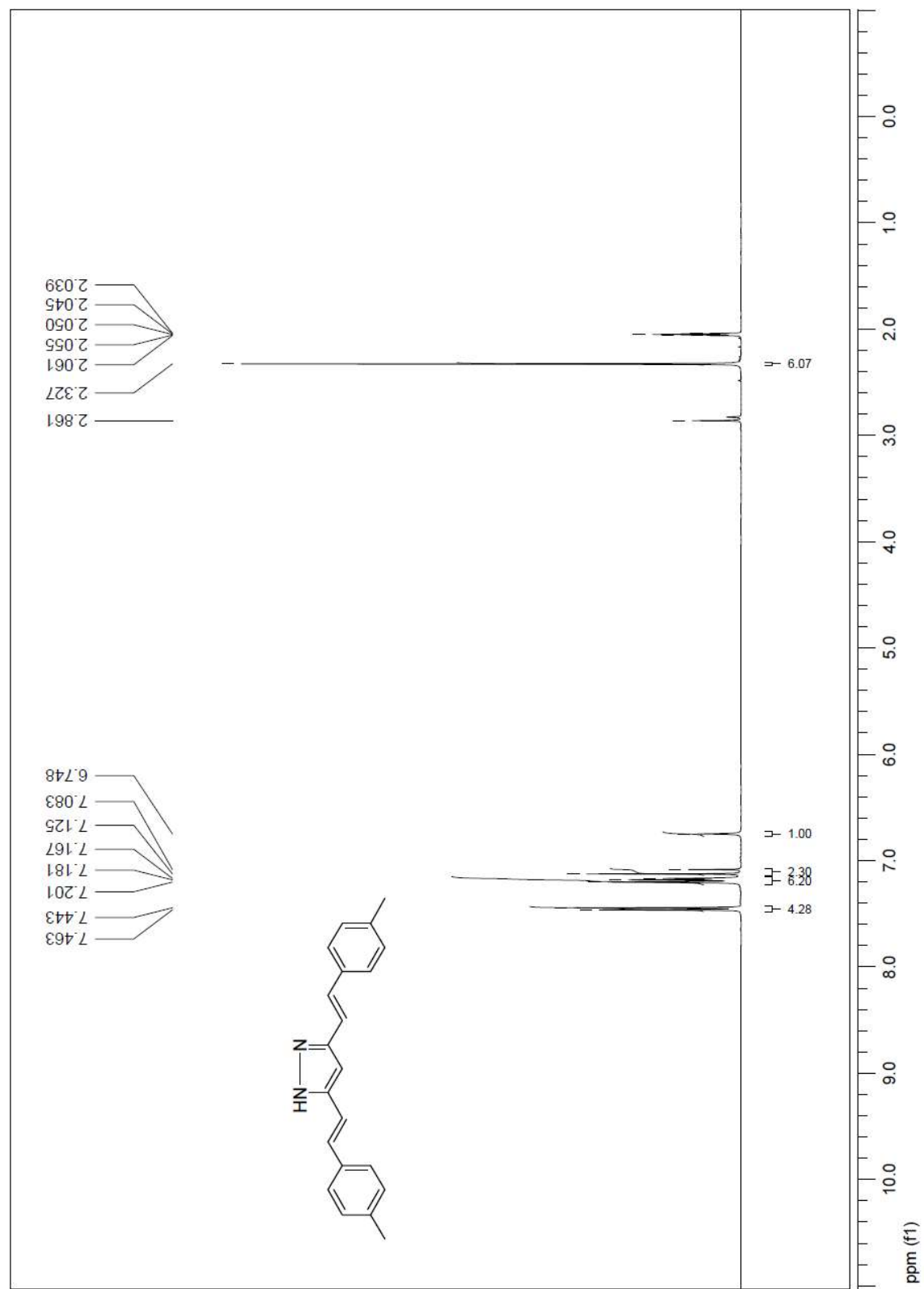
*3,5-Bis[(1E)-2-(4-methylphenyl)ethenyl]-1H-pyrazole (**2f**).* **¹³C NMR**
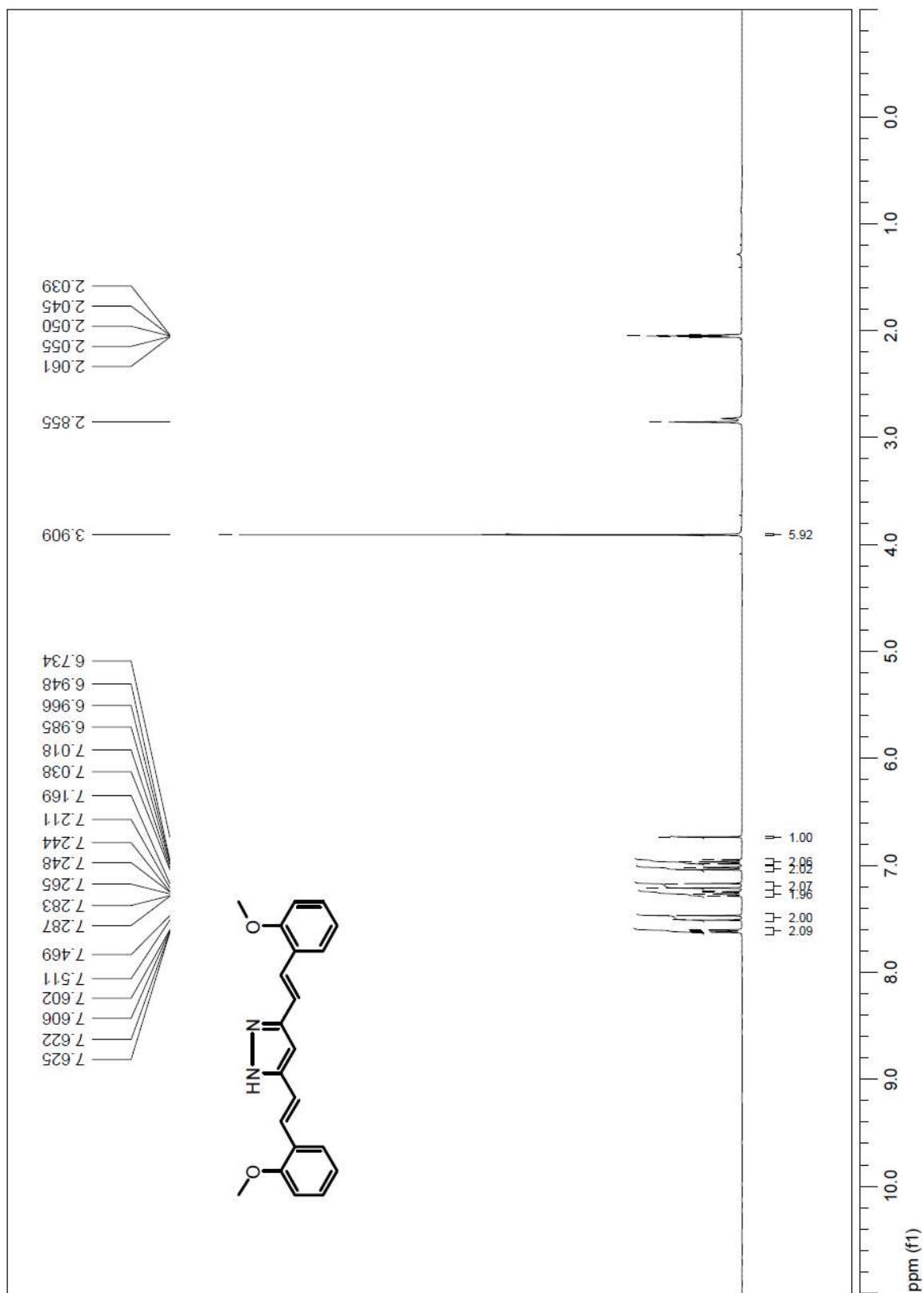
Peak labels:
- 22.202
- 30.252
- 30.445
- 30.637
- 30.830
- 31.023
- 31.215
- 31.408
- 101.681
- 128.146
- 131.217
- 136.283
- 139.329
- 207.130

ppm (f1)

*3,5-Bis[(1*E*)-2-(2-methoxyphenyl)ethenyl]-1*H-pyrazole (**2g**)*. **¹H NMR**

*3,5-Bis[(1*E)*-2-(2-methoxyphenyl)ethenyl]-1H-pyrazole (2g)*. **¹³C NMR**

207.160

158.973

130.716
128.346
127.669
126.351
122.510
113.032

101.535

56.869

31.408
31.215
31.023
30.830
30.638
30.445
30.252

230 220 210 200 190 180 170 160 150 140 130 120 110 100 90 80 70 60 50 40 30 20 10 0 -10
ppm (f1)

3,5-Bis[(1E)-2-(3-methoxyphenyl)ethenyl]-1H-pyrazole (2h). **¹H NMR**

3,5-Bis[(1E)-2-(3-methoxyphenyl)ethenyl]-1H-pyrazole (2h). **¹³C NMR**

3,5-Bis[(1E)-2-(4-methoxyphenyl)ethenyl]-1H-pyrazole (2i). **¹H NMR**

3,5-Bis[(1E)-2-(4-methoxyphenyl)ethenyl]-1H-pyrazole (2i). **¹³C NMR**

55.290

76.682
77.000
77.318

99.471

114.129
115.571

127.779
129.334
130.445

147.426

159.537

3,5-Bis[(1E)-2-(3-hydroxyphenyl)ethenyl]-1H-pyrazole (2j). **¹H NMR**

3,5-Bis[(1E)-2-(3-hydroxyphenyl)ethenyl]-1H-pyrazole (2j). **¹³C NMR**
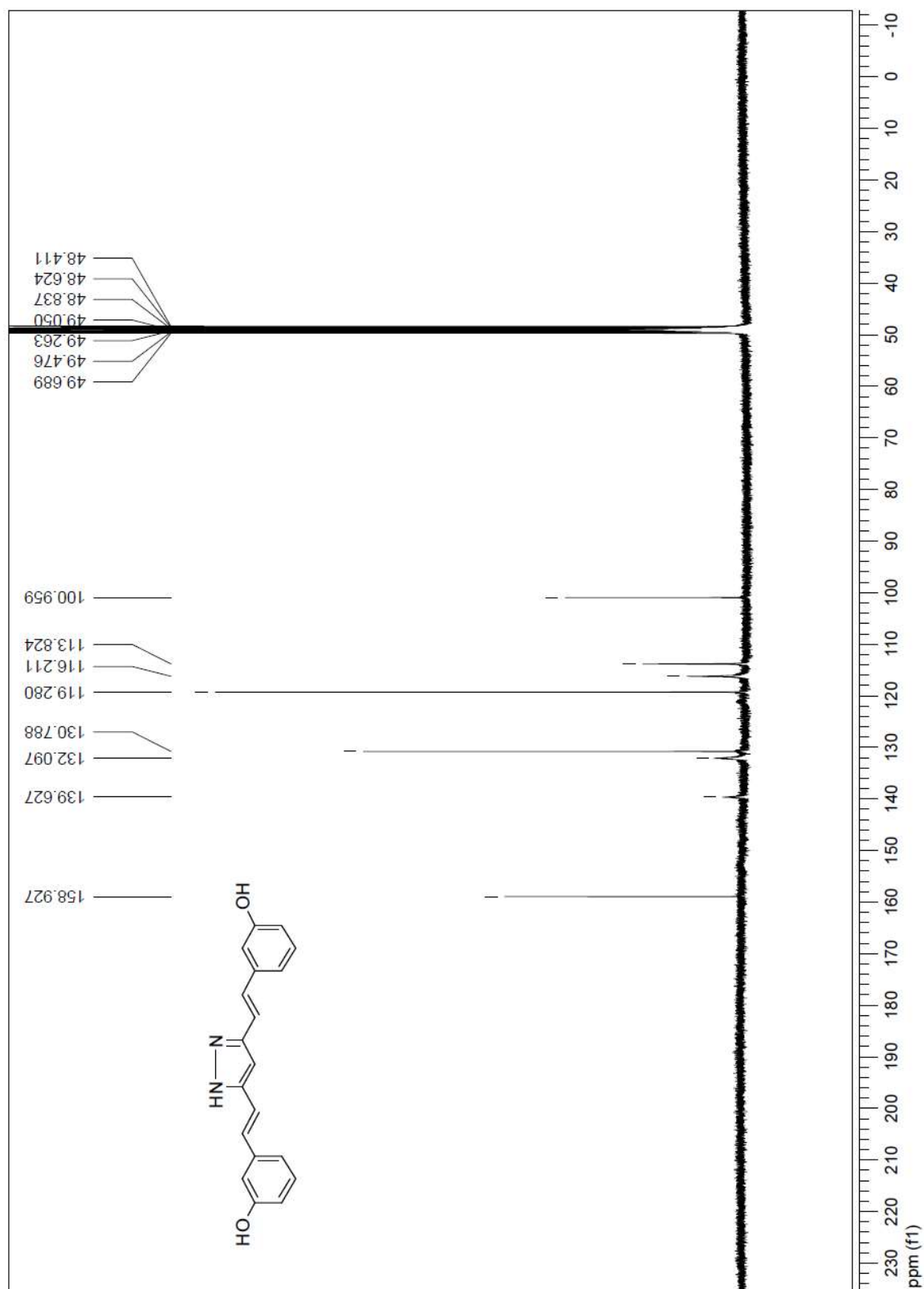
3,5-Bis[(1E)-2-(2,6-dichlorophenyl)ethenyl]-1H-pyrazole (2l). **¹H NMR CD₃OD**

3,5-Bis[(1E)-2(2,6-dichlorophenyl)ethenyl]-1H-pyrazole (2l). **¹H NMR**

6.810
7.088
7.107
7.109
7.128
7.172
7.219
7.260
7.320
7.340

1.07
2.49
4.57
4.00

ppm (f1)

*3,5-Bis[(1*E)-2(2,6-dichlorophenyl)ethenyl]-1H-*pyrazole (**2l**).* **¹³C NMR**

SUPPLEMENTAL TABLE 1

Linearity data for the standard curves for 3,5-bis(styryl)pyrazole **2a**

Standard curve	Slope	95 % confidence interval of slope	Intercept	95 % confidence interval of intercept	R^2
1	$1.623 \times 10^8 \pm 3.792 \times 10^6$	$1.517 \times 10^8 - 1.728 \times 10^8$	$-6.268 \times 10^5 \pm 1.477 \times 10^5$	$-1.037 \times 10^6 - -2.169 \times 10^5$	0.9978
2	$1.604 \times 10^8 \pm 3.908 \times 10^6$	$1.496 \times 10^8 - 1.713 \times 10^8$	$-5.814 \times 10^5 \pm 1.522 \times 10^5$	$-1.004 \times 10^6 - -1.590 \times 10^5$	0.9976
3	$1.616 \times 10^8 \pm 3.121 \times 10^6$	$1.529 \times 10^8 - 1.703 \times 10^8$	$-5.725 \times 10^5 \pm 1.216 \times 10^5$	$-9.099 \times 10^5 - -2.350 \times 10^5$	0.9985
Mean	1.614×10^8		-5.936×10^5		0.9980
SD	9.609×10^5		2.912×10^4		0.0005

The concentration range was between 0.01 - 0.06 mg/mL with six concentrations for each standard curve.

SUPPLEMENTAL TABLE 2

Linearity data for the standard curves for 3,5-bis(styryl)pyrazole **2l**

Standard curve	Slope	95 % confidence interval of slope	Intercept	95 % confidence interval of intercept	R^2
1	$8.090 \times 10^7 \pm 2.609 \times 10^6$	$7.366 \times 10^7 - 8.814 \times 10^7$	$-2.508 \times 10^5 \pm 1.016 \times 10^5$	$-5.328 \times 10^5 - 3.125 \times 10^4$	0.9959
2	$7.988 \times 10^7 \pm 2.507 \times 10^6$	$7.292 \times 10^7 - 8.684 \times 10^7$	$-2.371 \times 10^5 \pm 9.762 \times 10^4$	$-5.081 \times 10^5 - -3.389 \times 10^4$	0.9961
3	$8.127 \times 10^7 \pm 2.608 \times 10^6$	$7.403 \times 10^7 - 8.851 \times 10^7$	$-2.338 \times 10^5 \pm 1.016 \times 10^5$	$-5.158 \times 10^5 - 4.823 \times 10^4$	0.9959
Mean	8.068×10^7		-2.406×10^5		0.9980
SD	7.199×10^5		9.015×10^3		0.0001

The concentration range was between 0.01 - 0.06 mg/mL with six concentrations for each standard curve.

SUPPLEMENTAL TABLE 3

2a and **2l** treatment induced apoptotic cell death in A549, B16F10 and Huh-7 cells.

Compound	A549 (% dead cells)	B16F10 (% dead cells)	Huh-7 (% dead cells)
Control	6.7 ± 0.7	7.2 ± 0.8	4.0 ± 1.9
4 µM 2a	8.0 ± 4.0	19.6 ± 3.1	5.9 ± 1.9
8 µM 2a	18.8 ± 4.1	31.5 ± 5.4	17.3 ± 8.1
4 µM 2l	12.5 ± 2.7	12.1 ± 1.6	30.7 ± 4.5
8 µM 2l	17.3 ± 2.0	55.1 ± 5.2	37.9 ± 2.6

Data represent mean $\pm$ standard deviation of four independent replicates (n = 3).

SUPPLEMENTAL TABLE 4

Cell cycle analysis of PC3 cells after treatment with 3,5-bis(styryl)pyrazoles **2a** and **2l** (GI_{50} concentrations) showing the percentage of cells in each phase of the cell cycle.

	G_0/G_1	S	G_2/M
Control	72.2 ± 0.4	10.6 ± 1.1	17.1 ± 1.3
2a	9.2 ± 2.5	3.0 ± 1.2	87.6 ± 5.0
2l	5.3 ± 1.1	5.0 ± 1.2	89.8 ± 1.8

Data represent mean $\pm$ standard deviation of four independent replicates (n = 4).

SUPPLEMENTAL TABLE 5

Quantification of live / dead cells after treating PC3 cells with 4 and 8 μM **2a** and **2l** for 2 and 4 hours.

	Compound	PC3 (% dead cells)
	Control	2.7 ± 0.5
	4 μM 2a	3.2 ± 0.8
2 hours	8 μM 2a	3.4 ± 0.8
	4 μM 2l	4.0 ± 1.1
	8 μM 2l	3.9 ± 1.2
	4 μM 2a	3.8 ± 0.9
4 hours	8 μM 2a	4.1 ± 0.8
	4 μM 2l	4.3 ± 1.0
	8 μM 2l	4.1 ± 0.6

Data represent mean ± standard deviation of four independent replicates (n = 3).
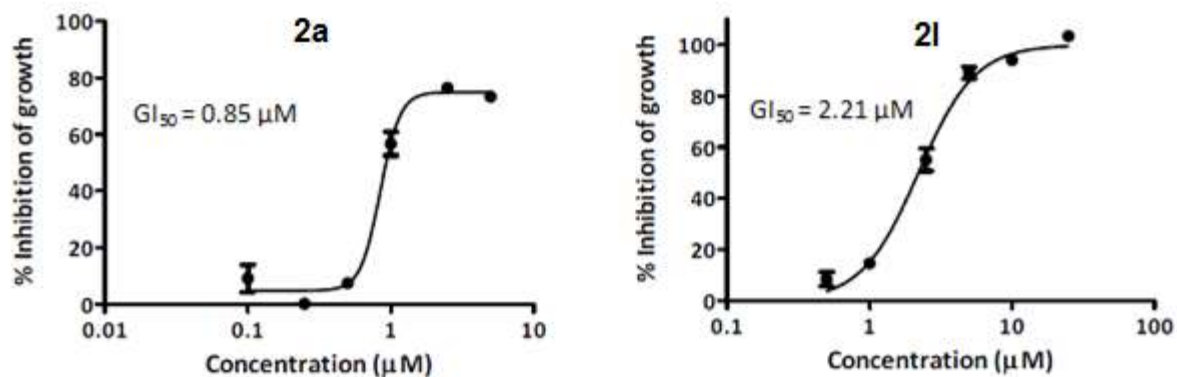
Supplemental Figure 1

Dose-response curves of percentage growth inhibition *vs* log concentrations of 3,5-bis(styryl)pyrazoles **2a** and **2l**. Data represent mean ± standard deviation of three independent replicates (n = 3).

(A)

(B)
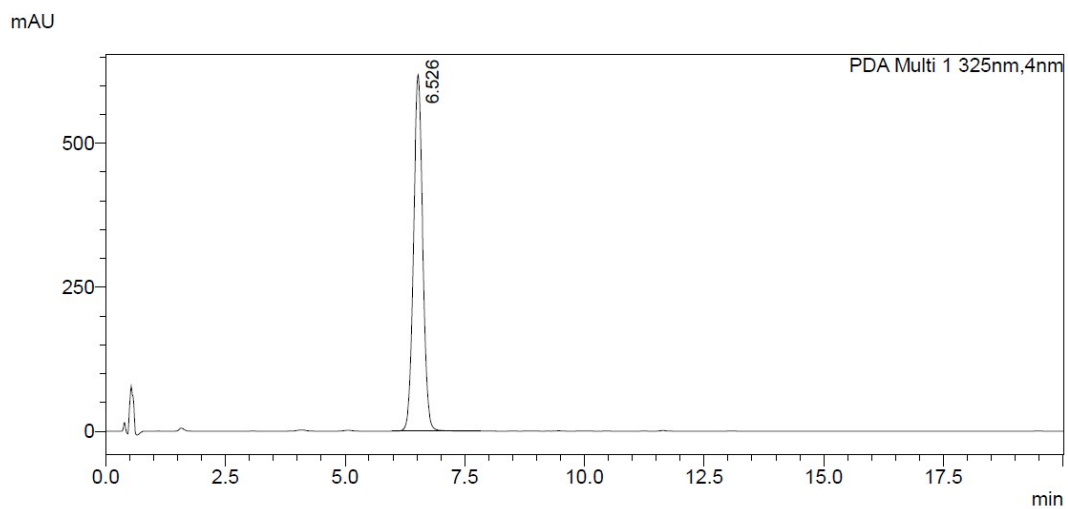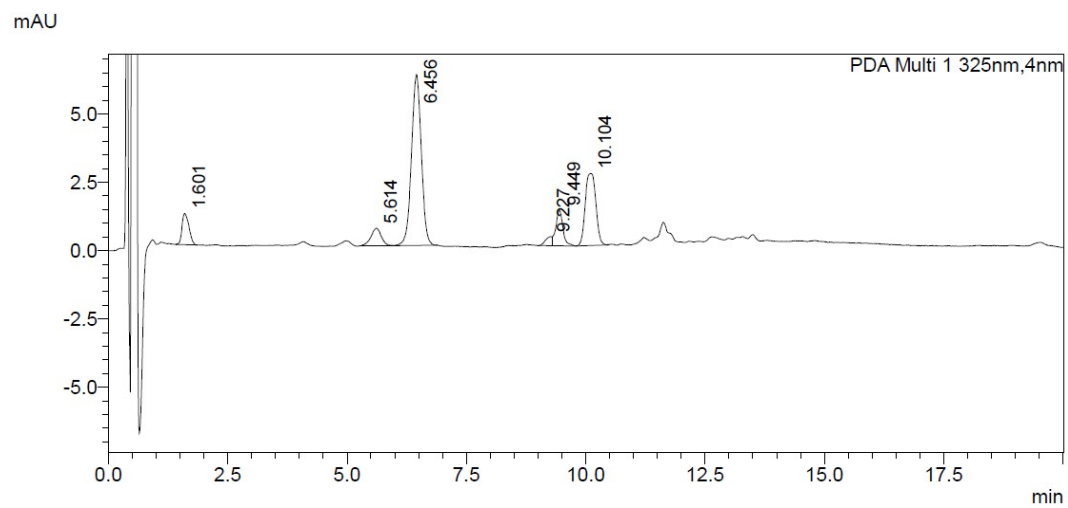
Supplemental Figure 2

HPLC chromatograms of the stability test for 3,5-bis(styryl)pyrazole **2a**; **(A)** t = 0 and **(B)** t = 72.

(A)

(B)
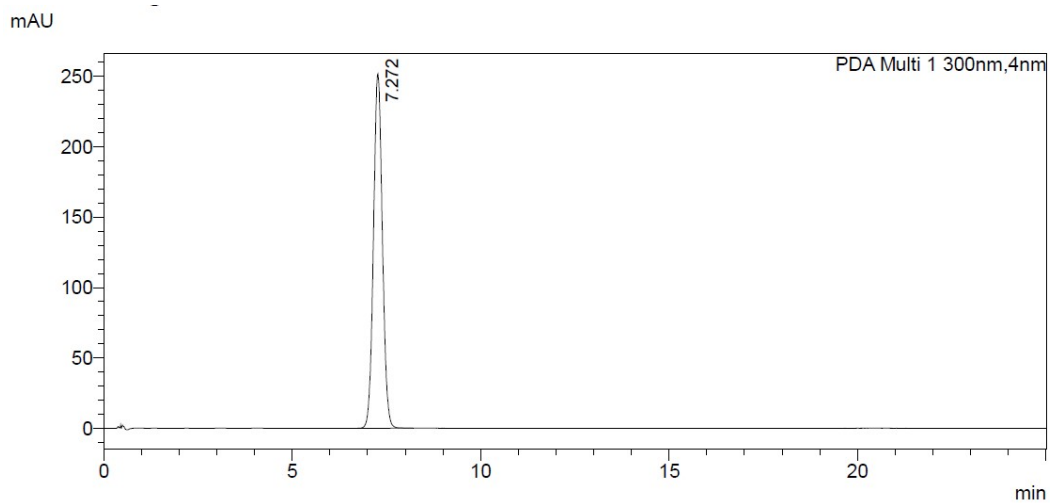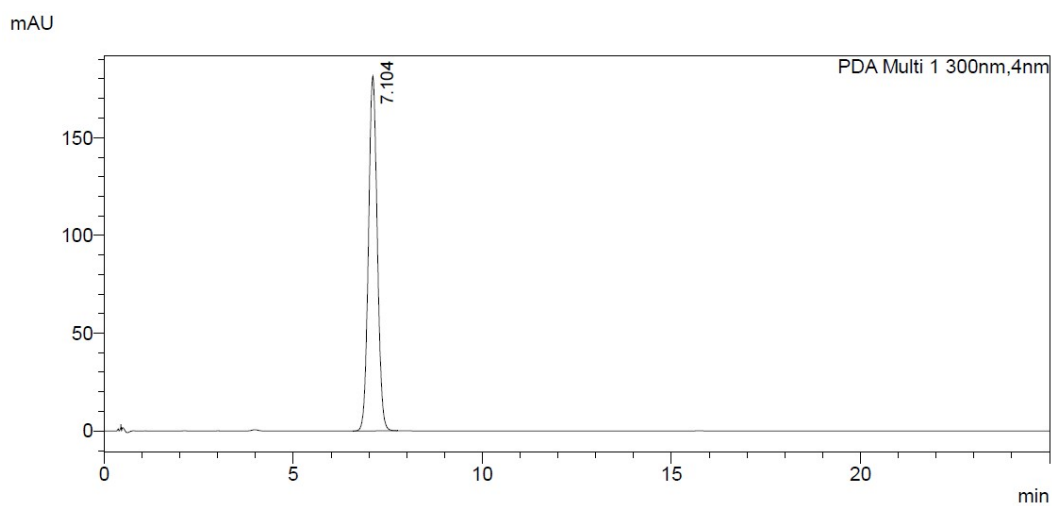
Supplemental Figure 3

HPLC chromatograms of the stability test for 3,5-bis(styryl)pyrazole **2l**; **(A)** t = 0 and **(B)** t = 72.
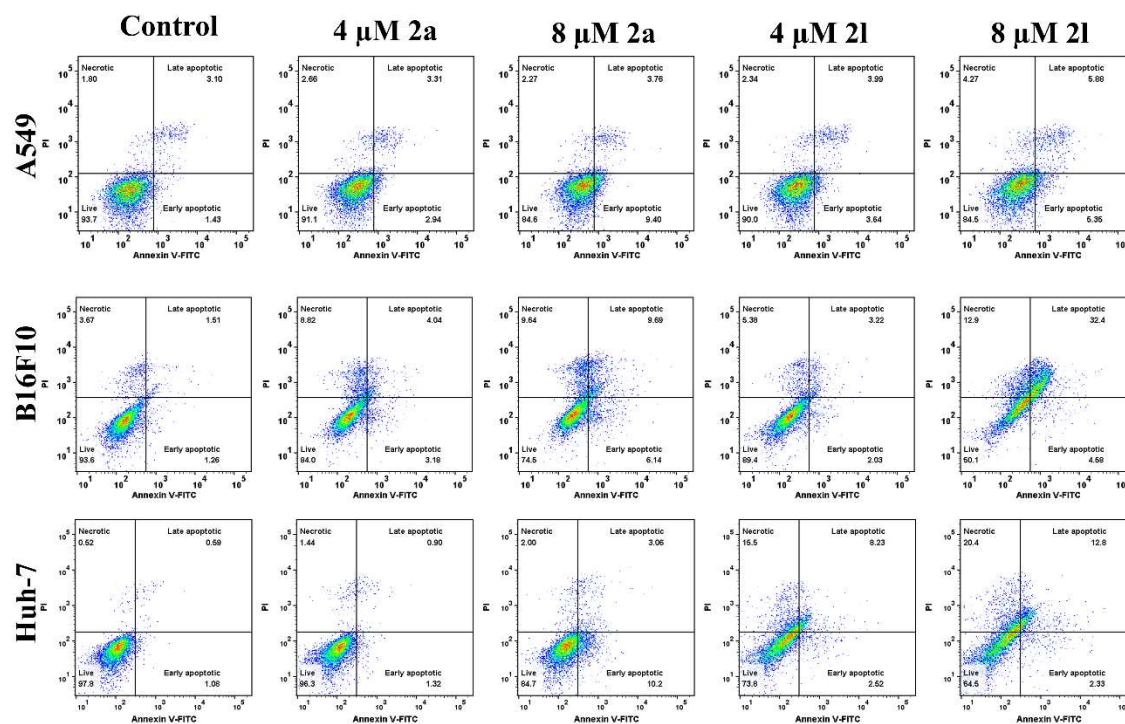
Supplemental Figure 4

Representative dot plots of Annexin-PI staining to determine the percentage of cell death after treatment with 0.1% DMSO (control); **2a** (4 µM); **2a** (8 µM); **2l** (4 µM); and **2l** (8 µM) in three different cell lines (A549, B16F10 and Huh-7) after 24 hours of treatment. The experiment was performed three times.
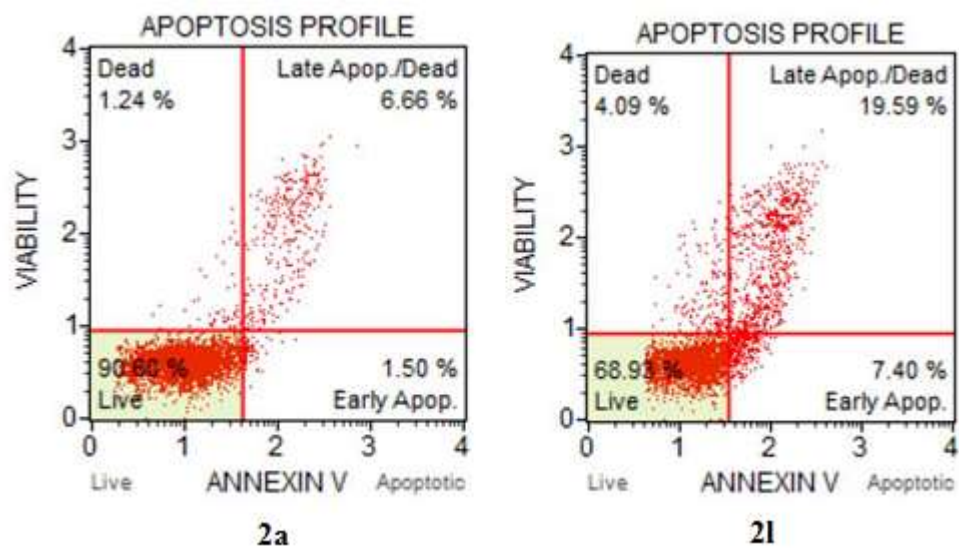
Supplemental Figure 5

Representative dot plot for the annexin V/PI apoptosis assay of PC3 cells 72 hours after the removal of 3,5-bis(styryl)pyrazoles **2a** and **2l** (GI_{50} concentrations).

(A)   (B)
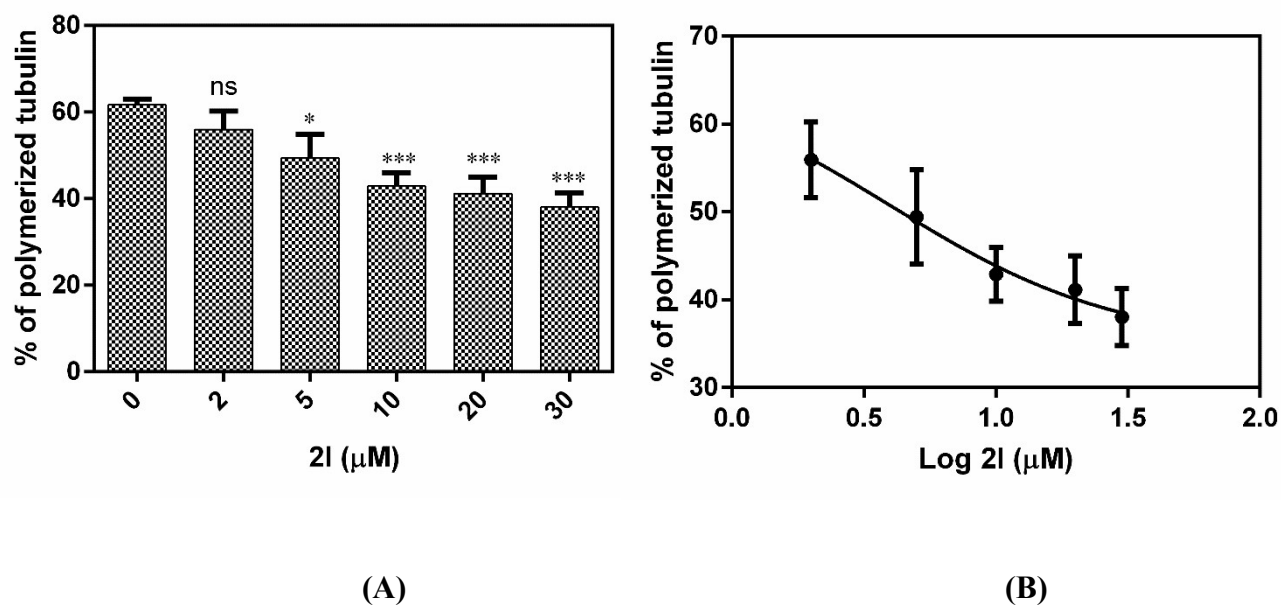
Supplemental Figure 6

Inhibition of tubulin polymerization by 3,-5-bis(styryl)pyrazole **2l** determined by quantifying the amount of microtubules formed in the absence and the presence of different concentrations of **2l** by sedimentation assay; **(A)** percentage of tubulin polymerization quantified by pelleting microtubules at different concentrations of **2l**; **(B)** Determination of IC_{50} of inhibition of tubulin polymerization by **2l** by fitting the data in dose-response inhibition curve in GraphPad Prism software. The experiment was repeated three times and error bars show standard deviations.

(A)

(B)
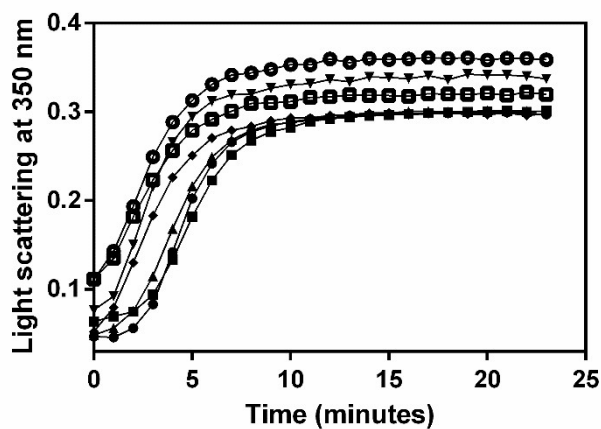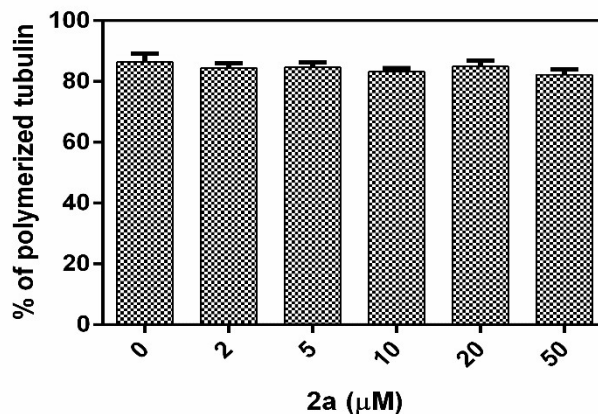
Supplemental Figure 7

Effect of increasing concentrations of **2a** on tubulin polymerization; **(A)** light scattering was observed at similar conditions to **2l**. Tubulin was polymerized without (●) and with 2 (■), 5 (▲), 10 (▼), 20 (♦), 30 (○) and 50 (□) μM of **2a**; **(B)** The amount of polymerized tubulin was determined by sedimentation assay similar to that performed with **2l**. Each experiment was repeated three times and error bar represents standard deviation.

(A)   (B)
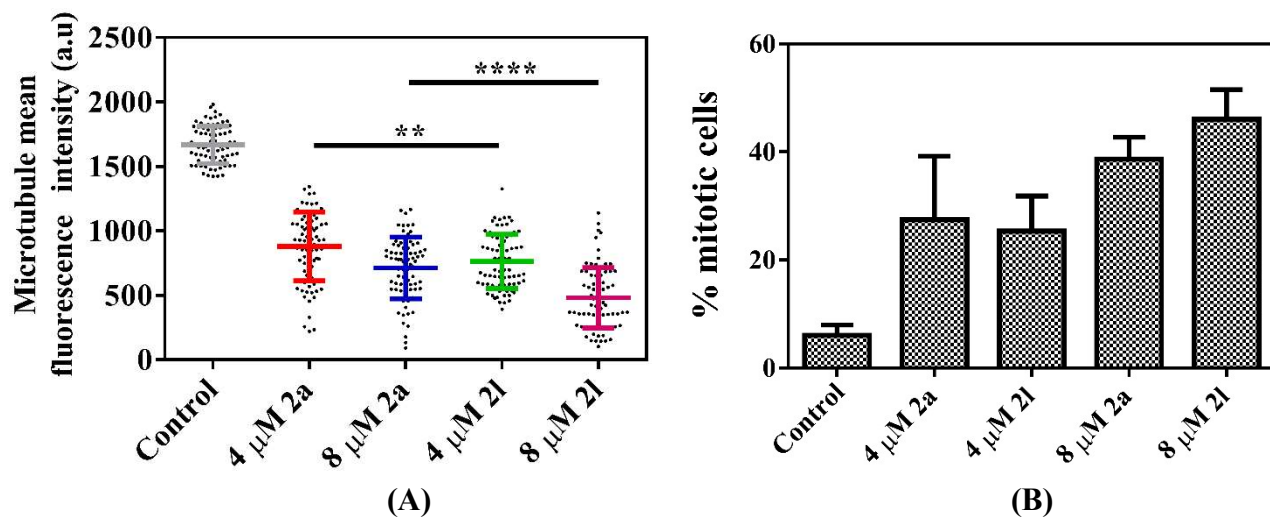
Supplemental Figure 8

(A) The fluorescence intensity of the interphase microtubules in PC3 cells in the absence and presence of 4 and 8 μM of **2a** and **2l**. 200 cells were monitored in each condition. ******represents p < 0.01; ********represents p < 0.0001 by Student's t-test. **(B)** Quantification of percentage of mitotic cells of PC3 cells in the absence and presence of 4 and 8 μM of **2a** and **2l**. Each experiment was repeated three times and error bars represents standard deviation.
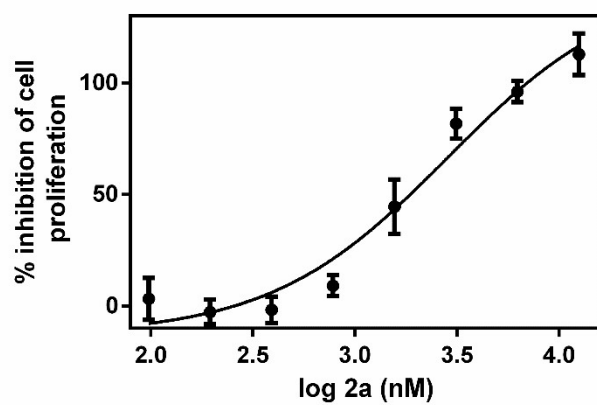
(A)
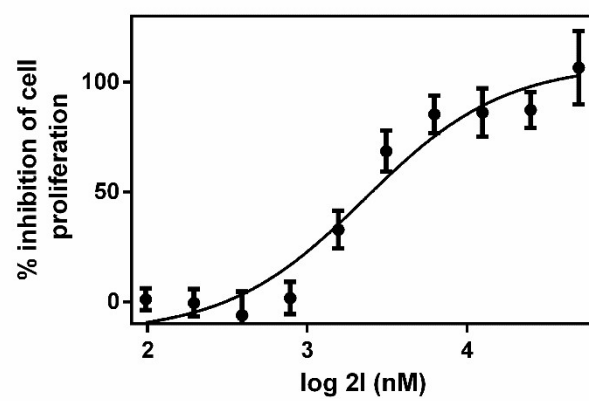
(B)
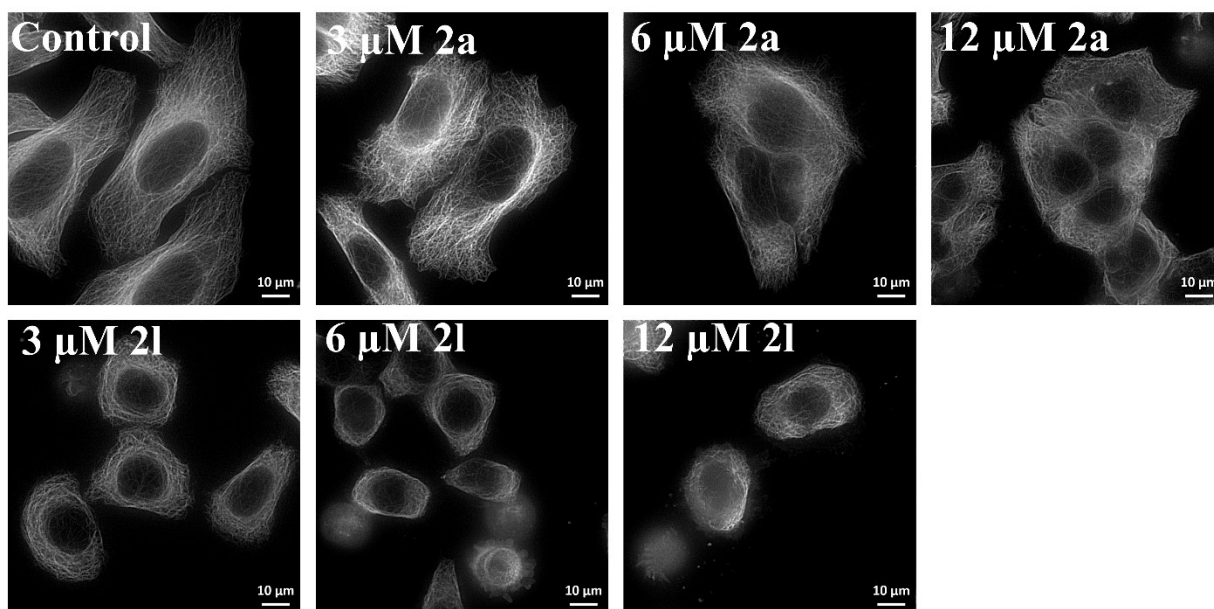
(C)

(D)
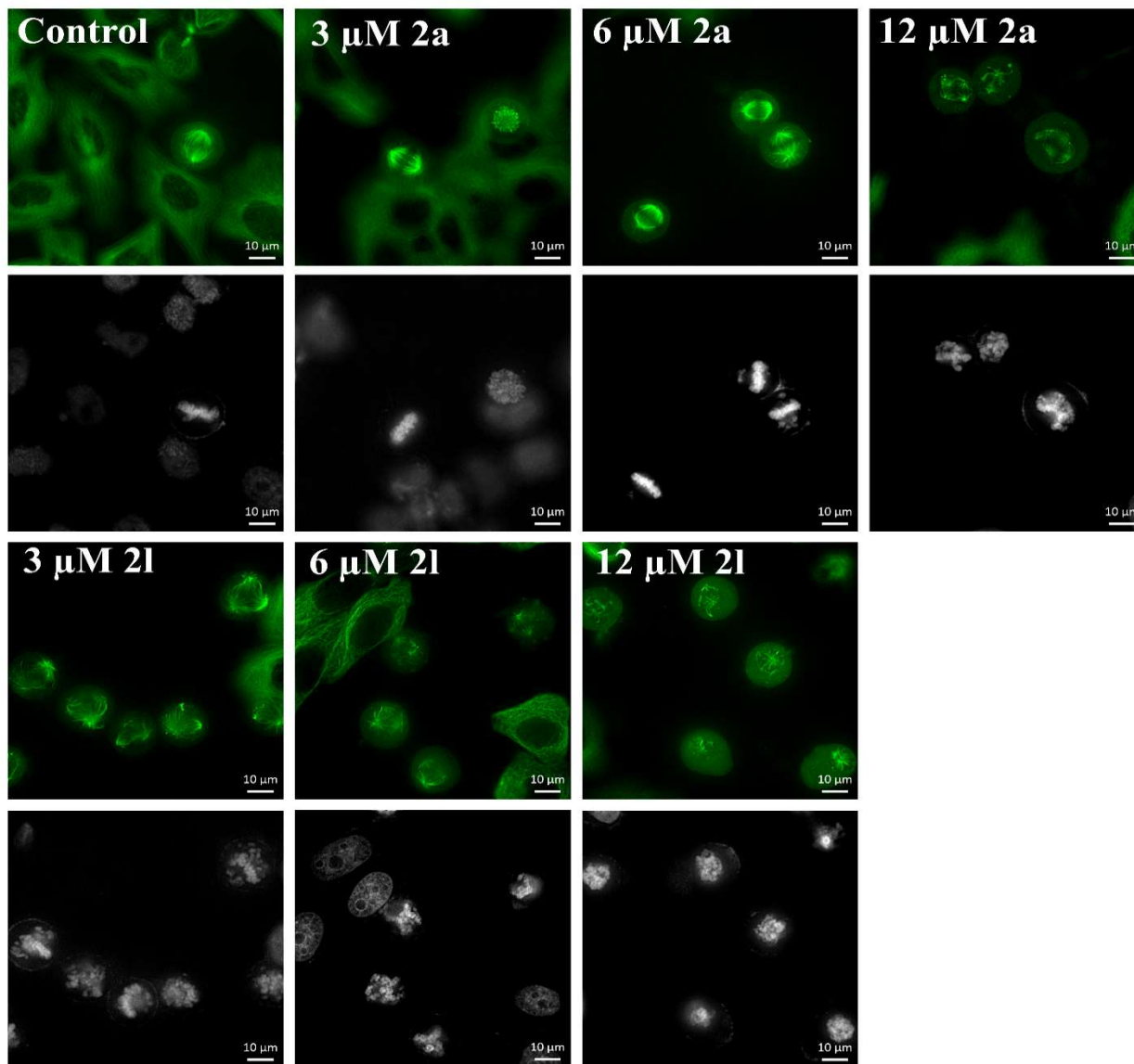
Supplemental Figure 9

Effect of 3,5-bis(styryl)pyrazoles **2a** and **2l** on HeLa cells. The GI_{50} values for **2a (A)** and **2l (B)** were determined by the Sulphorhodamine B assay. The experiment was performed three times and error bars represent standard deviation. The effect of these compounds on the microtubules of HeLa cells was determined by microtubule staining. Representative fluorescence microscope images of interphase microtubules **(C)** and mitotic microtubules **(D)** are shown after control (0.1 % DMSO treated) and treatment with **2a** and **2l** treatment (3, 6, and 12 µM). The scale bars are shown in the figures.

(A)

(B)
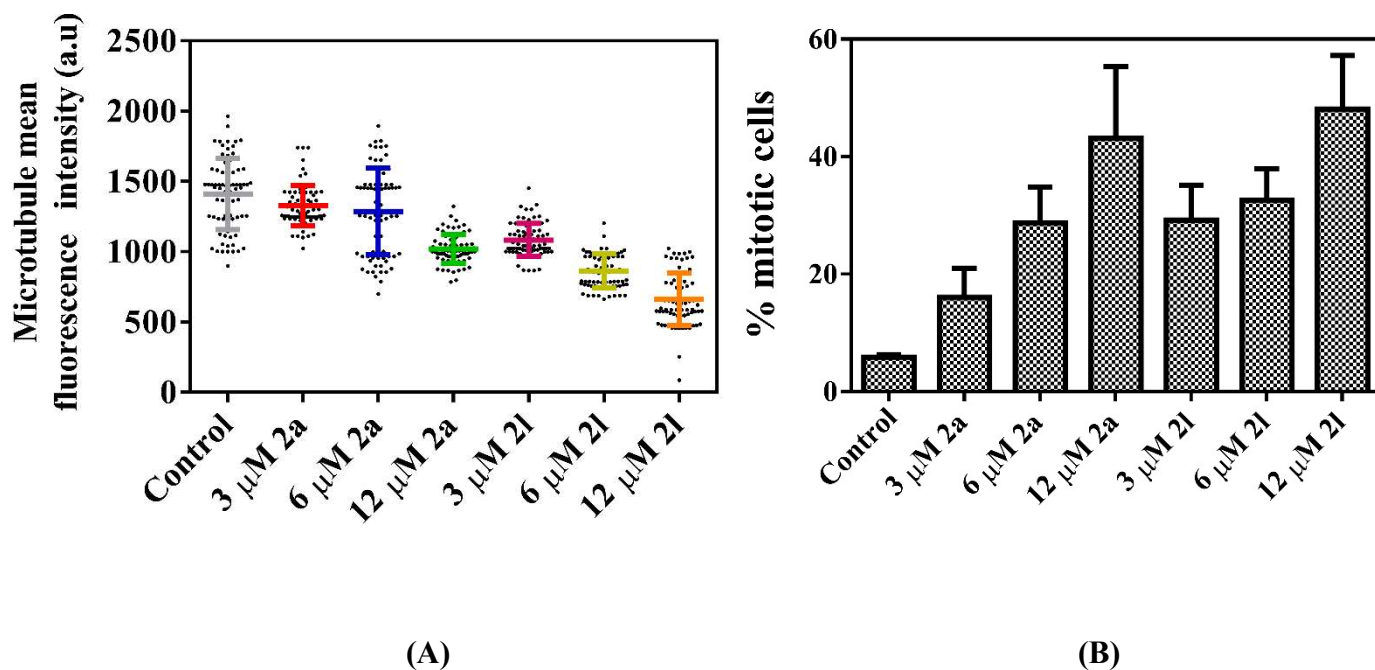
Supplemental Figure 10

(A) Quantification of interphase microtubule intensity of HeLa cells in the absence and presence of 3, 6 and 12 μM of **2a** and **2l**. **(B)** Quantification of percentage of mitotic cells of HeLa cells in the absence and presence of 3, 6 and 12 μM of **2a** and **2l**. Each experiment was repeated three times and error bar represents standard deviation.
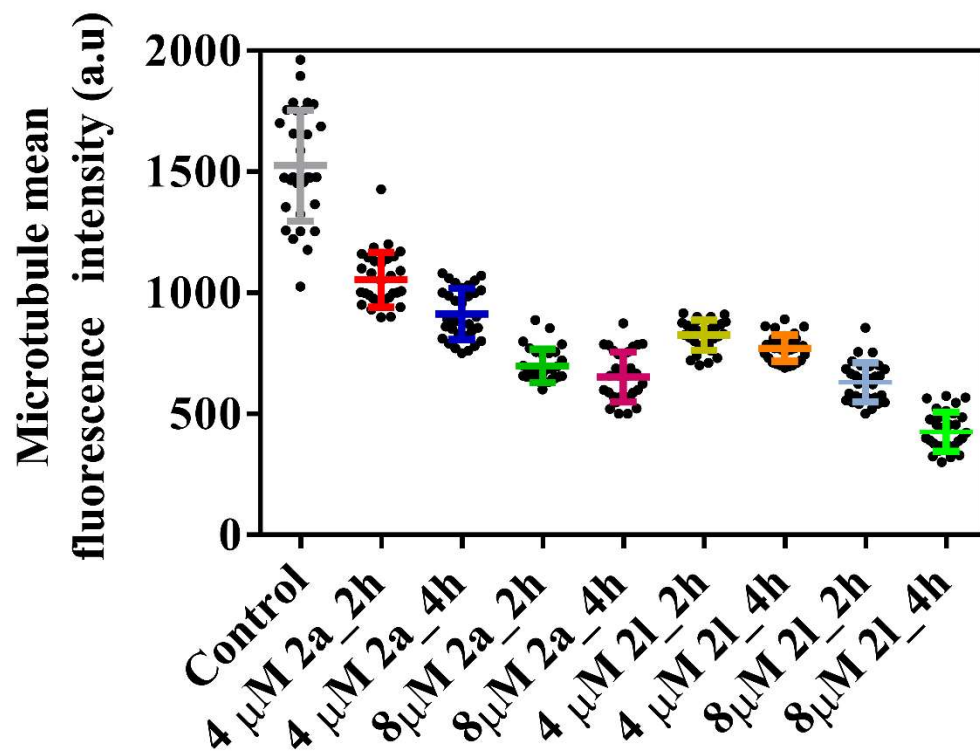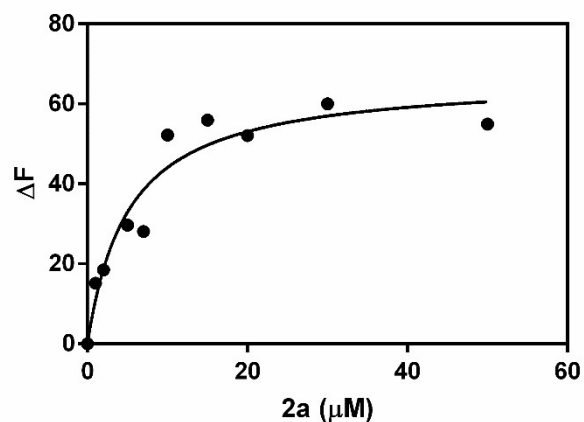
Supplemental Figure 11

Quantification of interphase microtubule intensity of PC3 in the absence and presence of 4 and 12 μM of **2a** and **2l** for 2hours and 4 hours. Experiment was repeated three times and error bar represents standard deviation.

(A)

(b)
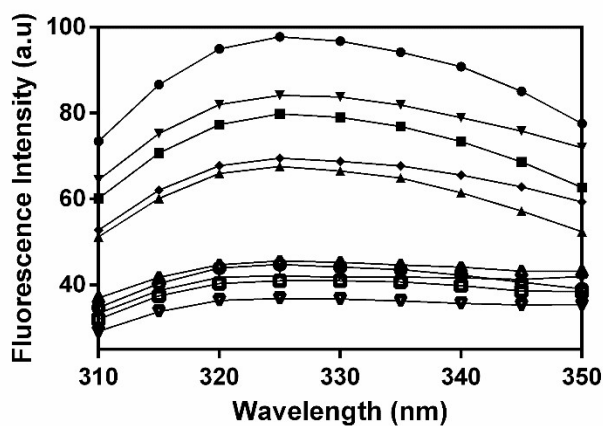
Supplemental Figure 12

Determination of the dissociation constant (K_d) of the tubulin-**2a** complex. **(A)** the fluorescence of tubulin decreases with increasing concentrations of **2a**; 0 (●), 1 (■), 2 (▲), 5 (▼), 7 (♦), 10 (○), 15 (□), 20 (Δ), 30 (★) and 50 (◊) μM; **(B)** the line of best fit for the difference in fluorescence at 340 nm at different concentrations was fitted gives the dissociation constant (K_d). The experiment was repeated three times.
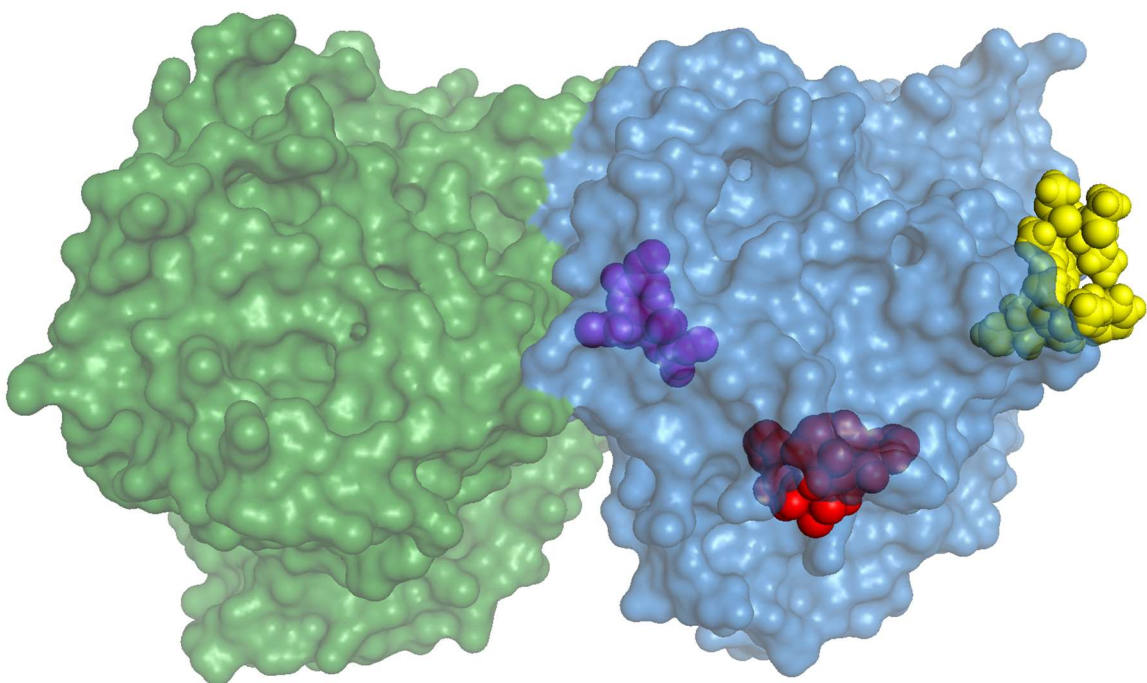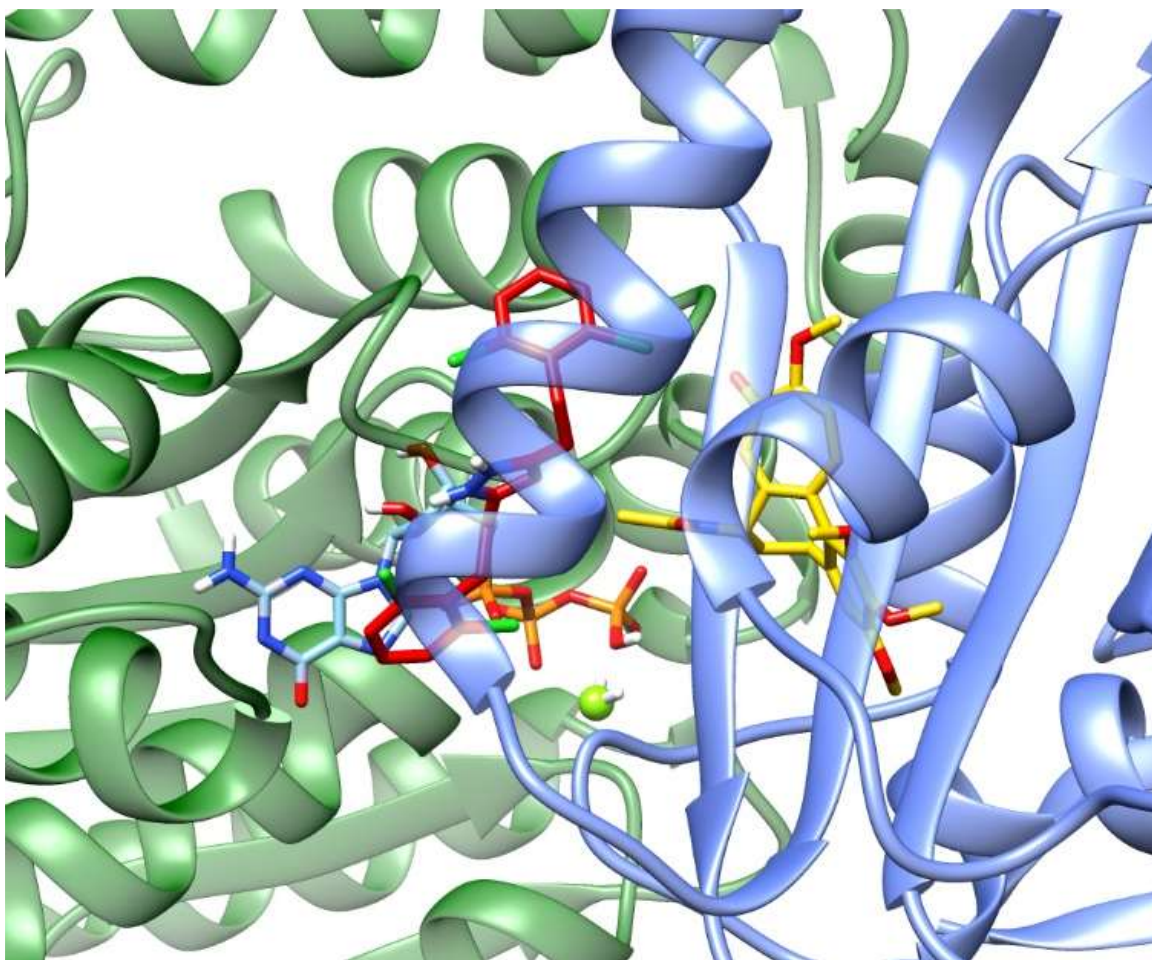
Supplemental Figure 13

Surface representation of α and β tubulin heterodimer with the three major binding sites. Tubulin is taken from the crystal structure of PDB: 5J2T. β-tubulin surface structure is shown in cyan colour while α-tubulin surface structure is shown in green colour. The three main ligands binding on three different binding sites on tubulin are shown by sphere representation. Colchicine is shown as navy blue spheres taken from PDB: 4O2B. Vinblastine is shown as yellow spheres taken from PDB: 5J2T. Taxol is shown as red spheres taken from PDB: 1TUB. The structure was generated using PyMOL.

(a)

(b)

(c)
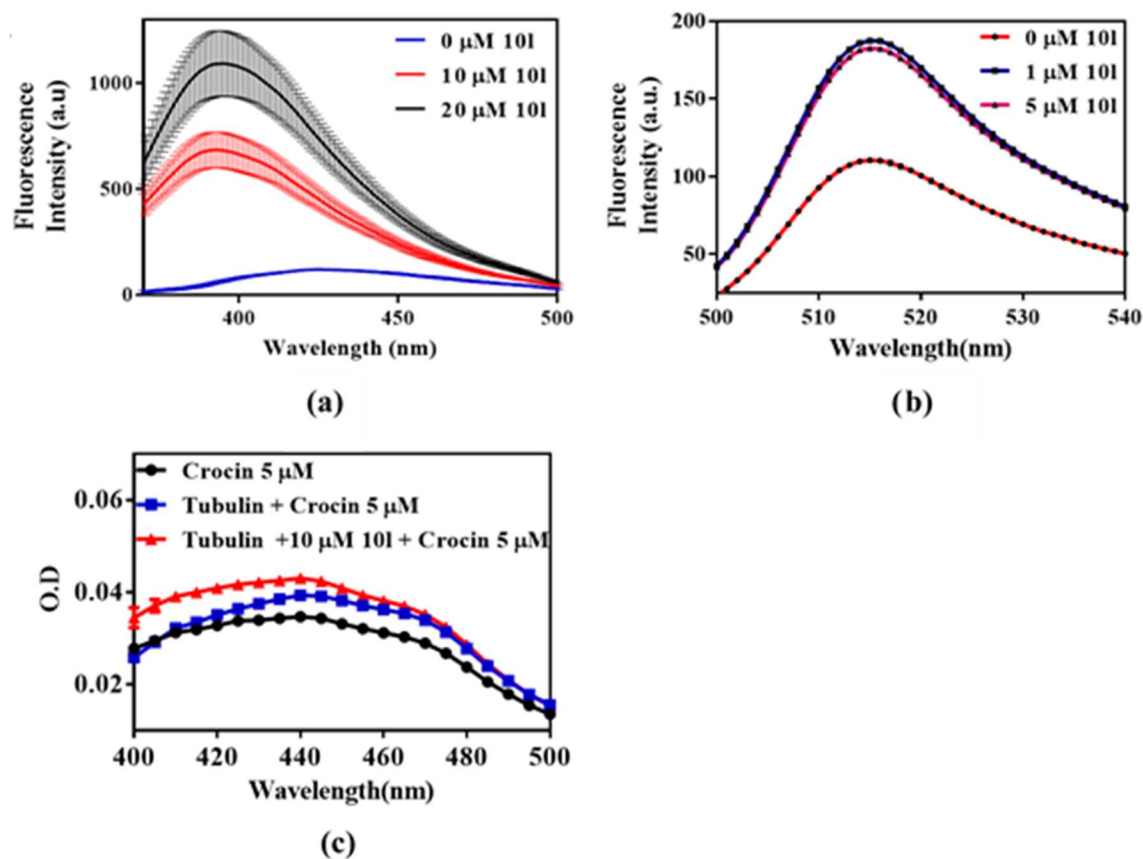
Supplemental Figure 14

Determination of the binding site of **2l** on tubulin; **(A)** the fluorescence of colchicine (blue) increases with increasing concentrations of **2l**; 10 (red) and 20 (black) μM indicating that **2l** does not bind to the colchicine binding site; **(B)** the fluorescence of BODIPY-FL-vinblastine (red) increases with increasing concentrations of **2l**; 1 (blue) and 5 (pink) μM showing **2l** does not bind to the vinblastine binding site ; **(C)** the absorbance of crocin (black) increases upon incubation with tubulin (blue) but remains unchanged (red) in presence of **2l** indicating that **2l** does not bind to the crocin binding site.

Supplemental Figure 15

Docking of **2l** and colchicine on tubulin; **2l** (red sticks) and colchicine (yellow sticks) are shown
to bind at the β-tubulin (blue ribbons) and α-tubulin (green ribbons) heterodimer interface. GTP is
shown in blue stick and green ball is magnesium ion.